ENHANCED DYNAMIC RANGE FRINGE PROJECTION FOR MICRO-STRUCTURE CHARACTERIZATION

by

Ayman Mohammad Samara

A dissertation submitted to the faculty of

The University of North Carolina at Charlotte

in partial fulfillment of the requirements

for the degree of Doctor of Philosophy in

Optical Science and Engineering

Charlotte

2005

Approved by:

_____

Dr. Angela D. Davies

_____

Dr. Faramarz Farahi

_____

Dr. Robert J. Hocken

_____

Dr. Michael A. Fiddy

_____

Dr. Thomas P. Weldon

Dr. Robert K. Tyson

ABSTRACT

AYMAN MOHAMMAD SAMARA. Enhanced dynamic range fringe projection for micro-structure characterization. (Under the direction of DR. ANGELA D. DAVIES)

We present a solution for one of the main limitations in classical interferometry and fringe projection, which is the dynamic range limitation. The technique is based on real time inverse fringe projection to enhance the dynamic range and increase the vertical resolution without the need of prior information about the test object or the system parameters. The object's form optical path difference map is first measured, and then used to generate inverse fringes to optically filter the low spatial frequency form. The surface finish can then be measured without the impact of the form.

A stereo microscope-based fringe projection system was designed, constructed, and used to illustrate the technique. The system was also used to characterize solder bumps with an uncertainty of approximately 10 %.

Individual solder bumps were also characterized using Zygo's NewView^{TM} scanning white light interferometer (SWLI), and the results were compared to measurements on Intel's bump metrology tool. The results show that the SWLI has the lowest uncertainty and maximum repeatability but the lowest measurement speed. Intel's tool has a

repeatability of approximately 1% and a measurement speed of about 10 minutes per 100,000 bumps, making it suitable for high volume process control.

DEDICATION

To my parents and family, the source of endless love and support.

ACKNOWLEDGMENTS

I would like to thank my advisor Dr. Angela Davies who directed this project with vision, elegance and patience. She made this research a pleasant experience for me, and without her extraordinary support I would never have been able to complete this project.

I would also like to thank Dr. Faramarz Farahi who has been a terrific mentor, giving me the key insight, and kindly volunteered to co-advise this project sounding out brilliant ideas and solutions that made this project one of the most challenging and joyful experiences in my life.

I would like to thank my committee members Dr. Robert Hocken and Dr. Michael Fiddy for the time and effort they spent in reviewing this manuscript. They gave the dissertation careful reading and great suggestions that made it a better one.

The faculty and graduate students of the department of Physics and Optical Science and the Center for Optoelectronics and Optical Communications have been a great

resource and helping hand. I enjoyed collaborating with them, their enthusiasm and support made me proud to be part of this wonderful family.

Intel Corporation is the initiator of this project and I would like to thank them for their continuous support and feedback. The experiences and skills I developed during my internships at Intel influenced the direction and outcomes of my research.

Our friends from Veeco Instruments kindly helped us with technical assistance and provided us with a copy of their fringe analysis software Vision^{TM} .

Funding for this project was provided by the Industrial Affiliates of the Center for Precision Metrology at the University of North Carolina at Charlotte.

TABLE OF CONTENTS

CHAPTER 1: INTRODUCTION

1.1 Project history and motivation

Solder bumps are partial-spherical microstructures approximately 100 μm in diameter and 35 μm high. They are grouped together on a substrate to function as high density interconnects for the die in flip chip technology for advanced integrated circuit packaging.

The original project started when Intel experienced unacceptable yield loss during the revenue product ramp of the current substrate technology platform. To avoid this problem in the next generations' substrate platforms, the volume of solder bumps was defined as the critical monitor. It was found that solder bumps with insufficient solder volume will not be able to connect with the die and hence causing an open circuit leading to a faulty processor or chipset. On the other hand, bumps with extra solder volume have the tendency to spread during the packaging process short circuiting the neighboring bumps. So it is critical to measure the volume of these bumps in order to set a tolerance range for the allowed solder volume used in manufacturing different packages.

Research was conducted to find and select the suitable metrology tool. After worldwide technology research, Intel selected an optical metrology instrument based on fringe projection as their tool to characterize solder bumps. The supplier name is not disclosed in this document as requested by Intel.

As a member of the industrial affiliates program through the Center for Precision Metrology at UNC-Charlotte, Intel suggested a project to asses the measurement uncertainty of their tool.

The project was divided into two parts. The first part was to measure individual solder bumps using state-of-the-art techniques, and then carry out an intercomparison with Intel's instrument. The instrument selected for the measurements at UNC-Charlotte is the Zygo New View^{TM} scanning white light interferometer (SWLI),

The second part of the project was to research and select a technique suitable for measuring arrays of bumps and other micro structures, design and construct a system based on that technique, and then use the system to measure solder bumps. After researching the literature, moiré and fringe projection techniques were selected for the reasons mentioned later in this chapter.

Over the course of the project, ideas were investigated to expand the scope, and build a system capable of measuring a wide range of surfaces and microstructures, and investigate a solution for one of the main limitations of classical optical interferometers and fringe projection systems, which is, the dynamic range limitation.

Classical laser interferometers suffer from a limited dynamic range. It can easily be shown that in phase shifting interferometry the height difference between two adjacent data points should be less than $\lambda/4$ for the phase to be resolved without ambiguities, where λ is the wavelength of the light used [1]. A variety of techniques are used to extend

the range beyond this limit. These include scanning white light interferometry, heterodyne interferometry, and multiple wavelength interferometry [1-8].

In this project we offer a technique to enhance the dynamic range in fringe projection systems based on real time, inverse fringe projection. The same concept is applicable to laser interferometry as well. The technique is described in detail, simulated, modeled, and tested in Chapters 3 and 4.

1.2 Document outline

The rest of Chapter 1 investigates different techniques for measuring microstructures. The pros and cons of each are discussed and compared to motivate our technology selection.

As mentioned in Section 1.1, fringe projection and moiré techniques are the bases of the system we built and represent the core of this project. In the first half of Chapter 2 we provide an overview of the moiré effect, its nature and mathematical model, and the different types of moiré setups and their metrology applications. The second half focuses on the details of the fringe projection and projection moiré techniques. A complete mathematical model is derived and used to investigate the origin and solutions of the perspective error, which is very common in moiré and fringe projection systems. Understanding the mathematical model was critical to derive the methodology used later to correct for the system biases and apply our dynamic range enhancement technique.

In Chapter 3, the reader will find an overview of the dynamic range limitations in laser interferometers and fringe projection systems, illustrated with computer simulations. After that, our dynamic range enhancing technique is modeled and simulated using Matlab™.

Chapter 4 is divided into 4 sections. The first section describes the setup of our fringe projection system and the hardware and optical components. The second section explains the Matlab™ software algorithms used to control the system and make measurements, and then it describes the fringe analysis software, Vision™, and the algorithms used for analyses and image processing. In the third section, the mathematical modeling described in Chapter 2 is used to model our system and derive the methodology and the procedures necessary to apply the dynamic range enhancing technique described in Chapter 3. Finally, experimental procedures and results are presented in the last section. The procedures include system preparation and calibration, system bias correction, and then measurement of surface profiles and surface finish.

Solder bump characterization is a main part of this project and is discussed in Chapter 5. First, an overview of the nature and shape of solder bumps is provided and the challenges faced in characterizing them. Then, we describe the procedures, algorithms, models and results used in characterizing solder bumps and deriving the measurement uncertainties using interferometry. The results are then compared with Intel's measurements. Finally, detailed procedures and results for characterizing solder bums using our fringe projection system are presented. The measurement uncertainties are also

estimated following the Guide to the Expression of Uncertainty in Measurement (GUM) [9].

In the final chapter, Chapter 6, we conclude with a summary of the major achievements of this project and suggest ideas for future work in order to upgrade the system and enhance measurement capabilities and reduce uncertainty.

The document also contains appendixes for all the Matlab^{TM} source code used to develop the algorithms for controlling the fringe projection system, and the algorithms for extracting the bump parameters from the SWLI data.

1.3 Optical techniques for surface metrology

1.3.1 Laser triangulation

In laser triangulation, a laser beam with a small spot is projected onto the surface of interest, and the light scattered (or reflected) is imaged onto a CCD array. As the point of light falling on the object moves closer to or farther from the reference point, the spot position on the detector changes as illustrated in Figure 1-1

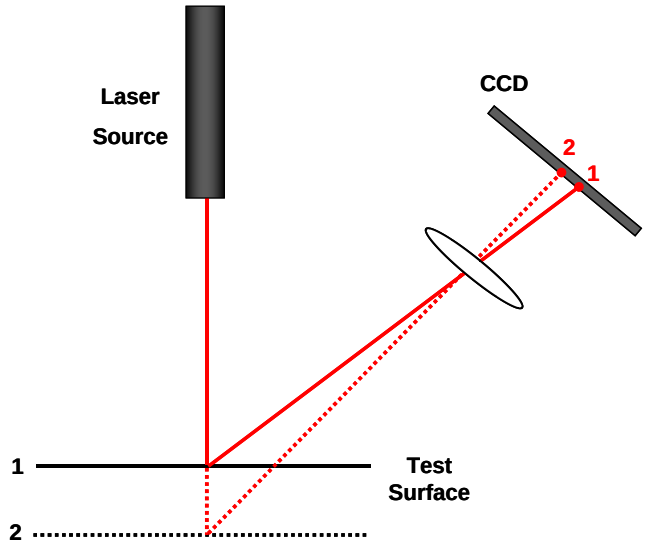

Figure 1-1. Laser triangulation setup

Based on the reflection characteristics of the surface, two types of sensors (optical setups) are needed, either diffuse or reflective. Smooth surfaces typically require a specular sensor (the laser illumination hits the target such that the primary reflected light is reflected into the receiving optics), while surfaces that scatter light are easier to measure with a diffuse sensor. Most surfaces have both specular and diffusive properties and a combination of both sensors can be used [10,11].

The lateral resolution of the system is usually limited by the laser spot size and the camera resolution. The vertical resolution is determined by the previous factors in addition to the angle of projection and viewing optics.

The detectors in most laser triangulation systems are called position-sensing detectors (PSDs) that use multiple average intensity sensors with electrical current

outputs. The amount of current from each sensor is proportional to the spot's position on the detector. If the spot is in the middle of the detector, centered between the sensors, the sensor outputs will be equal; as it moves off center, the sensor outputs change and spot position can be calculated from the relative change [10].

The advantage of such a system is the high speed and simple processing requirement. One disadvantage of the PSDs is they require only one spot on the detector. If more that one spot exists, the detector reports some average current and calculates an incorrect position. The other disadvantage is that they are very sensitive to spot intensity. If the spot intensity changes while moving, the sensor will report an incorrect position.

Some commercial systems are available, for example the SVS 8200-SPI from GSI Lumonics [12]. The system has a Z-resolution of 2 μm and a lateral resolution of approximately 15 μm.

1.3.2 Confocal microscopy

Confocal microscopy was invented to image biological specimens where there is a need to eliminate the out of focus light [13-14]. Figure 1-2 shows a confocal microscope setup. A laser beam passes through a pinhole that is in a conjugate plane (confocal) with a scanning point on the object, and a second pinhole is positioned in front of the detector. As the laser is reflected by a dichromatic mirror and scanned across the specimen in a defined focal plane, secondary fluorescence emitted from

points on the specimen (in the same focal plane) pass back through the dichromatic mirror and are focused as a confocal point at the detector pinhole. [14]

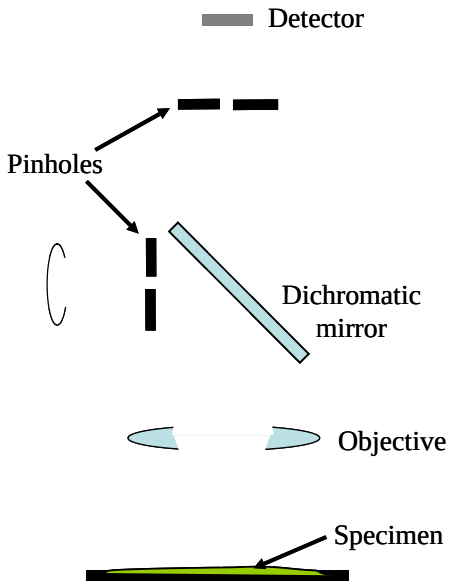

Figure 1-2. Basic confocal microscope setup.

In surface metrology, where high speed measurements are desirable and the surfaces are specular or diffusive, the pinhole in front of the laser source is replaced by a micro-lens array as shown in Figure 1-3. The micro-lenses allow a parallel measurement of a large filed of view. The more lenses in the array, the larger the field of view. The laser beam, after going through the micro-lens array, forms multiple focused beams that hit the test surface and reflect (or scatter) back to go through the same micro-mirror array and then focus through a pinhole onto a detector array. The detector receives the maximum intensity for each beam when the beam is exactly focused on the surface. Therefore, the surface is vertically scanned in small

steps for a measurement. The vertical position corresponding to the maximum intensity at each pixel is recorded to determine the height of the surface for each pixel. The micro-lens array is often scanned and the object remains static for faster operation.

The vertical resolution of the system is determined by the z-scanning step size. The lateral resolution is determined by the laser focus spot size and the distance between the adjacent lenses in the micro-lens array.

Several commercial confocal systems for surface metrology are available from companies like Nikon, ICOS, Olympus and August technologies. The lateral resolution for many is approximately 30 μm, Z-resolution 5 - 0.5 μm, and some are capable of measuring a field of view of approximately 25 mm^2 in less than half a second.

The main limitation of such systems is the lateral resolution, since it's determined by the lens size and separation in the micro-lens array. The surface finish is another limitation. Confocal systems work better for reflective surfaces. The more diffusive the surface is, the higher the laser power needed.

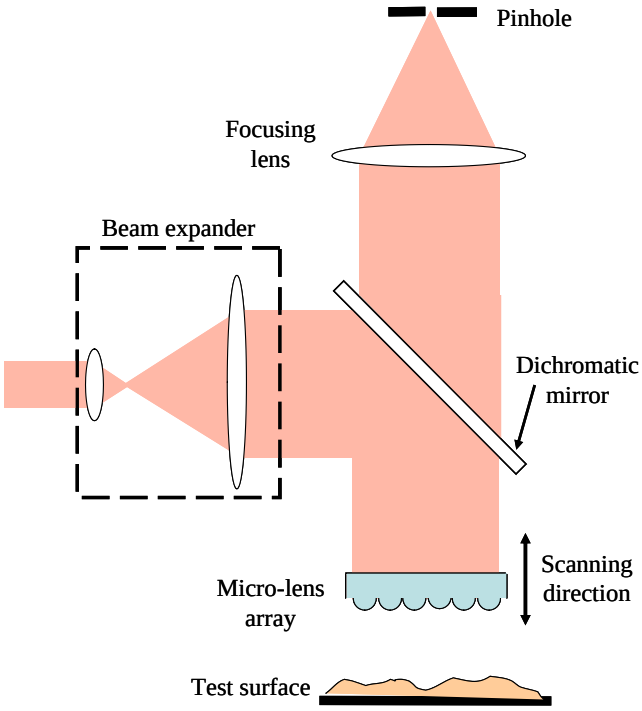

Figure 1-3. Confocal setup for surface metrology. The pinhole is replaced by a micro-lens array to cover a large field of view.

1.3.3 White light interferometry

Most interferometers use lasers as the light source. This is because the long coherence length makes it easy to create interference fringes without the need of matching the interferometer path lengths [1]. Laser interferometric profilometers combined with phase shifting techniques offer excellent vertical resolution in the nanometer to angstrom levels [1-3]. On the other hand laser interferometers suffer a limited dynamic range since the range is defined by the wavelength of light. In particular phase ambiguity limits the measurement range to phase shifts of less than 2π, in other

words the height difference between two adjacent data points on the surface is limited to $\lambda/4$, where λ is the wavelength of the laser used [1, 3]. Another problem with laser interferometers with a long coherence length is that stray reflections easily create unwanted interference fringes which add noise to the measurement.

The very short coherence length of the white light used in white light interferometry overcomes the problem of stray light interference, but it requires the interferometer path lengths to be matched. High contrast fringes are observed when the path lengths are matched and this can be exploited to extended the dynamic range. White light interferometers are based on standard microscope with an interferometric objective replacing the standard objective. Depending on the magnification needed and the measurement conditions, white light profilers use different types of interferometric objectives including the well known Michelson, Mirau, and Linnik interferometers [15,16]. A brief description of each objective and its uses is given in the following subsections.

1.3.3.1 Michelson interferometer

A Michelson interferometric objective contains a microscope objective, a reference surface and a beam splitter placed between the objective and the test surface (see Figure 1-4). This setup requires the objective to have a long working distance, consequently it is used only with low magnification objectives (less than 10x) with low numerical apertures and large field of views.

1.3.3.2 Mirau interferometer

The Mirau interferometric objective has a microscope objective underneath which a plate is located with a small reflecting spot at the middle that acts as a reference plane. A coated second plate is located under the first plate, to act as a beam splitter. The test surface is placed underneath the beam splitter. The first two plates are very thin and close to each other, so they can be used with middle magnification objectives (20x-50x). Figure 1-5 shows the Mirau objective setup

1.3.3.3 Linnik interferometer

Linnik interferometers are used with high magnification objectives for which the working distance is very small. They consist of a reference arm which contains a high magnification microscope objective that focuses on a reference mirror, and a test arm containing a high magnification microscope objective that focuses on the test surface. A beam splitter is placed between the reference and test arms as shown in Figure 1-6.

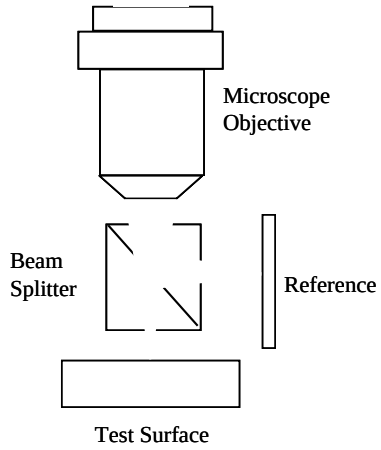

Figure 1-4. Michelson interferometric objective.

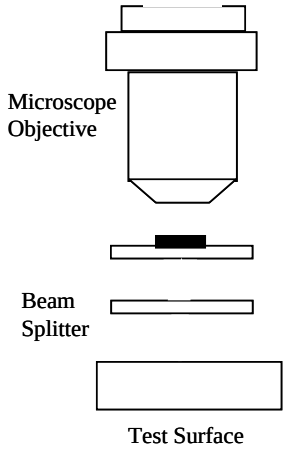

Figure 1-5. Mirau interferometric objective

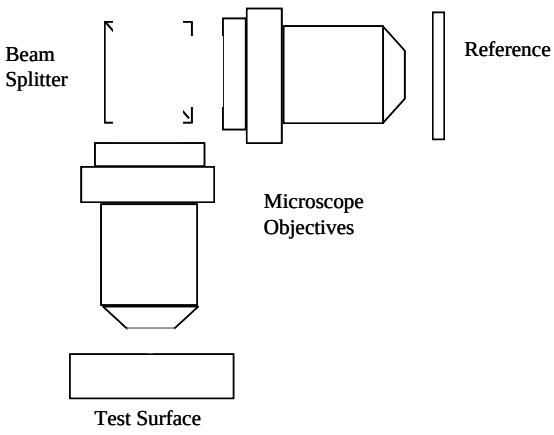

Figure 1-6. Linnik interferometric objective.

The two microscope objectives should be identical and matched with the beam splitter to provide a wavefront with minimum aberrations and maximum interference fringes [15]. The interferometer should be adjusted so that the fringes are obtained when the test surface is at the focal position in order to obtain the highest contrast fringes by focusing on the surface.

There are different types of white light interferometers. One of these types is the scanning white light interferometer (SWLI) which was our chosen technique for measuring individual solder bumps.

In SWLI, broadband (short coherence length) source is used. Due to its short coherence length, high contrast interference fringes are observed only when the path difference is close to zero. Thus, in SWLI, height variations across a test surface are determined by detecting the vertical position at which the interference fringes have maximum contrast. In this type of measurement, there are no height ambiguities and no focus errors since the surface is in focus when the maximum fringe contrast is detected [17-21].

For a low coherence source, the interference fringe intensity as a function of the scanning position forms an envelope like the one obtained in the amplitude modulated communication signals as shown in Figure 1-7. Consequently, a similar analysis is applied to obtain the envelope peak, and hence, the surface height profile. The signal is detected using a CCD array and sampled at constant intervals (every 80 nm for instance) as the optical path difference is varied by vertically moving the sample or the microscope

objective. The DC and low frequency components are removed with a digital high pass filter, then the signal is rectified and the signal peak detected, locating the vertical position corresponding to the peak. Figure 1-8 illustrates the variation of the peak location with surface height.

Interpolation between sample points can be used to increase the vertical resolution beyond the sampling interval. This type of measurement system produces fast, non-contact, true three-dimensional area measurements for both large steps and rough surfaces with nanometer precision [1].

Finally, to obtain a complete topographic map, many frames are detected as the object is scanned vertically, the peak visibility is detected for each pixel, and the z value is evaluated and recorded in the (x,y) position of the topographic map. A disadvantage is that only a single field of view can be measured at a time and measurements of larger areas require a large number of measurements to be stitched together. But the continuous enhancements in the computational speeds and algorithms is reducing this limitation.

Commercial scanning white light interferometers are available from companies like Zygo and Veeco Instruments. For instance, Zygo's New View SWLI in the Center for Precision Metrology has a vertical resolution in the rage of tens of nano-meters. With the 10× objective it can measure a 0.7 mm^2 field of view with a lateral resolution of 2 μm. Speed is one drawback of such a system. It takes approximately one minute to scan a 75 μm vertical range. The ultra-high resolution makes it a powerful precision metrology tool. This tool was used in this project to measure individual solder bumps to determine

how well the geometry of such structures could be measured and to compare measurement results with Intel's.

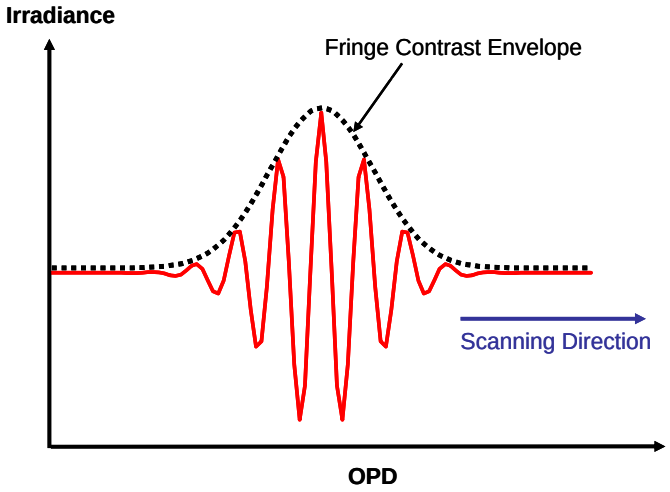

Figure 1-7. Irradiance of a single pixel as the sample is translated trough focus. The envelope is similar to the one obtained in AM communication signals.

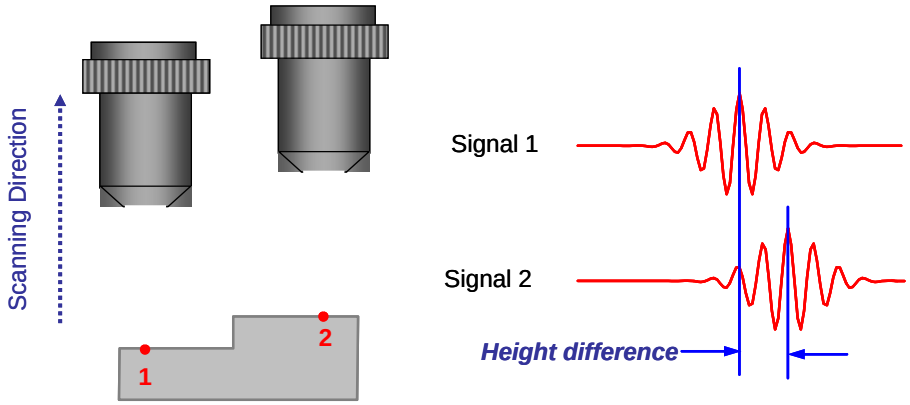

Figure 1-8. Height measurement scheme in SWLI.

1.3.4 Fringe projection and projection moiré

In fringe projection a grating is imaged onto the test surface using projection optics, and then imaged back at a different angle, as shown in Figure 1-9. The projected fringes are distrorted by the surface height profile, and the profile can be obtained by analyzing these fringes using phase shifting techniques [22 - 24]. Phase shifting is achieved by shifting the projected gratings. If another grating is placed in front of the detector, the beating between the two gratings, called moiré fringes, will be detected. Moiré and fringe projection techniques are discussed in detail in Chapter 2.

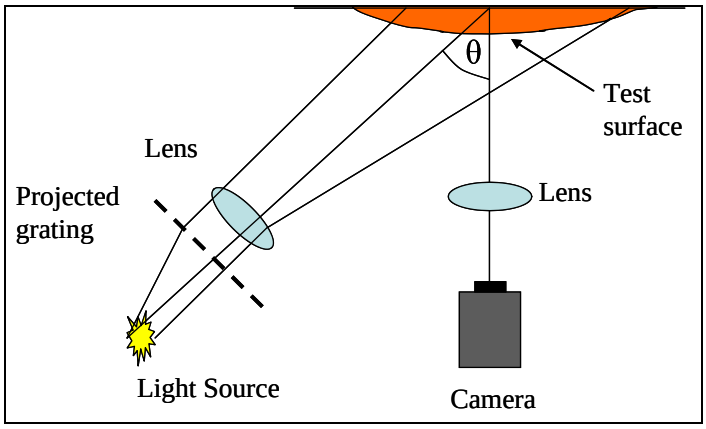

Figure 1-9. Fringe projection setup.

Fringe projection systems have simple hardware setups and they provide full field measurements with high speeds. No moving parts are required if the grating is generated by a spatial light modulator. This is an advantage over the metrology techniques discussed above, where precise lateral or vertical scanning is required.

The vertical and lateral resolution in fringe projection systems are determined by the resolution of the optics and the camera. The vertical resolution is also determined by the frequency of the gratings. Using a spatial light modulator to generate the gratings allows variable grating frequency and hence variable system resolutions applicable for wide range of surfaces and objects. A typical vertical resolution for fringe projection systems reported in the literature is approximately 1 μm [25, 26].

Most of fringe projection systems use white light. This is an advantage over metrology systems that use lasers, which need extra safety precautions and are impacted by undesired stray light interference.

Moiré and fringe projection systems utilize the same fringe analyses techniques used in classical interferometry, which include well-known phase shifting techniques. These techniques are very mature and do not require very uniform illumination over the field of view [22,23]. An enormous number of phase shifting and phase unwrapping algorithms are available and reported in the literature [27-29], and many are implemented in commercial software packages like IntelliWave™, Durango™ and Fringe Applications™.

Many commercial fringe projection systems are available from companies like Solvision and PTT Vision. Some provide a vertical resolution of 2 μm and a lateral resolution of 3 μm, and can measure an approximate 4 mm^2 field of view in about 1 second.

Given these advantages, we decided to design and construct a fringe projection system that could be used to measure wide variety of surfaces including arrays of solder bumps, and introduce modifications to allow dynamic range enhancement based on real time filtering of some surface structures. The system is discussed in detail in Chapter 4.

CHAPTER 2: MOIRÉ AND FRINGE PROJECTION TECHNIQUES

1.4 Introduction

Moiré is a French word for a watered, clouded, or frosted appearance produced upon either textile fabrics or metallic surfaces [30]. In optics it refers to the beating effect between two periodic structures having approximately equal frequencies. In 1874, Lord Rayleigh was the first to use the moiré technique for low sensitivity testing when he looked at the moiré between two identical gratings to determine their quality [31].

Fringe projection is simply projecting (or imaging) a fringe pattern onto a surface and viewing from a different angle. Moiré and fringe projection techniques are closely related. They have been commonly used in metrology and are widely reviewed in the literature [31-46].

This chapter describes moiré theory and the relationship to interferometry, different types of moiré setups, advantages and limitations of the technique and some important moiré applications in metrology. This introduction is necessary for understanding our project.

1.5 Theory of the moiré effect

The similarity between the shape of moiré fringes and the fringes generated by classical interferometry, and hence the similarity of the techniques used to analyze both

fringes, make the term “moiré interferometry” commonly used for different types of moiré. But, the basic moiré effect is not an interference effect in the classical meaning of the word. The term “moiré” is sufficient to describe different types of moiré effects, and the term “moiré interferometry” should be used to describe methods that combine classical interferometry with the moiré effect [31, 35, 47, 48].

Moiré and classical interference are caused by two physically different phenomena. In classical interferometry, the intensity pattern of the interference fringes of two coherent light beams is generated by the coherent addition of the complex amplitudes of the interfering beams [49, 50] . On the other hand, moiré fringes are simply produced by overlapping two periodic structures such as gratings. The light propagates only through points where two spaces from the two gratings overlap and stops where lines from one or both gratings exist. In other words, moiré patterns are obtained by multiplying the intensity transmission distribution of the two patterns. Figure 2-1 shows the moiré pattern generated by overlapping two equal frequency gratings with one slightly rotated with respect to the other.

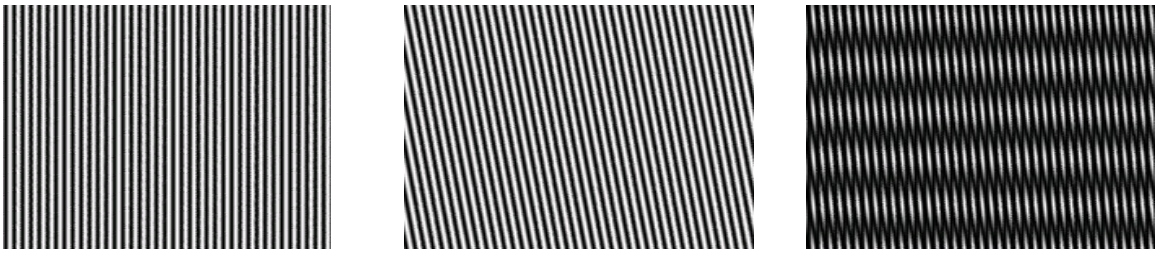

(a) **(b)** **(c)**

Figure 2-1. (a) Straight line sinusoidal grating. (b) Second grating with same frequency as the first one and slightly rotated. (c) The thick horizontal black lines represent moiré between the two gratings generated by multiplying the intensity distribution of both gratings.

Since generating moiré patterns requires periodic or quasi-periodic structures, a Fourier series approach becomes very useful for modeling the moiré effect [31-34].

The transmittance function for any two arbitrary periodic gratings can be expressed in a Fourier series as $T_1(x, y)$ and $T_2(x, y)$:

$$T_1(x, y) = a_1 + \sum_{n=1}^{\infty} b_{1n} \cos[n\phi_1(x, y)],$$
$$T_2(x, y) = a_2 + \sum_{m=1}^{\infty} b_{2m} \cos[m\phi_2(x, y)], \qquad \textbf{(2-1)}$$

where $\phi_1(x, y)$ and $\phi_2(x, y)$ represent the basic line shape functions of gratings 1 and 2, respectively. The a coefficients are the zero frequency components of the Fourier series, and the b coefficients describe the overall profile of the grating lines (sinusoidal, square, etc). For example, consider the straight-line sinusoidal-profile grating shown in Figure 2-2. For this particular grating, $\phi(x, y) = \frac{2\pi x}{p}$, where p is the grating period. Because of the sinusoidal profile, the only surviving b term is b_1. Assuming that the transmittance amplitude has a maximum of one and a minimum of zero, solving for the Fourier series coefficients gives $a = b_1 = \frac{1}{2}$. Hence, the transmittance function for this grating is

$$T(x, y) = \frac{1}{2} + \frac{1}{2}\cos[\frac{2\pi x}{p}] \ . \qquad (2\text{-}2)$$

Consider again Equation 2-1. Multiplying the transmittance functions for both gratings gives

$$T_1(x,y).T_2(x,y) = a_1a_2 + a_1\sum_{m=1}^{\infty} b_{2m}\cos[m\phi_2(x,y)] + a_2\sum_{n=1}^{\infty} b_{1n}\cos[n\phi_1(x,y)] + \sum_{m=1}^{\infty}\sum_{n=1}^{\infty} b_{2m}b_{1n}\cos[m\phi_2(x,y)]\cos[n\phi_1(x,y)]. \quad \textbf{(2-3)}$$

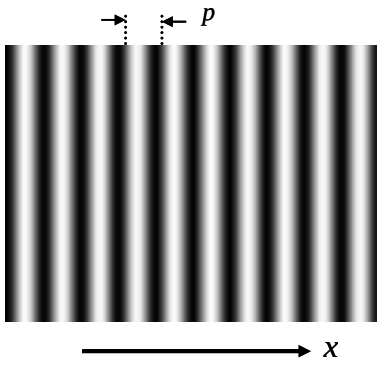

Figure 2-2. Straight sinusoidal grating

The first term of Equation 2-3 is the zero frequency component of the new transmittance function. The second and third terms represent two sets of patterns with the same frequency as the two original gratings, and the fourth term contains information about the new generated pattern. Using trigonometric identities, term four can be written as

$$\frac{1}{2}b_{11}b_{21}\cos[\phi_1(x,y)-\phi_2(x,y)] + \frac{1}{2}\sum_{m=1}^{\infty}\sum_{n=1}^{\infty} b_{2m}b_{1n}\cos[n\phi_1(x,y)-m\phi_2(x,y)], \text{ n and m both} \neq 1 + \frac{1}{2}\sum_{m=1}^{\infty}\sum_{n=1}^{\infty} b_{2m}b_{1n}\cos[m\phi_2(x,y)+n\phi_1(x,y)].$$

(2-4)

The first term is the difference between the fundamental components of the two gratings and represents the fundamental component of the moiré pattern. The other two terms are higher frequency components that exist only for non-sinusoidal grating profiles.

Equation 2-4 can be used to predict moiré patterns. Consider two vertical sinusoidal gratings with frequencies f_1 and f_2, respectively. The two gratings are oriented with an angle 2θ between them as shown in the figure. In this case, the two grating functions are

$$\phi_1(x,y) = 2\pi f_1(x\cos\theta + y\sin\theta), \text{ and}$$
$$\phi_2(x,y) = 2\pi f_2(x\cos\theta - y\sin\theta). \tag{2-5}$$

From Equation 2-4, the moiré intensity pattern can be written as

$$I = A + B\cos(\phi_1 - \phi_2)$$
$$= A + B\cos(2\pi f_{beat} x\cos\theta + 4\pi f_{average} y\sin\theta), \tag{2-6}$$
$$\text{where: } f_{beat} = f_1 - f_2$$
$$f_{average} = \frac{f_1 + f_2}{2}.$$

The moiré bright lines should satisfy the following equation:

$$\phi_1(x,y) - \phi_2(x,y) = N2\pi. \tag{2-7}$$

where *N* is an integer represents the fringe order. Three different cases can be recognized:

Case 1: $f_1 = f_2 = f$, and $\theta \neq 0$, the moiré fringe centers satisfy:

$$\frac{N}{f} = 2y\sin\theta \Rightarrow y = \frac{N}{2f\sin\theta} \tag{2-8}$$

The equation represents horizontal lines with frequency $f_{moire} = 2f\sin\theta$, as shown in Figure 2-3

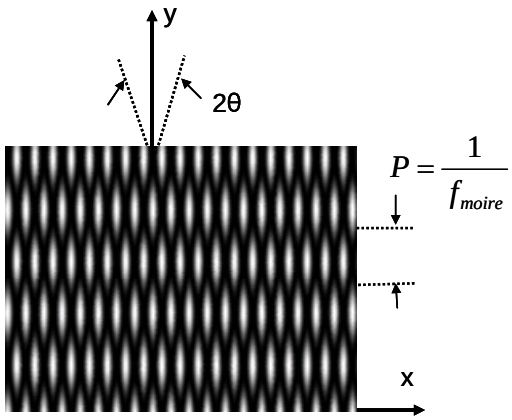

Figure 2-3. Moiré fringes for case 1

Case 2: The two gratings are parallel with slightly different frequencies, $f_1 \neq f_2$ and $\theta = 0$.

In this case moiré fringes can be represented by the following equation:

$$x = \frac{N}{f_{beat}}. \tag{2-9}$$

Moiré fringes are parallel vertical lines with frequency f_{beat} as shown in Figure 2-4.

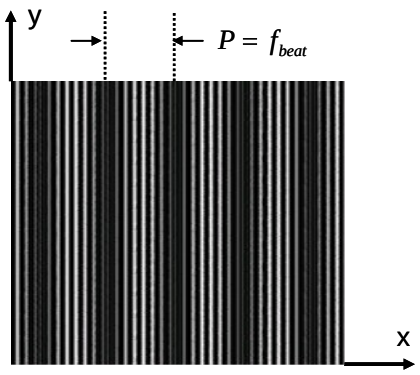

Figure 2-4. Moiré fringes for case 2

Case 3: The general case $f_1 \neq f_2$, and $\theta \neq 0$. The moiré fringe equation will be

$$\frac{N}{f_{average}} = \frac{f_{beat}}{f_{average}} x\cos\theta + 2y\sin\theta. \tag{2-10}$$

The moiré fringes are parallel straight lines with frequency and orientation dependent on the gratings frequency difference and the angle between them. This case is illustrated in Figure 2-5.

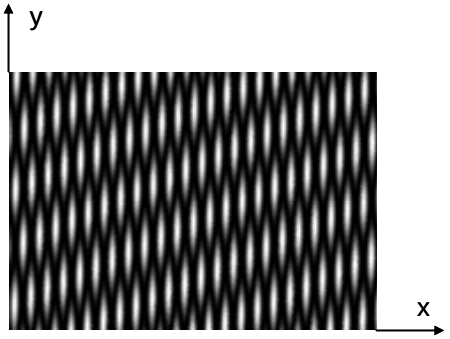

Figure 2-5. Moiré fringes for case 3.

1.6 Moiré in metrology

In the previous two sections the moiré phenomenon was introduced, and the modulation of the light intensities between two periodic patterns was described. This modulation conveys information about the two patterns and the relative changes between them. The moiré effect simply works as a magnifier for these changes. If one of the gratings is moved slightly or deformed, moiré fringes will show a much exaggerated movement or deformation, which makes moiré a very powerful metrology tool.

Depending on the application and the type of the grating, different moiré methods can be used. If the grating was imprinted or engraved on the surface, in-plane (lateral) displacement and rotations can be measured. And this is called intrinsic moiré [42].

Another method is reflection moiré. In this case the image of the gratings is reflected of the test surface and this provides information concerning the slopes of the surface.

Two methods are used for out of plane displacements and 3D contouring, the shadow moiré, where the shadow of a grating is projected on the surface and viewed from an angle through the same grating, and the projection moiré, where the grating is imaged on the test surface and viewed from an angle through another grating called the mask grating. Each method is discussed in the next few subsections. More attention is given for fringe projection and projected moiré, since they are the core of this project.

1.6.1 Intrinsic moiré for in-plane displacement measurements

With this type, a grid (two sets of equally-spaced parallel lines perpendicular to each other) is engraved or imprinted on the test surface. To simplify the math consider only the grid lines that are parallel to the y axis. The intensity distribution of the lines can be represented by

$$I_1 = a + b\cos[2\pi f_x x]\ , \tag{2-11}$$

where f_x is the spatial frequency of the grid in the x-direction. If the surface is moved or deformed in the x-direction, f_x is modified. The argument of the cosine function in Equation 2-11, call it θ, can then be expressed as [42]

$$\theta(x) = 2\pi(f_x x + \psi(x)), \tag{2-12}$$

where $\psi(x)$ is the modulation function. The modulation function is equal to the x-displacement of the grid from its original position, $u(x)$, multiplied by the grid frequency and contains all the information about the deformations in the x-direction, hence

$$\psi(x) = f_x u(x) \Rightarrow u(x) = \frac{\psi(x)}{f_x}. \tag{2-13}$$

For small displacements and rotations, a linearized strain tensor is defined by [42]

$$\varepsilon_x = \frac{\partial u(x)}{\partial x}\ . \tag{2-14}$$

Considering the grid lines parallel to the x-axis, the same derivation is done for the displacement vector in the y-direction, v.

In order to fully describe the relative displacements of the test surface, two modulating functions are needed, $\psi_x(x,y)$ and $\psi_y(x,y)$. Together, both functions include all the information about the displacements:

$$\varepsilon_x = \frac{\partial u}{\partial x} = \frac{1}{f}\frac{\partial \psi_x(x,y)}{\partial x},\ \varepsilon_y = \frac{\partial v}{\partial y} = \frac{1}{f}\frac{\partial \psi_y(x,y)}{\partial y}$$
$$\frac{\partial u}{\partial y} = \frac{1}{f}\frac{\partial \psi_x(x,y)}{\partial y},$$
$$\frac{\partial v}{\partial x} = \frac{1}{f}\frac{\partial \psi_y(x,y)}{\partial x},$$
$$\varepsilon_{xy} = \frac{1}{2}\left[\frac{\partial u}{\partial y} + \frac{\partial v}{\partial x}\right]. \qquad (2\text{-}15)$$

The two modulating functions are encoded in the phase of the grid lines and can be recovered using the common fringe analysis techniques.

Intrinsic moiré is widely used in stress and strain analysis and thermal expansion measurements for a variety of applications. Refer to references 51-59 for more details.

1.6.2 Reflection moiré

In reflection moiré, the test object must have a specular reflecting surface. The moiré pattern results from superimposing the image of the grating reflected from the surface in its original position and the image of the grating reflected of the deformed surface. Figure 2-6 shows an equivalent ray diagram of a simple reflection moiré setup. The test surface produces a virtual image of the grating at distance d behind the surface. When the surface is in its initial (non-deformed) position, a point P in the camera plane will have its

conjugate at point P_1 as shown in the figure. When the surface gets deformed, the conjugate of P moves to point P_2.

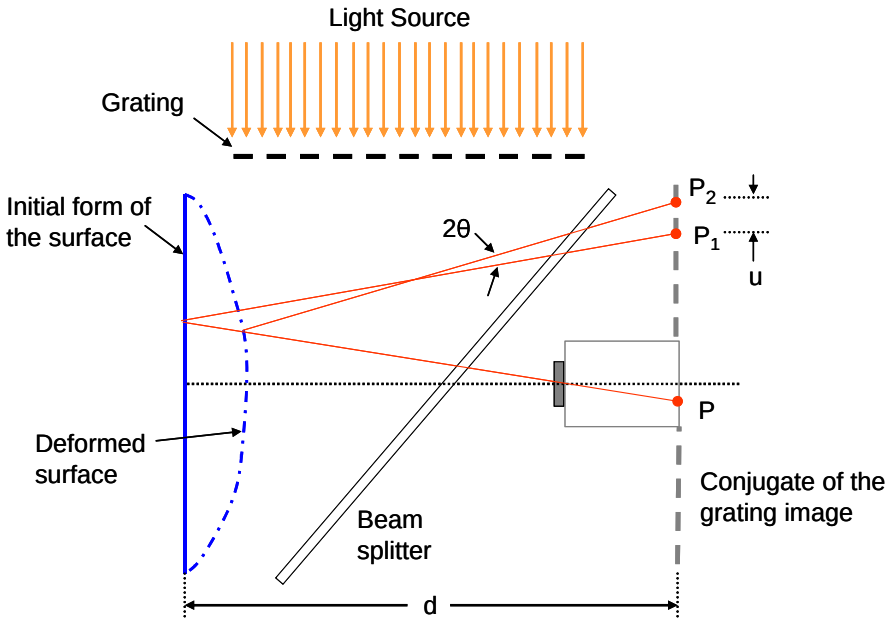

Figure 2-6. Equivalent ray diagram of reflection moiré setup.

Neglecting the second order terms caused by the curvature, the displacement between points P_1 and P_2 is given by [60]

$$u = 2d\theta = p, \text{ which yields to } \theta = \frac{Np}{2d}, \tag{2-16}$$

where p is the period of the grating and N is the moiré fringe order. This means that a moiré fringe is formed where the deformation u is an integer multiple of the grating period.

Reflection moiré was first proposed by Ligtenberg in 1954 [60], and modified by Reider in 1965 [61]. Since then different setups and enhancements on reflection moiré were proposed for different applications [34, 42, 61-66].

1.6.3 Shadow moiré

Both shadow and projection moiré are powerful tools for measuring the object form in three dimensions, which can be referred to as moiré topography. The profile of the object is presented in 2-D contour maps. Unlike reflection moiré, shadow and projection moiré work better for objects that reflect light diffusely.

In shadow moiré, moiré fringes are formed between a grating and its own shadow. A master grating is placed just in front of the object and illuminated with an angle of incidence θ_1, and viewed thorough the same grating with an angle θ_2 as shown in Figure 2-7. Simple ray tracing shows point A is projected on the surface then to point B. Assuming collimated illumination and viewing at infinity or through a telemetric lens system, the equivalent displacement of the grating relative to its shadow is equal to [31, 46, 67-69]

$$\overline{AB} = \overline{AO} + \overline{OB} = Z(\tan\theta_1 + \tan\theta_2), \tag{2-17}$$

and the height Z between the grating and the object point is given by

$$Z = \frac{Np}{\tan\theta_1 + \tan\theta_2}, \tag{2-18}$$

where p is the period of the grating, and N is the number of grating lines between A and B. Equation 2-18 describes a moiré contour map with a constant contour interval, and a reference plane that is parallel to the grating plane.

In case of finite illumination and viewing distances, θ_1 and θ_2 will vary across the test surface resulting in a moiré contour map with varying contour intervals, and the reference surface will no longer be parallel to the grating, as shown in Figure 2-8. However, if the light source and the viewing point are located at the same z-distance, h, above the grating, and if the surface height variations are negligible compared to h, the sum $\tan\theta_1 + \tan\theta_2$ stays constant although θ_1 and θ_2 vary from point to point across the surface. This results in a constant contour interval and a reference parallel to the grating. Figure 2-9 illustrates this situation.

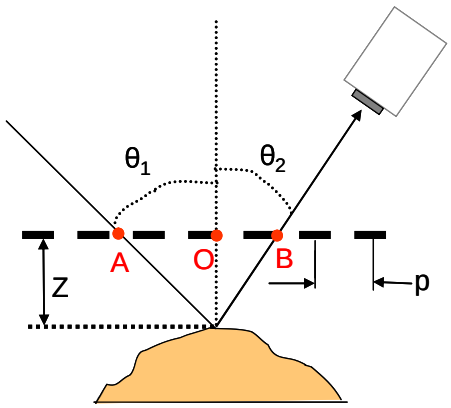

Figure 2-7. Shadow moiré

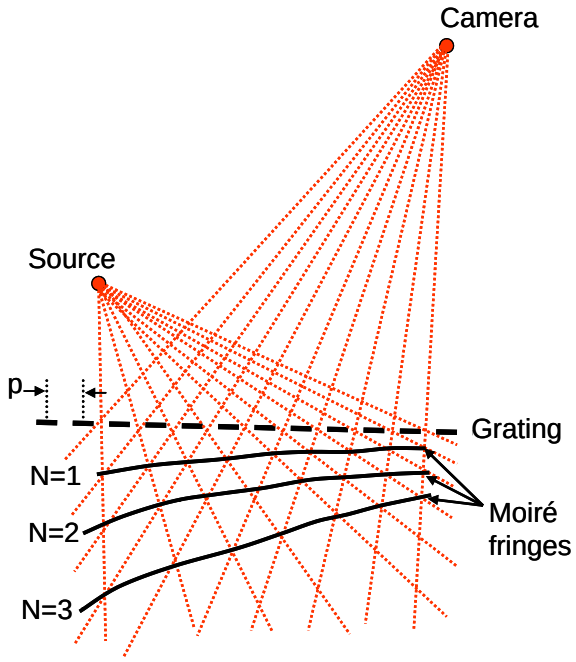

Figure 2-8. Shadow moiré with unequal finite illumination and viewing distances. Moiré contours depend on the point coordinate.

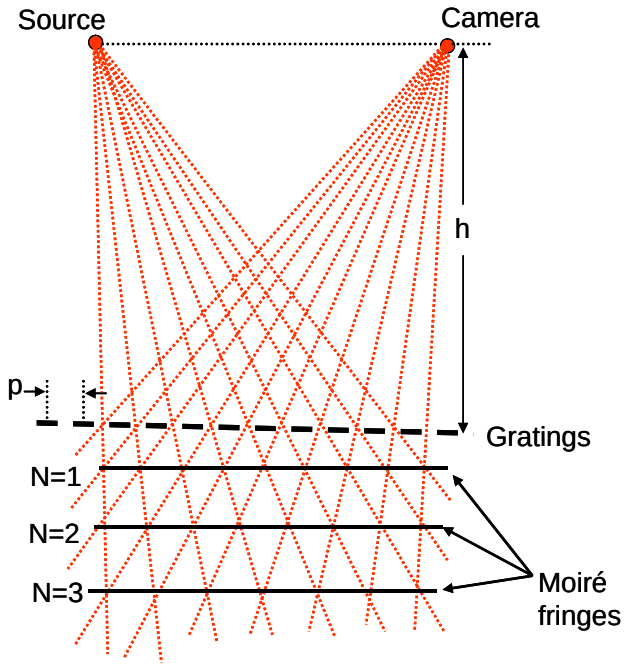

Figure 2-9. Shadow moiré with equal finite illumination and viewing distances. Moiré contours intervals are independent on the point coordinates

In order for shadow moiré to be an efficient method, the test surface has to be quasi-flat so the grating can be placed very close to the object in order for the shadow of the grating to be will defined. This limits the area of the object that can be covered by the grating. Projection moiré is used to overcome this limitation.

For more information on shadow moiré and its applications in industry and medicine, refer to references 70-77.

1.6.4 Fringe projection and projection moiré

In fringe projection the grating is imaged onto the test surface using projection optics, and then imaged back again from a different angle onto a detector array. The fringes can

also be created by means of interference between two plane waves inclined at a small angle to each other [31, 34, 46].

Figure 2-10 shows a typical fringe projection setup. A sinusoidal grating of a constant period p is projected onto a test surface through lens L_1 of which the principle axis makes an angle of θ_1 with the normal on the surface. The surface and the projected fringes are then imaged back onto a detector array through lens L_2 of which the principal axis makes an angle θ_2 with the normal on the surface. Three coordinate systems are used, the grating coordinate system (x_1, y_1, z_1), the surface coordinate system (x_2, y_2, z_2), and the detector array coordinate system (x_3, y_3, z_3). Points 0, 2, and 4 are the origins of the grating, surface and detector coordinate systems, respectively.

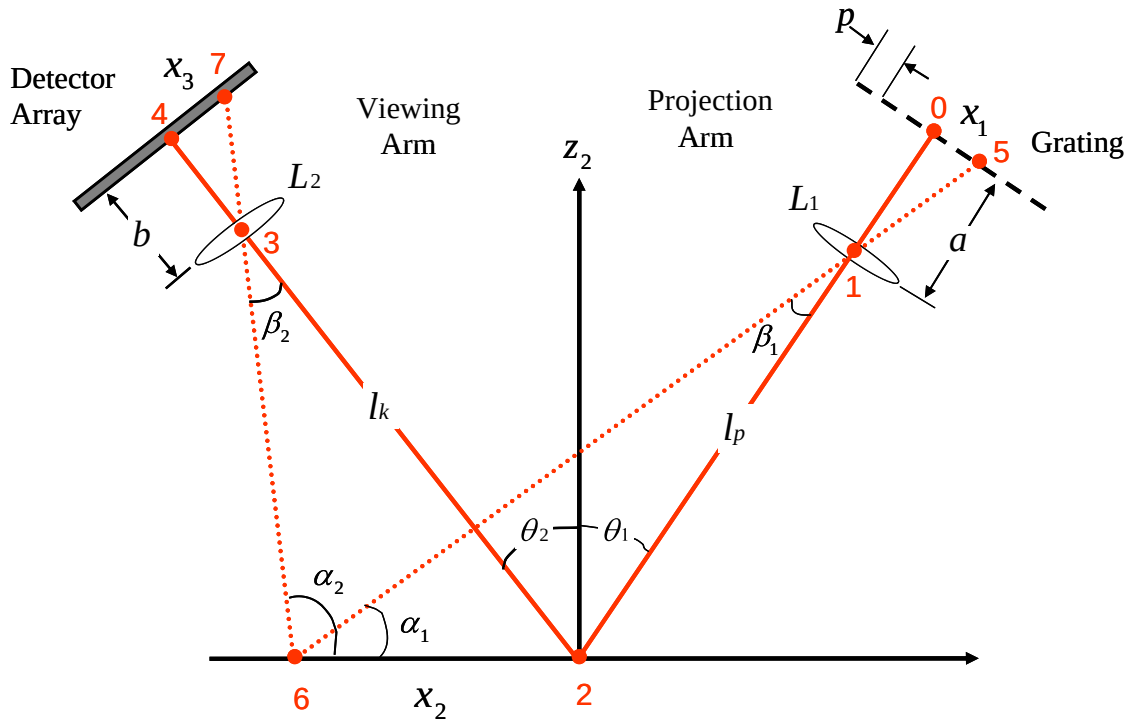

Figure 2-10. Fringe projection setup

To begin the analysis, consider projecting onto a flat surface to find the impact of the system geometry on the period of the fringes as seen by the detector array.

First, focus on the projection arm of the system to find the fringe period on the x_2y_2-plane, λ_{x2}, as a function of x_1. As Figure 2-10 shows, a light ray through the center of lens L_1 goes from point 5 on the grating to point 6 on the x_2y_2-plane. Point 5 lies a distance x_1 from the optical axis of the projection lens and point 6 is a distance x_2 from the origin of the x_2y_2-plane. From triangle *1-2-6* we see that

$$\frac{x_2}{\sin\beta_1} = \frac{l_p}{\sin\alpha_1}, \tag{2-19}$$

and

$$\alpha_1 = 90^\circ - (\beta_1 + \theta_1). \tag{2-20}$$

Using Equation 2-20, Equation 2-19 can be written as

$$\frac{x_2}{\sin\beta_1} = \frac{l_p}{\cos(\theta_1 + \beta_1)} = \frac{l_p}{\cos\theta_1\cos\beta_1 - \sin\theta_1\sin\beta_1}$$

$$\Rightarrow \frac{x_2}{\tan\beta_1} = \frac{l_p}{\cos\theta_1 - \tan\beta_1\sin\theta_1}, \tag{2-21}$$

where l_p is the distance from the center of L_1 to the origin of the x_2y_2-plane. From triangle *0-1-5*, $\tan\beta_1$ is given by

$$\tan\beta_1 = \frac{x_1}{a}, \tag{2-22}$$

where a is the distance from the grating to the lens L_1 along its principal axis.

Substituting (2-22) into (2-21) gives the position x_2 as a function of the position x_1:

$$x_2 = x_2(x_1) = \frac{x_1 l_p}{a\cos\theta_1 - x_1\sin\theta_1}. \tag{2-23}$$

To find the fringe period along the x_2-axis, λ_{x2}, increase x_1 by the grating period p:

$$\lambda_{x2} = x_2(x_1 + p) - x_2(x_1) = \frac{p l_p a\cos\theta_1}{(a\cos\theta_1 - x_1\sin\theta_1)^2 - p\sin\theta_1(a\cos\theta_1 - x_1\sin\theta_1)}. \tag{2-24}$$

Equation 2-24 represents the wavelength of the fringes projected onto a reference surface on the x_2y_2-plane as a function of x_1 and the grating period p. The second term of

the denominator in Equation 2-24 can be neglected, which is a good approximation since p is much smaller than a [46]. So λ_{x2} can be written as

$$\lambda_{x2} = \frac{p l_p a \cos\theta_1}{(a\cos\theta_1 - x_1 \sin\theta_1)^2}. \tag{2-25}$$

Now, focusing on the viewing arm, we will find the fringe period on the detector array plane (λ_{x3}). From triangle *2-3-6* in Figure 2-10 we see that

$$\frac{x_2}{\sin\beta_2} = \frac{l_k}{\sin(\alpha_2)} = \frac{l_k}{\cos(\beta_2 - \theta_1)} = \frac{l_k}{\cos\theta_2\cos\beta_2 + \sin\theta_2\sin\beta_2}$$

$$\Rightarrow \frac{x_2}{\tan\beta_2} = \frac{l_k}{\cos\theta_2 + \tan\beta_2\sin\theta_2}, \tag{2-26}$$

where l_k is the distance from lens L_2 to the origin of the x_2y_2-plane. From triangle *3-4-7* we see that

$$\tan\beta_2 = \frac{x_3}{b}, \tag{2-27}$$

where b is the distance from the detector array to the lens L_2 along its principal axis. Substituting (2-27) into (2-26), the position x_2 as a function of x_3 is given by

$$x_2 = x_2(x_3) = \frac{x_3 l_k}{b\cos\theta_2 + x_3\sin\theta_2}. \tag{2-28}$$

Rearranging the terms in Equation 2-28, the position x_3 as a function of x_2 is given by

$$x_3 = \frac{x_2 b\cos\theta_2}{l_k - x_2\sin\theta_2}. \tag{2-29}$$

To find the fringe period along the x_3-axis (λ_{x3}), increase x_2 by the fringe period along the x_2-axis (λ_{x2}):

$$\lambda_{x3} = x_3(x_2 + \lambda_{x2}) - x_3(x_2) = \frac{\lambda_{x2} l_k a \cos\theta_2}{(l_k - x_2 \sin\theta_2)^2 - \lambda_{x2} \sin\theta_2 (l_k - x_2 \sin\theta_2)}, \quad (2\text{-}30)$$

and since λ_{x2} will be much smaller than l_k, the second term of the denominator in Equation 2-30 can be neglected to give

$$\lambda_{x3} = \frac{\lambda_{x2} l_k a \cos\theta_2}{(l_k - x_2 \sin\theta_2)^2}. \quad (2\text{-}31)$$

Equation 2-31 represents the fringe period as seen by the detector array as a function of the position x_2, and the fringe period along the x_2-axis, λ_{x2}. Substituting λ_{x2} by its value from Equation 2-25, λ_{x3} is becomes

$$\lambda_{x3} = \frac{p(a l_p \cos\theta_1)(l_k a \cos\theta_2)}{(a\cos\theta_1 - x_1 \sin\theta_1)^2 (l_k - x_2 \sin\theta_2)^2}. \quad (2\text{-}32)$$

Substituting x_2 by its value from Equation 2-23, we see that λ_{x3} can be written as

$$\lambda_{x3} = \frac{p(a l_p \cos\theta_1)(l_k a \cos\theta_2)}{(l_k a\cos\theta_1 - l_k x_1 \sin\theta_1 - x_1 l_p \sin\theta_2)^2}. \quad (2\text{-}33)$$

For a symmetric system, which will be the case in our fringe projection system, $a = b$, $l_p = l_k = l$, and $\theta_1 = \theta_2 = \theta$. λ_{x3} becomes

$$\lambda_{x3} = \frac{p(al\cos\theta)^2}{(la\cos\theta - 2lx_1 \sin\theta)^2} = \frac{p}{\left(1 - \frac{2x_1 \tan\theta}{a}\right)^2}. \quad (2\text{-}34)$$

Equation 2-34 represents the fringe period as detected by the camera as a function of the original position on the grating x_1, the grating period p, and the system geometry in a symmetric fringe projection system.

It is important to notice that the period of the projected fringes as seen by the camera is not constant anymore; it's a function of the location x_1. This will cause the reference surface to appear as a non-planar surface. This is called the perspective effect [31], which is discussed in the next section.

Now, consider an object with a height profile given by h as shown in Figure 2-11. From the figure, it is clear that the existence of an object with height h at a point x_2 causes the point location on the reference plane (x_2y_2-plane) to shift from point 6 to point 8. The corresponding shift on the camera plane (from point 7 to 9) is given by the displacement u_3. The coordinates of points 6 and 8 along the x_2 axis are given by $(x_2 - h\tan\gamma_1)$ and $(x_2 + h\tan\gamma_2)$, respectively. Substituting these values into Equation 2-29 for a symmetric system, the coordinates of points 7 and 9 along the x_3 axis are given by

$\frac{(x_2 - h\tan\gamma_1)b\cos\theta}{l-(x_2 - h\tan\gamma_1)\sin\theta}$ and $\frac{(x_2 + h\tan\gamma_2)b\cos\theta}{l-(x_2 + h\tan\gamma_2)\sin\theta}$, respectively.

The displacement u_3 is calculated as follows:

$$u_3 = \frac{(x_2 + h\tan\gamma_2)b\cos\theta}{l-(x_2 + h\tan\gamma_2)\sin\theta} - \frac{(x_2 - h\tan\gamma_1)b\cos\theta}{l-(x_2 - h\tan\gamma_1)\sin\theta}$$

$$= \frac{\begin{array}{c}(x_2 + h\tan\gamma_2)lb\cos\theta - (x_2 - h\tan\gamma_1)(x_2 + h\tan\gamma_2)b\cos\theta\sin\theta \\ -(x_2 - h\tan\gamma_1)lb\cos\theta + (x_2 - h\tan\gamma_1)(x_2 + h\tan\gamma_2)b\cos\theta\sin\theta\end{array}}{\left[l-(x_2 + h\tan\gamma_2)\sin\theta\right]\left[l-(x_2 - h\tan\gamma_1)\sin\theta\right]}$$

$$= \frac{(x_2 + h\tan\gamma_2)lb\cos\theta - (x_2 - h\tan\gamma_1)lb\cos\theta}{(l - x_2\sin\theta - h\tan\gamma_2\sin\theta)(l - x_2\sin\theta + h\tan\gamma_2\sin\theta)}$$

$$= \frac{hlb\cos\theta(\tan\gamma_1 + \tan\gamma_2)}{(l - x_2\sin\theta)^2\left(1 - \frac{h\tan\gamma_2\sin\theta}{l - x_2\sin\theta}\right)\left(1 + \frac{h\tan\gamma_2\sin\theta}{l - x_2\sin\theta}\right)}. \quad \text{(2-35)}$$

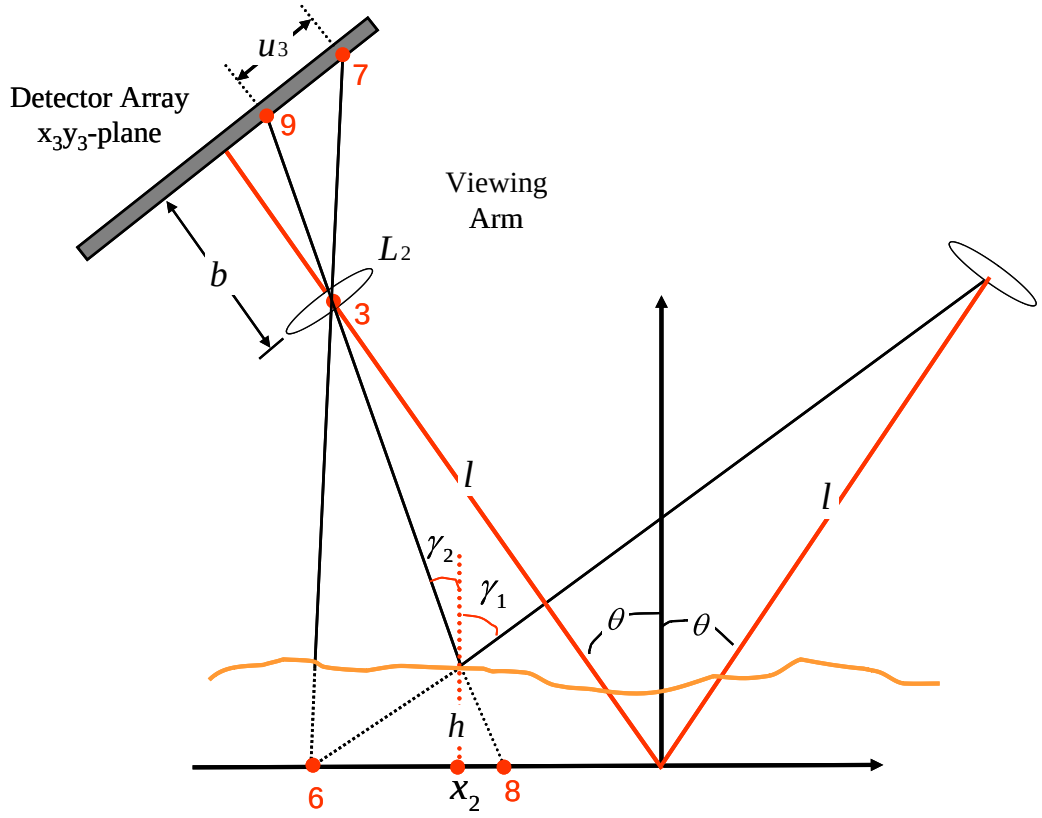

Figure 2-11. Illustration of the modification of the point image location due to the height profile *h*.

Since $h << l$, $x_2 << l$, $\sin\theta << 1$, and $\tan\theta << 1$, the second and third terms of the denominator of Equation 2-35 are well approximated by 1 and the equation becomes

$$u_3 = \frac{hlb\cos\theta(\tan\gamma_1 + \tan\gamma_2)}{(l - x_2\sin\theta)^2}. \tag{2-36}$$

From the geometry in Figure 2-11 and the approximation $h<<l$,

$$\begin{aligned} \tan\gamma_1 &= \frac{l\sin\theta + x_2}{l\cos\theta}, \text{ and} \\ \tan\gamma_2 &= \frac{l\sin\theta - x_2}{l\cos\theta}. \end{aligned} \tag{2-37}$$

Substituting (2-37) in (2-36), u_3 can be written as

$$u_3 = h\frac{2lb\sin\theta}{(l - x_2\sin\theta)^2}. \tag{2-38}$$

Equation 2-38 represents the displacement of the fringe image on the camera due to the object's height as a function of the point location on the object, x_2. In order to present u_3 as a function of x_1 (the original point location on the grating), substitute x_2 by its value from Equation 2-23:

$$\begin{aligned} u_3 &= h\frac{2lb\sin\theta}{\left(l - \dfrac{x_1 l_p\sin\theta}{a\cos\theta - x_1\sin\theta}\right)^2} \\ &= h\frac{2lb\sin\theta}{\left(\dfrac{la\cos\theta - lx_1\sin\theta - x_1 l\sin\theta}{a\cos\theta - x_1\sin\theta}\right)^2} \\ &= h\frac{2lb\sin\theta(a\cos\theta - x_1\sin\theta)^2}{\left(la\cos\theta - 2lx_1\sin\theta\right)^2}. \end{aligned} \tag{2-39}$$

Factor out $(a\cos\theta)^2$ from the nominator and $(la\cos\theta)^2$ from the denominator, Equation 2-39 becomes

$$u_3 = h\frac{2b\sin\theta}{l}\times\frac{\left(1-\frac{x_1\tan\theta}{a}\right)^2}{\left(1-\frac{2x_1\tan\theta}{a}\right)^2}. \tag{2-40}$$

A good approximation can be made here. Since $x_1\tan\theta << a$, the Taylor series expansion of the term $\left(1-\frac{x_1\tan\theta}{a}\right)^2$ is approximately $\left(1-\frac{2x_1\tan\theta}{a}\right)$. Using this relationship, Equation 2-40 becomes

$$u_3 = h\frac{2b\sin\theta}{l}\left(1-\frac{2x_1\tan\theta}{a}\right)^{-1} = h\frac{2\sin\theta}{M}\left(1-\frac{2x_1\tan\theta}{a}\right)^{-1}, \tag{2-41}$$

where ($M = \frac{l}{b}$) is the system magnification along the principal axis (at the origins of the coordinate systems).

Equation 2-41 represents the shift in the image location of the point x_1 on the grating due to the height profile of the object (h) as seen by the camera in a symmetric fringe projection system.

Finally, the intensity distribution of the fringes on the camera plane can be written as:

$$I = A + B\cos\left(\frac{2\pi}{\lambda_{x3}}\left[x_3 + u_3\right]\right). \tag{2-42}$$

To present I as a function of x_1, a relationship between x_1 and x_3 can be established using Equations 2-23 and 2-28 for a symmetric system:

$$x_2 = \frac{x_1 l}{a\cos\theta - x_1\sin\theta} = \frac{x_3 l}{b\cos\theta + x_3\sin\theta}$$

$$\Rightarrow x_3 = x_1\left(1 - \frac{2x_1\tan\theta}{a}\right)^{-1}. \tag{2-43}$$

Substituting Equations 2-34, 2-41, and 2-43 into 2-42, the fringe intensity distribution on the camera plane as a function of the point location on the grating (x_1) can be written as

$$I = A + B\cos\left(\frac{2\pi}{p}\left(1 - \frac{2x_1\tan\theta}{a}\right)^2\left[x_1\left(1 - \frac{2x_1\tan\theta}{a}\right)^{-1} + h\frac{2\sin\theta}{M}\left(1 - \frac{2lx_1\tan\theta}{a}\right)^{-1}\right]\right)$$

$$= A + B\cos\left(\frac{2\pi}{p}\left[1 - \frac{2x_1\tan\theta}{a}\right]\times\left[x_1 + \frac{2\sin\theta}{M}h\right]\right). \tag{2-44}$$

This equation can be written as:

$$I = A + B\cos(\phi + \psi), \tag{2-45}$$

where $\phi = \frac{2\pi x_1}{p}\left[1 - \frac{2x_1\tan\theta}{a}\right]$ represents the main phase (commonly called the carrier phase) of the measured fringes, and $\psi = \frac{2\pi}{p}\left[1 - \frac{2x_1\tan\theta}{a}\right]\frac{2\sin\theta}{M}h$, is the phase shift in the measured fringes introduced by the height profile of the object. Analyzing the measured fringe intensity maps, we can extract the value of ψ, and then the height profile h can be calculated by the following relation:

$$h = \frac{\lambda_{eq}}{2\pi}\psi\,, \tag{2-46}$$

where

$$\lambda_{eq} = \frac{Mp}{2\sin\theta}\left[1 - \frac{2x_1\tan\theta}{a}\right]^{-1}, \tag{2-47}$$

is the equivalent wavelength (or synthetic wavelength). This is the factor that is multiplied by the measured phase map to convert from phase to height values.

For the sake of completeness, its worth mentioning that to make a projection moiré system, another grating (commonly called the mask grating) is inserted just in front of the detector array, and hence the intensity distribution of the fringes seen by the detector array is going to be the multiplication of the transmittance function of the mask grating with the intensity distribution given by Equation 2-44.

Fringe projection and projection moiré techniques have been used in various metrology applications and are well described in the literature. For more information on the theory and applications, the reader should refer to references 31, 34, 17 and 79-85.

1.6.4.1 Illustration of the perspective effect

As mentioned above, looking at Equation 2-34, we see that the measured fringe period, λ_{x3}, is a function of the position x_1. This means that the fringes or grating projected onto a plane will not be composed of straight, equidistance lines, resulting in an apparent non-planar reference surface. This is called the perspective effect and leads to a

systematic bias in measurements made with this type of fringe projection system. The following Matlab™ simulation illustrates this effect.

In this simulation, $l_p = l_k = 128\ mm$, $\theta_1 = \theta_2 = 20^\circ$, the projected grating is sinusoidal of period $p = 1\,mm$, and the field of view is 12 *mm*. The grating is projected onto a flat surface, as shown in Figure 2-12. In the detector array plane, the intensity distribution of the fringes is given by Equation 2-44 after replacing *h* by zero to simulate a plane. The fringe period varies with the position x_1 as shown in Figure 2-13. Then, eight phase shifted frames are created by increasing the phase of Equation 2-44 by (π/2) for each frame, and then the frames are analyzed using Veeco's fringe analysis software Vision™. By analyzing these fringes, we can generate the optical path difference (OPD) map, shown in Figure 2-14. Note that the map is not a plane, rather it is cylindrical. The curvature of this map increases by increasing the field of view.

As mentioned above, the perspective effect is considered a systematic bias in the system and has to be either eliminated or corrected for. Two methods are briefly described to overcome this problem in the following subsection.

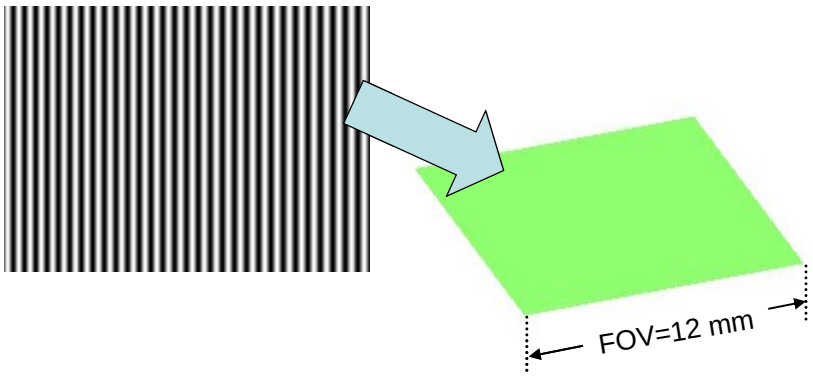

Figure 2-12. Straight sinusoidal equidistance fringes of period p = 1 mm projected onto a flat surface. The total field of view FOV is 12 mm.

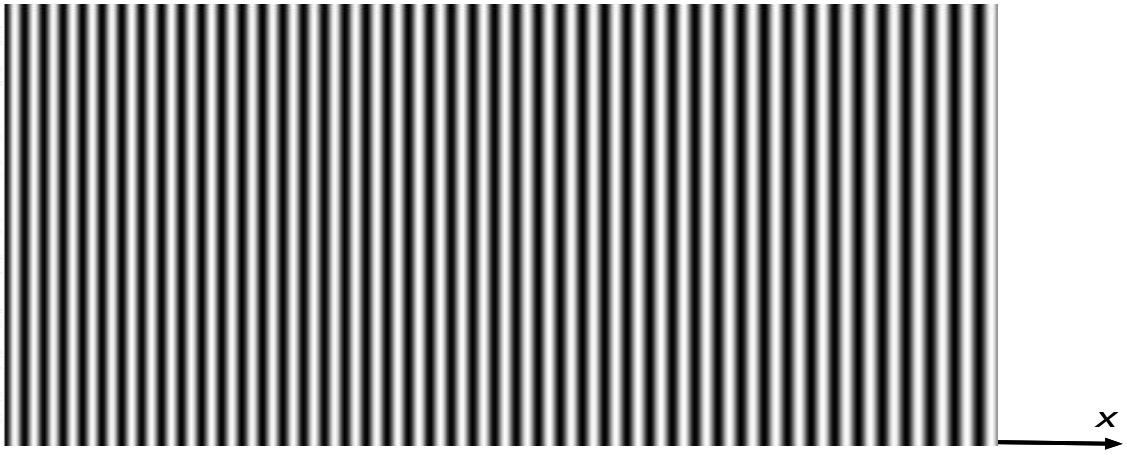

Figure 2-13. Fringes after being projected onto a flat surface. Notice the variation of the wavelength with x.

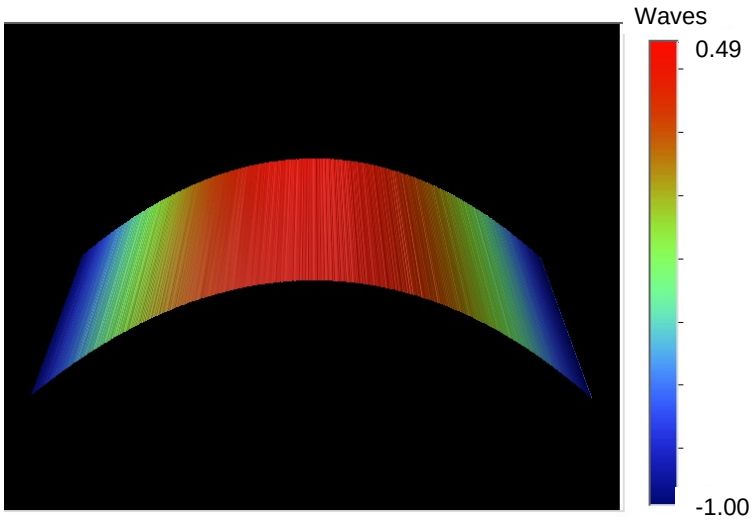

Figure 2-14. OPD map of the flat surface as measured by the fringe projection system for total field of view of 12 mm.

1.6.4.2 Eliminating the perspective effect using telecentric lenses

With a conventional lens, the image of an object appears larger if it is closer to the imaging lens, meaning that the magnification changes with the object distance. This is clear from the thin lens equation [86].

In telecentric lens systems, the magnification is constant, So an object will have the same image size regardless of its distance from the lens. This is done by introducing an aperture stop at the rear principal focal plane of the lens and making the focal point located at the center of the aperture as shown in Figure 2-15. In such a setup, the chief rays will always be parallel to the lens principal axis, regardless of the position of the object, resulting in a constant system magnification. For more details on telecentric lenses refer to references 86- 88.

Using telecentric lenses for projecting and viewing arms in a fringe projection system will cause the period of the measured fringes to be constant over the field of view since all the chief rays coming in and out of the telecentric lenses will be parallel as shown in Figure 2-16.

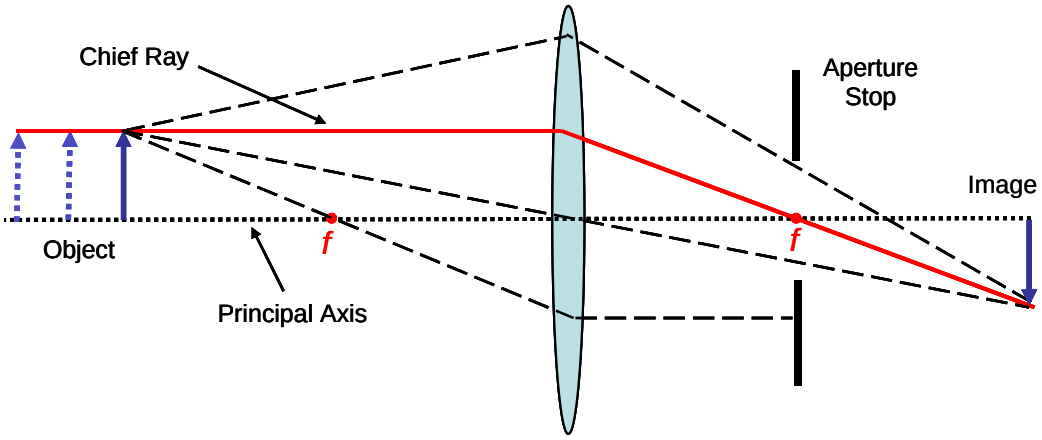

Figure 2-15. Telecentric lens setup. Notice that the chief ray is always parallel to the principal axis regardless of the object position.

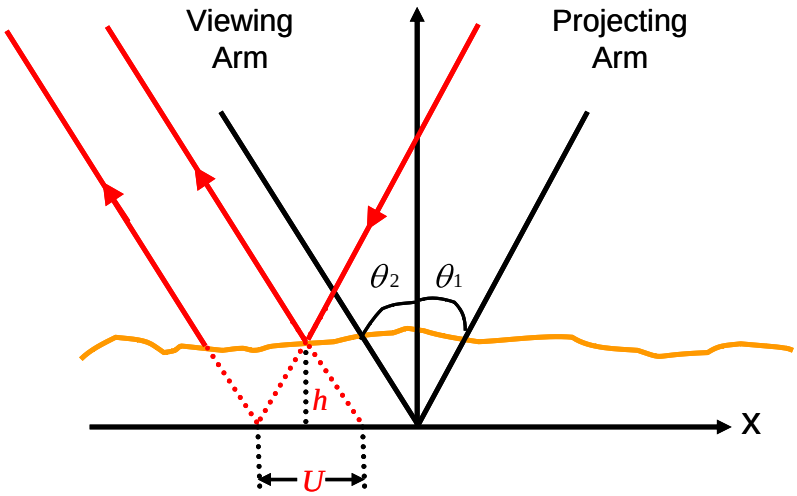

Figure 2-16. Fringe projection using telecentric lenses.

If the system has the same magnification for projection and viewing, defined by M, the fringe period detected by the camera will be constant and equal to p, where p is the period of the grating. From Figure 2-16, the fringe displacement caused by the object's height, h, on the object plane is given by

$$U = h(\tan\theta_1 + \tan\theta_2). \tag{2-48}$$

The corresponding displacement on the camera plane, u is then given by

$$u = \frac{U}{M} = \frac{h(\tan\theta_1 + \tan\theta_2)}{M}, \tag{2-49}$$

where M is the system magnification as mentioned above. The phase shift in the fringe intensity map is then given by

$$\psi = \frac{2\pi}{p}u = \frac{2\pi h(\tan\theta_1 + \tan\theta_2)}{Mp}, \tag{2-50}$$

and hence, the height profile is calculated using the following relationship:

$$h = \lambda_{eq} \times \frac{\psi}{2\pi} = \frac{Mp}{\tan\theta_1 + \tan\theta_2} \times \frac{\psi}{2\pi}. \quad (2\text{-}51)$$

For a symmetric system, $\theta_1 = \theta_2 = \theta$, and Equation 2-51 becomes:

$$h = \frac{Mp}{2\tan\theta} \times \frac{\psi}{2\pi}. \quad (2\text{-}52)$$

From Equation 2-52 we see that using telecentric lenses for projection and viewing makes the equivalent wavelength constant and a flat reference surface will be measured as a plane. The equivalent wavelength can be measured either by knowing the system parameters or by calibration as described in Chapter 4. Telecentric lenses are used in different fringe projection systems reported in the literature [83-85].

1.6.4.3 Eliminating the perspective effect by projecting a custom grating

The other method of eliminating the perspective error is to make a special projection grating whose projection on a reference plane will give a constant equivalent wavelength and eliminate the additional apparent height added to the surface. This method was used in references 71 and 89-91.

From Section 2.3.4, we saw that by projecting a grating with a constant period (*p*), the fringe intensity distribution detected by the camera is given by Equation 2-44 which shows that the main period of the detected fringes is given by

$$\lambda_3(x_1) = \frac{p}{1 - \frac{2x_1 \tan\theta}{a}}. \quad (2\text{-}53)$$

In a system free of biases, the detected fringes should have the same period as the gratings (assuming the same magnification for both projection and viewing arms). Hence, we want to project a custom grating with variable period, say p_2, that will correct for the bias and generate fringes on the camera plane with a constant period $\lambda_3(x_1) = p$. The variable pitch, p_2, can be calculated from Equation 2-53:

$$\lambda_3(x_1) = \frac{p_2}{1 - \frac{2x_1 \tan\theta}{a}} = p$$

$$\Rightarrow p_2 = p \times \left(1 - \frac{2x_1 \tan\theta}{a}\right). \tag{2-54}$$

Using the simulation used in Section 2.3.4.1, the new fringes with period p_2 will look opposite of the detected fringes in Figure 2-13. This is shown in Figure 2-17.

The intensity distribution after projecting p_2 is now given by Equation 2-44 after replacing p by p_2:

$$I = A + B\cos\left(\frac{2\pi}{p_2}\left[1 - \frac{2x_1 \tan\theta}{a}\right] \times \left[x_1 + \frac{2\sin\theta}{M}h\right]\right)$$

$$= A + B\cos\left(\frac{2\pi}{p\left[1 - \frac{2x_1 \tan\theta}{a}\right]} \times \left[1 - \frac{2x_1 \tan\theta}{a}\right] \times \left[x_1 + \frac{2\sin\theta}{M}h\right]\right)$$

$$= A + B\cos\left(\frac{2\pi}{p} \times \left[x_1 + \frac{2\sin\theta}{M}h\right]\right). \tag{2-55}$$

The phase shift (ψ) due to the object's height (h) is now given by:

$$\psi = \frac{2\pi}{p} \times \frac{2\sin\theta}{M} h, \tag{2-56}$$

and hence, *h* can be written as:

$$h = \frac{\psi}{2\pi} \times \frac{Mp}{2\sin\theta} = \frac{\psi}{2\pi} \times \lambda_{eq}. \tag{2-57}$$

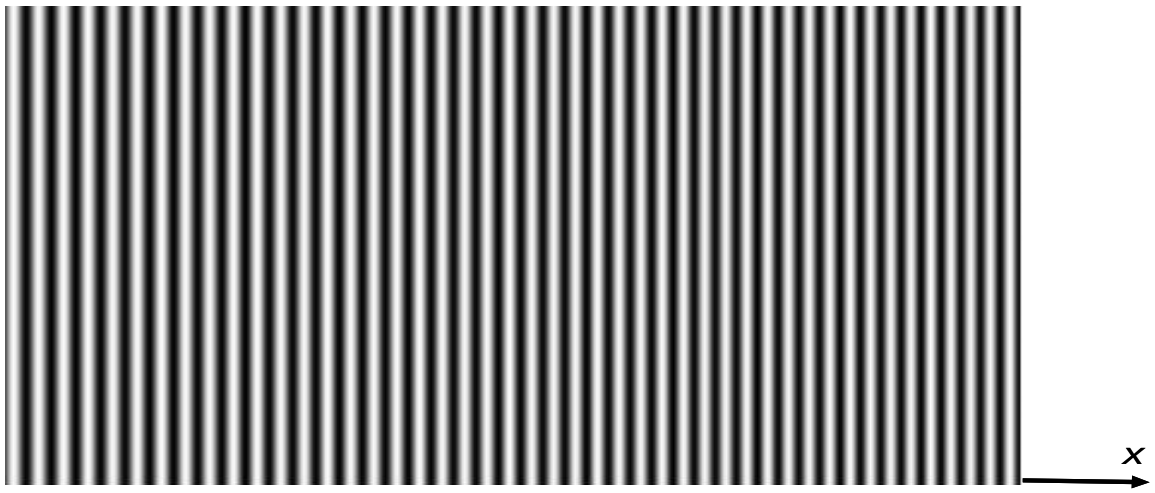

Figure 2-17. The new projected fringes with period p_2. Notice that they are the opposite of the fringes in Figure 2-13.

Equation 2-57 shows that the equivalent wavelength is now constant. It can be estimated either by knowing the system parameters or by calibrating the system as describer later in Chapter 4.

In this project we used the method of projecting a custom grating to correct for the systematic biases in our system. The details of this procedure and the creation of the custom grating from measured data are described in Chapter 4.

CHAPTER 3: DYNAMIC RANGE ENHANCEMENT AND WAVINESS FILTERING TECHNIQUE

1.7 Introduction

Laser interferometers have been widely used in surface profiling for many years. Combined with phase shifting techniques, these interferometers have proven to be very accurate and powerful. However, they suffer from a limited dynamic range. It can easily be shown that in phase shifting interferometry the height difference between two adjacent data points should be less than $\lambda/4$ for the phase to be resolved without ambiguities, where λ is the wavelength of the light used [92]. In fringe projection and moiré techniques this range is $\lambda_{eq}/2$ since it is equivalent to single pass interferometers, where λ_{eq} is the equivalent (effective) wavelength of the system.

Another factor that limits the dynamic range in both classical interferometers and fringe projection systems is that the fringes become very dense on surfaces with high slopes such that the imaging system is not able to resolve them. The following simulation illustrates this limitation. The simulation is done in a similar way described in Section 2.3.4.1. In this simulation, we model a fringe projection system with a 10^{o} projecting and viewing angles and a magnification of 2×. Consider the object shown in Figure 3-1. The object consists of a large dome-shaped low spatial frequency object of 0.5 mm height, with much smaller size and higher frequency features on top with height of 0.05 mm. The size of the small features is exaggerated in the figure for a better visual. The large dome

shape is considered as the waviness of the surface and the small features are the surface roughness. In fringe projection, high frequency fringes are needed to resolve the small features, and since the object profile is much larger than the surface finish, the projected fringes will be significantly deformed by the large profile. Consequently, the fringes will become very dense and irresolvable by the system. Figure 3-2-(a), shows the simulated projected high frequency fringes with an equivalent wavelength of 10 μm, and Figure 3-2-(b) shows the fringes after being deformed by the object and Figure 3-2-(c) shows the object's optical path difference map (OPD) reconstructed from the fringes in Figure 3-2-(b). The figure clearly demonstrates the system's failure to resolve the surface profile. If a low frequency grating is projected so the fringes can be resolved by the system, the resolution is insufficient to measure the small features as demonstrated in Figure 3-3 (a), (b), and (c).

To clarify how a system looses its capability of detecting small feature sizes by increasing the equivalent wavelength, consider one of the high resolution fringe projection systems reported in the literature [93]. The system has a maximum vertical resolution in the range of 0.5 μm with an equivalent wavelength of 10 μm and a maximum lateral resolution of 0.05 μm. From these numbers we conclude that an object which has a 0.5 μm height causes a lateral shift in the projected fringes of 0.5/10 = 0.05 μm, which is equal to the system's lateral resolution, and therefore, the system is able to measure it. Now, assume that the system's grating is replaced by a lower frequency one that changes the equivalent wavelength to 50 μm. The 0.5 μm object will introduce a

lateral shift in the projected fringes of 0.5/50 = 0.01 μm, which is lower than the system's lateral resolution and therefore the system will not be able to measure this feature any more.

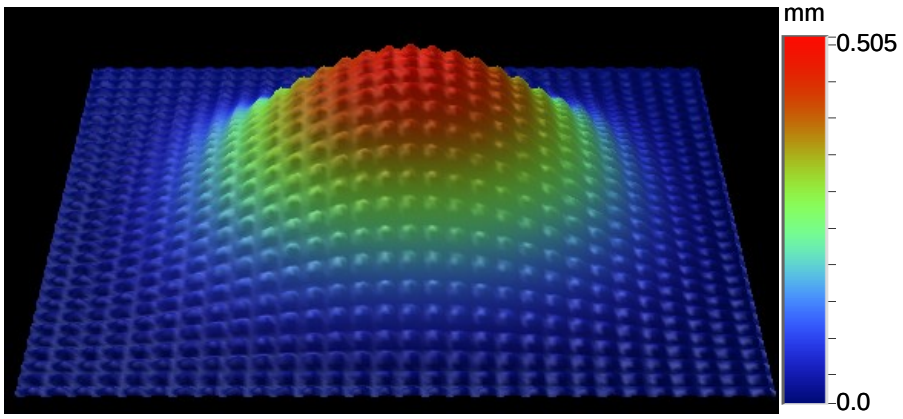

Figure 3-1. Object with low-frequency, large dome-shaped profile (waviness), with small high-frequency features (roughness) on top.

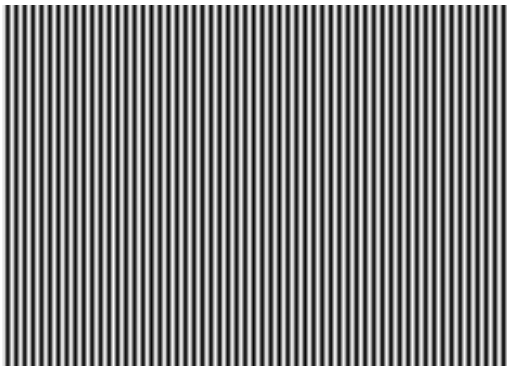

(a)

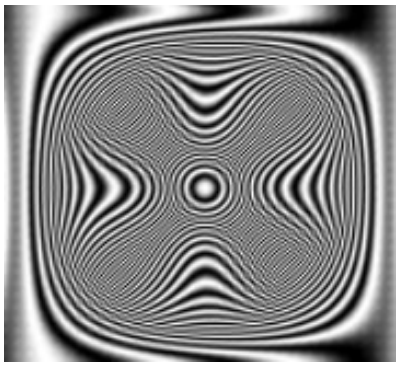

(b)

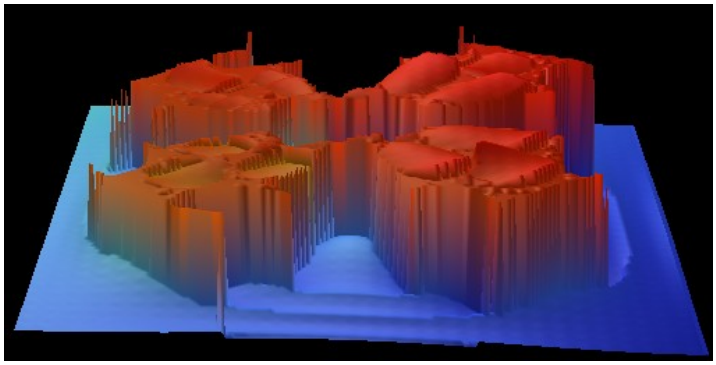

(c)

Figure 3-2. (a) The high frequency projected fringes. (b) The fringes deformed by the large object's profile (irresolvable by the system). (c) The reconstructed OPD map.

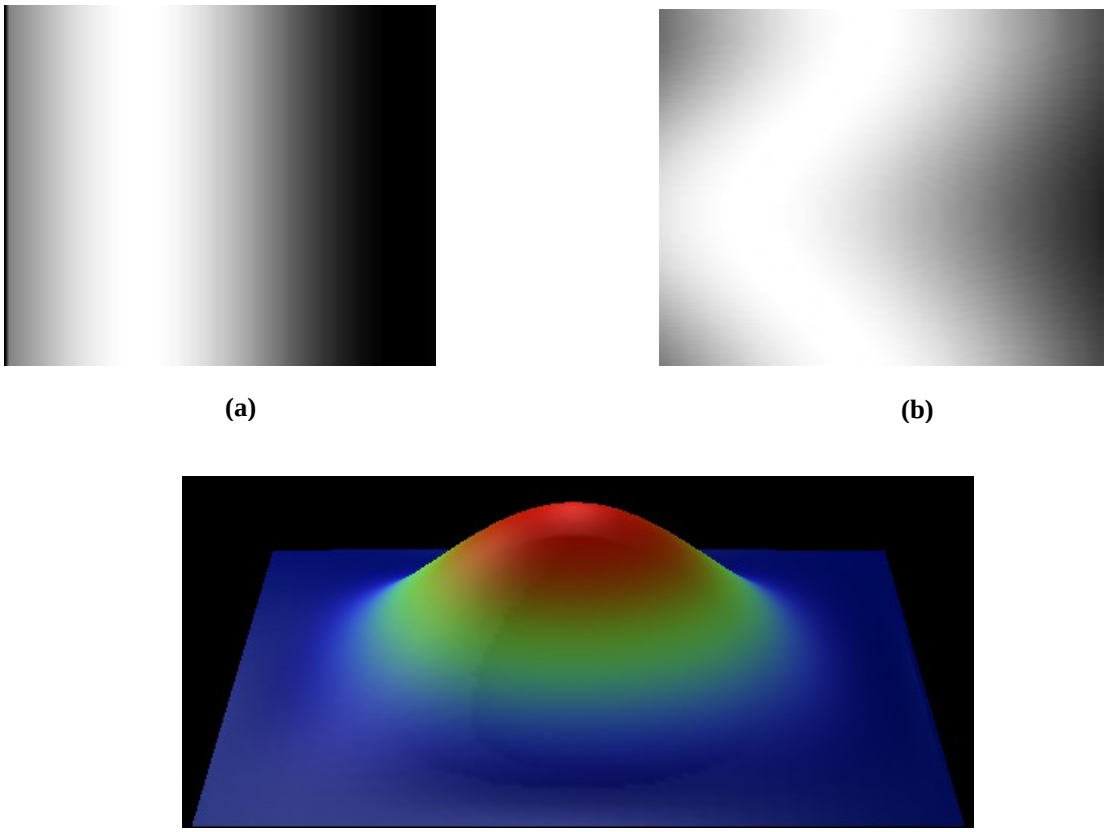

(a) **(b)**

(c)

Figure 3-3. (a) The low frequency projected fringes. (b) The fringes deformed by the large object's profile (resolvable by the system). (c) The reconstructed OPD map which has no information about the desired small features.

In this chapter, we propose and simulate a real time inverse fringe projection technique to overcome this limitation and enhance the dynamic range without reducing the vertical resolution. Inverse fringe projection (commonly called object-adapted fringes) is discussed in the literature [94- 97]. In these systems the inverse fringes are created by calculating the theoretical position of the grating lines so that when they are projected on a master object, they will be observed by the camera as straight lines. This

requires precise measurements of the system's parameters and the master object's dimensions. In this work, the inverse fringes are created in real time without the need to have prior information about the surface or the system's parameters. The object's waviness OPD map is measured and used to generate the inverse fringes to optically filter out this waviness, and then the surface finish is measured without the impact of the large form. The technique can be applied in several steps to focus on specific spatial frequencies at a time.

1.8 Simulation of dynamic range enhancement and waviness filtering

In the following simulation, Matlab™ was used to create gratings and simulate the fringe projection. Veeco Instruments' fringe analysis software (Vision™) was used to analyze fringes.

Matlab™ is used to simulate a symmetric fringe projection system like the one described in section 2.3.4, with the following parameters:

$\theta_1 = \theta_2 = 10°$,

$l_p = l_k = 70\ mm$,

$a = b = 140\ mm$,

$M = \frac{l_k}{b} = 0.5$.

Consider the same object shown in Figure 3-1. The object has a large, low-frequency profile (waviness) given by

$$h_1 = 0.5\left[\cos\left(\frac{2\pi}{11}x\right)\cos\left(\frac{2\pi}{11}y\right)\right]^2 mm \quad , \tag{3-1}$$

and a small, high-frequency features (roughness) given by

$$h_2 = 0.005\left[\cos\left(\frac{2\pi}{0.5}x\right)\cos\left(\frac{2\pi}{0.5}y\right)\right]^2 mm \ . \tag{3-2}$$

The overall height profile of the object is

$$h = h_1 + h_2 \ . \tag{3-3}$$

First, in order to ensure that our system is capable of measuring the dome profile without ambiguity, we choose the system parameters such that the equivalent wavelength is larger than twice the height of the dome. Consequently, we project a straight sinusoidal pattern with period $p_1 = 2mm$ as shown in Figure 3-4. Assuming a telecentric system, the equivalent wavelength is calculated using the following equation: $\lambda_{eq} = \frac{Mp_1}{2\tan(\theta)} = \frac{0.5 \times 2}{2\tan(10)} = 2.8mm$, which is larger than twice the height of the dome. The pattern then gets deformed by the object as shown in Figure 3-5.

Figure 3-4. The projected straight sinusoidal fringes with 2mm period.

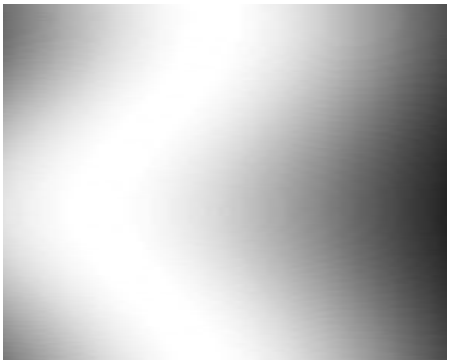

Figure 3-5. The fringes after being deformed by the object as seen by the camera.

Phase shifting is applied to generate the surface height profile from the fringes. The surface phase map is first generated and then multiplied by the equivalent wavelength. Figure 3-6 shows the generated height profile. The figure clearly shows that the profile obtained by the system does not include information about the surface finish (only h_1 is measured). This is not surprising since we initially chose a large effective wavelength by using the period of the initial pattern to be *2 mm* in order to have a measurement range greater than double the object's height. This choice, while necessary to determine the

general form of the object, reduces the vertical resolution of our system such that it can no longer resolve the surface finish. This is the fundamental limitation of basic interferometers as described in Section 3.1.

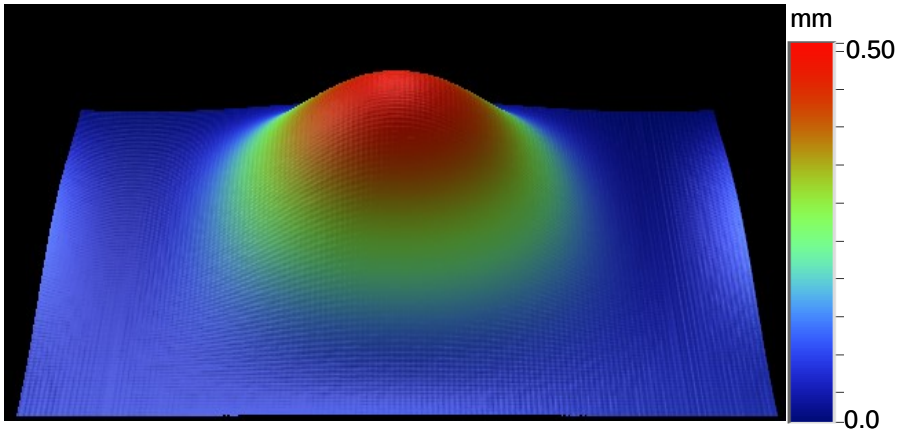

Figure 3-6. Generated object profile using the 2mm fringes. The object does not include any information about the surface finish.

Our next step is to increase the resolution while maintaining the measurement range. Our solution is to filter out the large profile of the object by projecting a pre-deformed periodic pattern that has the opposite deformation of what is shown in Figure 3-5. This can be done by replacing the grating in our system with a spatial light modulator (SLM). The object will then impact this pattern in the opposite direction and consequently produces straight fringes. Figure 3-7 and Figure 3-8 show the pre-deformed pattern and the same intensity pattern after being impacted by the surface, using the 2.8 mm effective wavelength.

As before, phase shifting is used to obtain the phase information. Figure 3-9 represents the three dimensional phase profile of the object. As we can see, the phase profile obtained by this method represents a flat surface. This shows that the large profile was successfully filtered out by projecting the proper pre-deformed fringes.

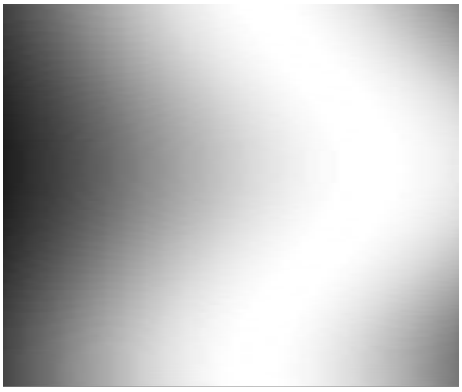

Figure 3-7. The pre-deformed projected fringes with 2mm period.

Figure 3-8. The fringes after being impact by the object as seen by the camera.

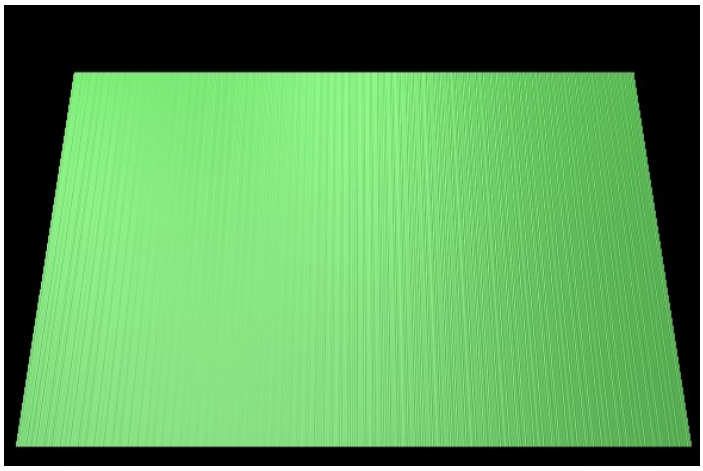

Figure 3-9. The height profile after filtering out the waviness. Still no information about the surface finish since the fringe period was 2mm.

To measure the surface finish, we propose to project a different pattern than that shown in Figure 3-7. The proposed pattern is also deformed in the same manner, however, the frequency of this pattern is much higher, and consequently the effective wavelength much shorter. For example, we choose this frequency to be 10 times higher than before. Therefore, the pitch of this pattern will be *0.2 mm* in comparison with *2 mm* in our earlier analysis.

Figure 3-10 depicts the proposed projected pattern. As before, the fringes are deformed by the large profile producing straight lines, except now they are significantly deformed by the high frequency surface roughness, as shown in Figure 3-11. The phase of this pattern is then analyzed as before to obtain the surface finish shown in Figure 3-12. Finally, the overall object height is the summation of the surface finish and the low

frequency profile as shown in Figure 3-6. The final object profile is shown in Figure 3-13.

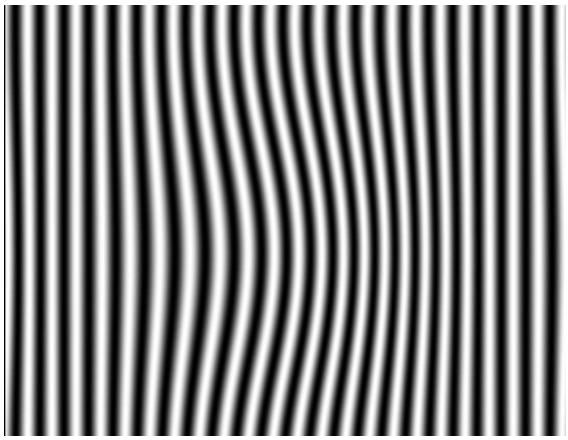

Figure 3-10. The projected pre-deformed fringes with 0.2 mm period.

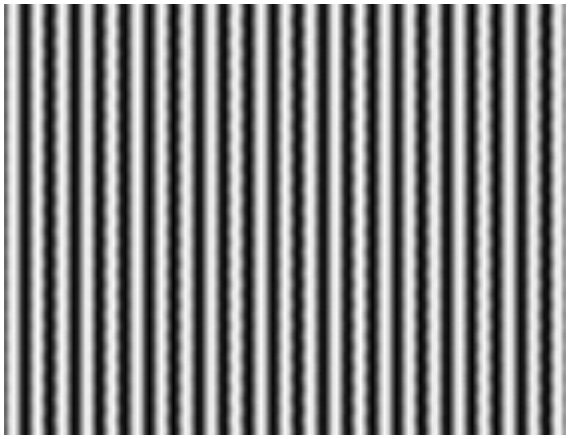

Figure 3-11. The fringes after being deformed by the large profile. The fringes are now deformed by the surface roughness only.

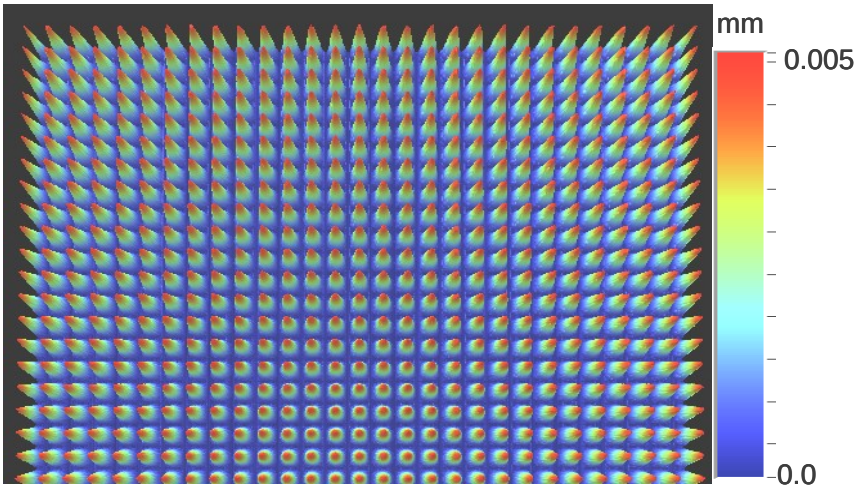

Figure 3-12. Surface finish obtained by analyzing the fringes in Figure 3-11.

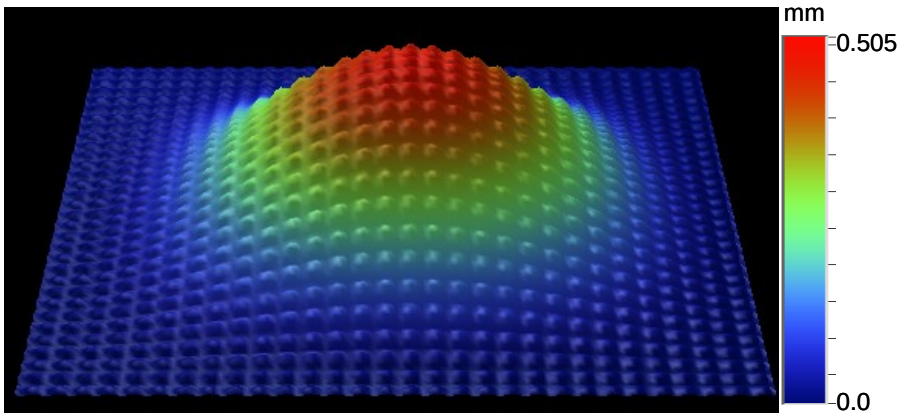

Figure 3-13. Final surface height profile

The same idea can be used to improve the dynamic (vertical) range of laser interferometers. Currently, parts with significant dimensional departure from a sphere or

a plane are measured with an interferometer by using a ‘null’ optic or they are measured with a profilometer. These measurements are either slow or expensive, and there is a need for a rapid, flexible and inexpensive alternative. A spatial light modulator (SLM) can be used to deform a wavefront so that the wavefront is the inverse shape of the geometric form of the surface. The SLM can be used in either a diffractive or transmissive mode to modify the wavefront, essentially functioning as a variable null optic. Then, once the modified wavefront reflects from the surface it will become nearly flat. Or alternatively, one could design the system so the reflected wavefront was nearly spherical. Once the reflected wavefront is nearly flat or spherical, a laser interferometric measurement will yield information about the departure of the surface from the shape of the incident wavefront, allowing the measurement of the surface waviness and roughness. Of course, the measurement uncertainty will be limited by the degree to which the SLM is repeatable and calibrated.

CHAPTER 4: FRINGE PROJECTION SYSTEM: HARDWARE, SOFTWARE, METHODOLOGY AND EXPERIMENTAL RESULTS

1.9 Hardware

To illustrate the dynamic range enhancement and waviness filtering technique, we had to consider a device that would allow us to generate gratings with variable frequencies and forms. Digital Spatial Light Modulators (SLM) provide such functionality. They are electro-optical devices that consist of arrays of optical elements (pixels), in which each pixel is digitally controlled to adjust or modulate light intensity or phase [106]. There are three types of digital SLM technologies, Liquid Crystal Display (LCD), Digital Light Processing (DLP) and Liquid Crystal Over Silicon (LCOS). From their names, LCD and LCOS technologies use liquid crystals (one for each pixel) to modulate the light by changing its polarization and/or phase. LCD panels contain two polarizing sheets and several layers of liquid crystals sandwiched between them. Light passes through these LCD panels, and is modulated by the liquid crystals as it passes. In

the LCOS technology, the liquid crystals are applied to a reflective mirror substrate. As the liquid crystal is modulated, the light is either reflected from the mirror below, or blocked [107]. Finally, DLP uses micro electro-mechanical mirrors (MEMS), one for each pixel, to reflect light. DLP modulates the light by tilting the mirrors either into or away from the imaging optics.

In addition to the advantage of providing variable frequency and form, SLM gratings have the ability to provide accurate phase shifting and a contrast close to that provided by the conventional gratings [101].

The cost of SLMs increases rapidly with the resolution. The smaller the pixel size the higher the resolution and the more expensive the SLM module becomes. For instance, the DLP chip module from Texas Instruments with a resolution of 1024 × 768 pixels and the control electronics is around $10,000 [102]. The same price range applies to LCD SLMs from companies such as HoloEye and Bolder Optics.

To overcome the price limitation, we used an LCD digital projector connected to a computer as our grating generator. An LCD projector contains 3 LCD SLMs as shown in Figure 4-1. Each SLM has a color filter placed in front of it, red, green and blue. A uniform white light beam passes through each filter-SLM combination, is modulated by the SLM, and then combined by a prism to generate the full color image. We used a projector made by 3M, model (MP7740i), with poly-silicon LCDs of resolution 1024×768 pixels and dimensions 14.4×10.8 mm. The projector uses a halogen lamp as a white light source with a maximum power of 1200 lumens. Figure 4-2 shows a schematic of our fringe projection system. The original projector lens was replaced by a Cannon zoom lens that creates a de-magnified image of the grating on the x_1y_1-plane, which is called the grating plane in Figure 4-2. This lens magnification was adjusted so that the final image on the camera plane covers the detector area. The system is shown in Figure 4-3.

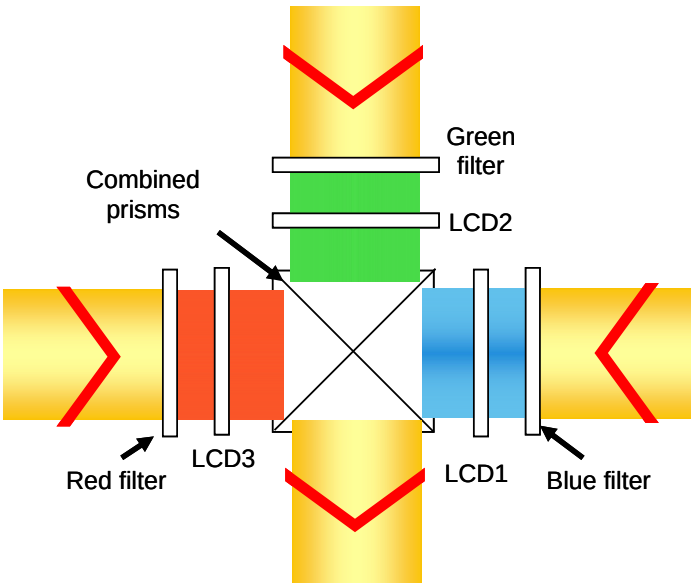

Figure 4-1 LCD projector, colored image generation schematic.

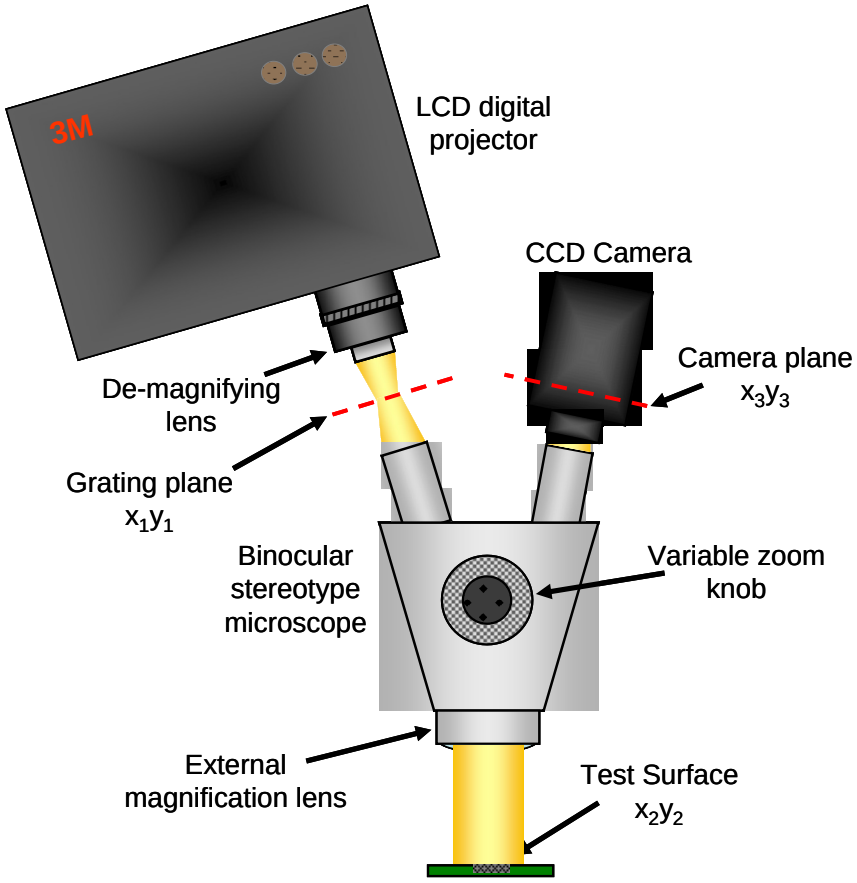

Figure 4-2. Stereotype microscope-based fringe projection system schematic.

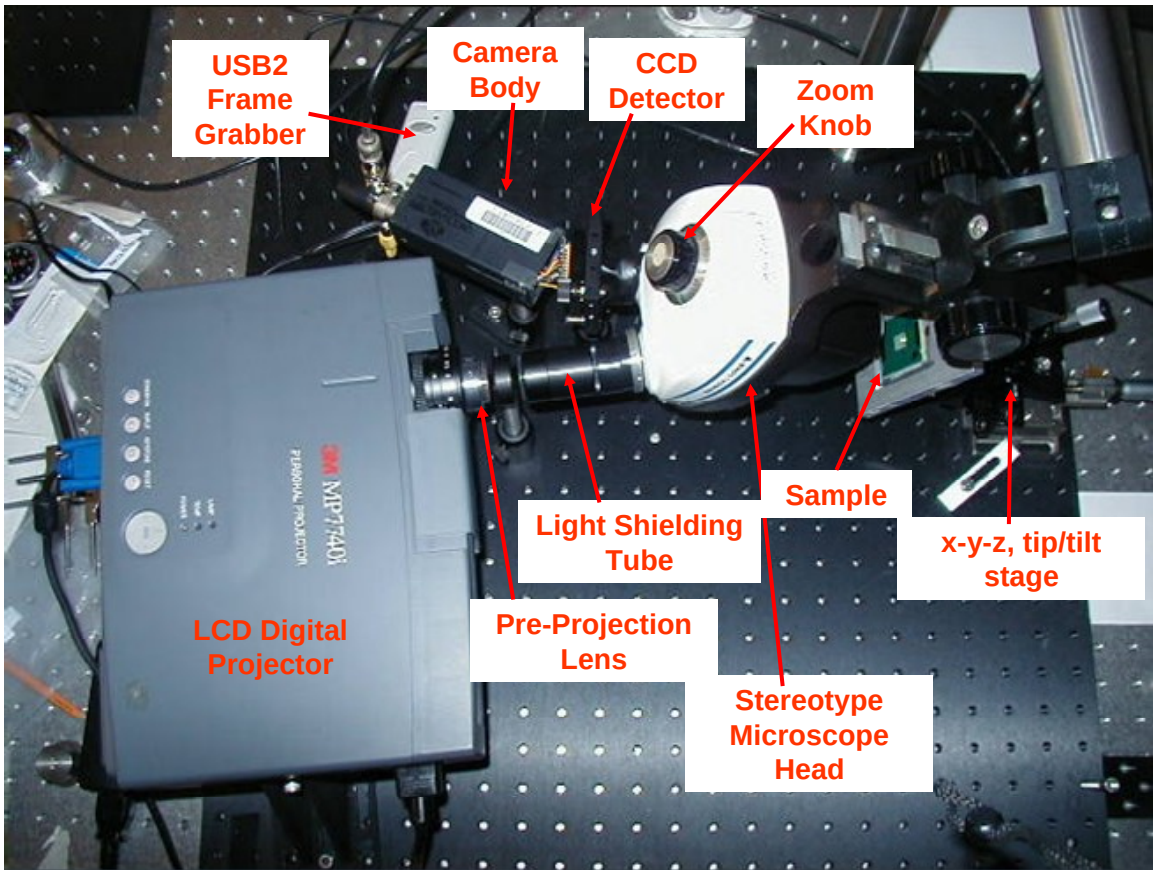

Figure 4-3. Setup of our fringe projection system.

Starting from the x_1y_1-plane in Figure 4-2, the system is symmetric just like the one described in Chapter 2. The projection and viewing arms of the system are replaced by a binocular stereotype zoom microscope (model: Bausch & Lomb Stereo Zoom4) with a 2× external magnifying lens. The grating image formed on the x_1y_1-plane is imaged again through one channel of the stereo microscope and projected onto the test surface (the x_2y_2-plane). The surface is then imaged through the other channel of the stereo microscope onto a CCD camera (the x_3y_3-plane). The camera is a Sony (XC-77) CCD

with a maximum resolution of 768 x 512 pixels. The image is then converted into a digital format using a frame grabber. The total zoom range of the stereo microscope is 1.3 - 5.8 enabling a field of view between 1.2 × 0.9 mm and 5.3 × 4.1 mm.

Stereotype microscopes have been used in fringe projection systems and reported in the literature [99105]. One advantage is that they assure the symmetry of the system, which makes the mathematical modeling much easier and the approximations more accurate. A second advantage is the integrated zoom that allows variable field of views with different scales and resolutions. The final advantage is that the basic parts of the stereo microscope consist of rigid, standard, and high quality components. The main disadvantage is that they introduce systematic biases caused by the perspective effect. The principle of stereo imaging depends on the perspective effect to create 3D images; therefore, stereotype microscopes are non-telecentric. Consequently, the perspective error has to be corrected as discussed in Section 2.3.4.3. Another disadvantage is the small projecting and viewing angles which minimizes the system's sensitivity.

1.10 Software

Matlab7^{TM} Release 14 was used to write the algorithms for the system control, which includes creating and projecting fringes with different frequencies and forms, applying phase shifting, capturing frames through the frame grabber, and then performing image pre-processing to prepare the frames for analysis. The Image Acquisition Toolbox in Matlab is needed to control the frame grabber.

A basic surface measurement is performed using the function "*projecting_function*" which contains the following algorithm:

1- Define the fringe period in millimeters and assign it to a variable, *p*. The fringe period is defined on the x_1y_1 plane (see Figure 4-2).

2- Create a 640 × 480 matrix (called *straight_fringes_double*) that contains a gray intensity image of sinusoidal straight fringes of a period determined by *p* in double precision format using the function $I = 1 + \sin(\frac{2\pi}{p}x)$.

3- Display the fringe intensity image on the screen using the function *display_full_screen* that takes the image and resizes it to cover the whole screen.

4- Grab the first image, which has a resolution of 640 × 480 by default, and store it in a three dimensional matrix called *fringes*. Eventually, this matrix contains all the captured frames through one complete measurement cycle. The size of this matrix is 640 × 480 × D, where D is the number of the phase shifting steps.

5- Apply phase shifting by adding π/2 to the phase of the sine function used in step 2, then repeat steps 3 and 4.

6- Repeat the sequence 5 – 3 – 4 until the desired number of frames is captured.

The algorithm will allow you to repeat the measurement as many times as desired and then perform an average for noise reduction.

The output of this algorithm is a matrix called *fringes*. If the eight phase shift algorithm is applied, this matrix contains 8 frames, each frame is a 640 × 480 pixels

intensity image of the fringes impacted by the test surface, and each frame is phase shifted by $\pi/2$ compared to the previous frame.

After the phase-shifted frames are acquired, they are converted to a form readable by Veeco Instrument's fringe analysis software, Vision™, for analysis. This is done using a set of Matlab™ .m files provided by Veeco for the Vision-Matlab interface. The function *"WriteFrames(filename, frames)"* accepts a matrix *"frames"* that contains the 8 phase-shifted interferograms, and writes it to the file *"filename.p2"* that can be processed by Vision. The file is then saved in the same folder where Vision is installed.

In order for Vision to analyze external interferograms, the measurement default options should be changed. This is done by opening in Vision the "Hardware" option from the drop down menu, and then selecting "Measurement Setup" and the "PSI Options" tab. In the "Phase Algorithm", the "Read Frames" check box must be checked and the phase shifting algorithm files you wish to use selected through the "browse" button. There are several options, 4-frames, 5-frames, 6-frames and 8-frames algorithms.

After selecting your phase shifting algorithm, press open, and this will take you back to the "PSI Options" menu. In the "Phase UnWrapping" drop down menu, you can choose a phase unwrapping algorithm. In most of the measurements taken by our system, the "Enhanced2" algorithm was used, since it proved to work with the most complicated interferograms with poor contrast and many discontinuities.

After selecting the PSI options, Vision is ready to analyze the interferograms. This is done by selecting “New Measurement” from the “File” options at the drop down menu. The interferograms will be analyzed and an OPD map is generated.

Since Vision is originally used for Veeco’s laser interferometers, the default wavelength is set to 632 nm. For our application, we want the height values in all generated OPD maps to be presented in waves so they can be multiplied by the system’s equivalent wavelength to give the correct height values. This can be done by selecting “Hardware Setup” from the “Hardware” drop down menu and then choosing the “Available Filters” tab. A list of all available default wavelengths appears. Change the numbers under the “Wavelength(nm)” list to 2, to set each fringe (wave) to be equal to 1 nm. Consequently, all OPD maps from now on will be presented in waves. (The units for the heights on the OPD graphs will stay in nanometers, but each nanometer now represents one wave).

For the lateral dimensions, the default field of view is set to 128 × 96 μm, which is used for the 5× magnification with Veeco’s interferometer. For our application, we need to normalize this number so the FOV becomes 640 x 480 μm, so each micrometer represents one pixel. Then for every FOV we use, we calibrate the system using a lateral calibration artifact, as discussed in Section 4.4.3 to find the pixel-to-micrometer conversion factor to find the correct lateral dimensions. The lateral dimension default can be changed by going to the “Hardware Setup” from the “Hardware” drop down menu, selecting the “Available FOV Lenses” tab, and changing the magnification under the

"Mag" list to 1. (The lateral units on the OPD maps will still be in micrometer, but each micrometer now represents one pixel).

1.11 Methodology

This section provides detailed models of, and procedure descriptions for system bias correction, measuring a surface profile, waviness filtering and surface finish measurement.

1.11.1 System biases correction and general surface height measurement

In Section 2.3.4.3 we showed that the perspective error can be eliminated by projecting a special pre-deformed grating whose projection on a reference plane will give a constant equivalent wavelength. This method is used to correct the systematic biases in our system as described below.

To ensure the coordinate system compatibility, our system is modeled as a basic fringe projection system similar to the one shown in Figure 2-10. As mentioned above, the de-magnifying lens attached to the projector and shown in Figure 4-2 was adjusted so that the final image covers the CCD detector array. Since we always resize the intensity image of the projected fringes to cover the whole computer monitor, and hence cover the SLM, this lens has no effect in the overall system magnification. Therefore, the grating plane is assumed to be located on the x_1y_1 plane shown in Figure 4-2.

The basic model of the system is shown in Figure 4-4. Notice that the distances a and b are greater than the distances l_p and l_k, respectively, since the object image is

magnified. It is difficult to measure the system parameters accurately. Instead, the system is calibrated using a standard VLSI step height, described later. The approximate parameter values are shown in Figure 4-4 .

The modeling begins by projecting straight sinusoidal fringes onto a flat surface. In Chapter 2, we showed that projecting straight fringes with a fixed period (p_1) on a flat surface will produce a fringe intensity distribution on the CCD plane given by

$$I = A + B\cos\left(\frac{2\pi}{p_1}\left[1 - \frac{2x_1 \tan\theta}{a}\right]x_1\right). \tag{4-1}$$

Analyzing these fringes produces a phase map given by

$$\phi_1 = \frac{2\pi}{p_1}\left[1 - \frac{2x_1 \tan\theta}{a}\right]x_1$$

$$= \frac{2\pi}{p_1}x_1 - \frac{2x_1^{\,2} \tan\theta}{ap_1}. \tag{4-2}$$

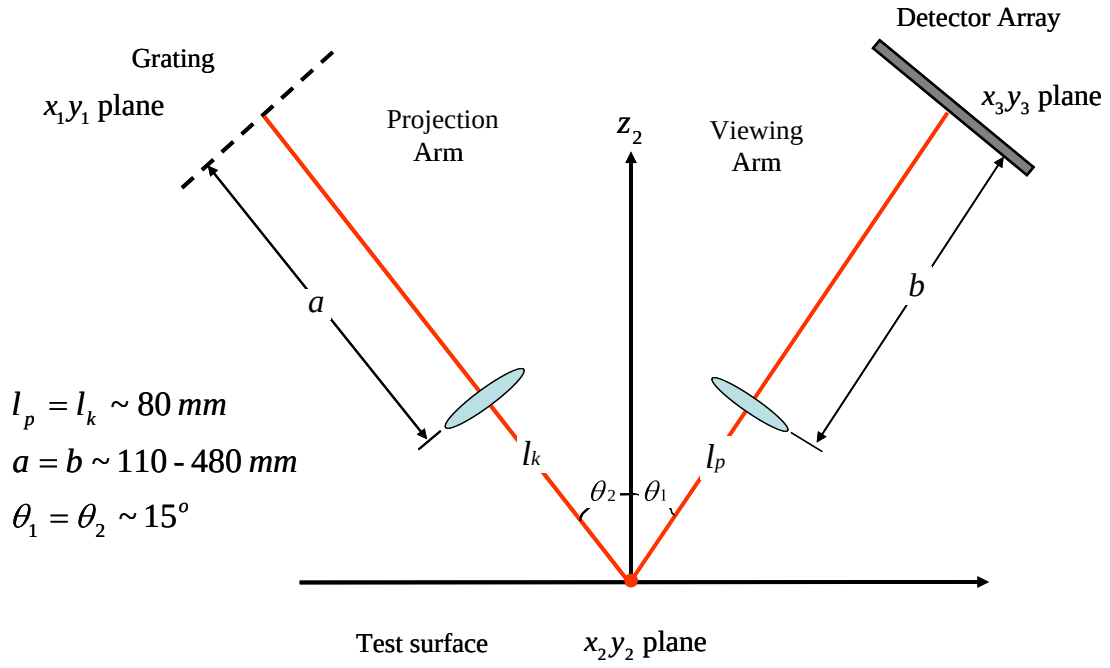

Figure 4-4. Simplified model of the fringe projecting system. All parameters are approximated.

This map consists of a tilted curved plane. The tilt is given by the term $\frac{2\pi}{p_1}x_1$ and is inversely proportional to the projected fringe period. The curvature is given by the term $-\frac{2x_1^{\,2}\tan\theta}{ap_1}$ and is the result of the perspective effect. Removing the tilt will result in a curved surface like the one shown in Figure 2-14 in Chapter 2.

In order to correct for the perspective bias, we must project a grating with variable period, $p_2(x_1)$, that will produce a final fringe intensity distribution corresponding to a flat surface, therefore

$$I = A + B\cos\left(\frac{2\pi}{p_2(x_1)}\left[1-\frac{2x_1\tan\theta}{a}\right]x_1\right) = A + B\cos\left(\frac{2\pi}{p_1}x_1\right), \quad (4\text{-}3)$$

and consequently, $p_2(x_1)$ is given by

$$p_2(x_1) = p_1 \times \left(1-\frac{2x_1\tan\theta}{a}\right). \quad (4\text{-}4)$$

So, in order to correct for the perspective bias, we should project the following fringe intensity map:

$$I_{projected} = 1+\cos\left(\frac{2\pi}{p_2(x_1)}x_1\right) = 1+\cos\left(\frac{2\pi}{p_1\times\left(1-\frac{2x_1\tan\theta}{a}\right)}x_1\right). \quad (4\text{-}5)$$

The phase of Equation 4-5 is given by:

$$\phi_2 = \frac{2\pi}{p_1\times\left(1-\frac{2x_1\tan\theta}{a}\right)}x_1$$

$$= \frac{2\pi}{p_1}x_1 \times \frac{1}{\left(1-\frac{2x_1\tan\theta}{a}\right)}. \quad (4\text{-}6)$$

Since $x_1\tan\theta << a$, Equation 4-6 can be replaced by its first order Taylor series expansion without adding significant errors to the measurements:

$$\phi_2 \sim \frac{2\pi}{p_1}x_1\left(1+\frac{2x_1\tan\theta}{a}\right)$$

$$= \frac{2\pi}{p_1}x_1 + \frac{2x_1^{\,2}\tan\theta}{ap_1}. \quad (4\text{-}7)$$

Equation 4-7 shows that the phase of the new projected grating consists of a tilted plane with additional curvature. Comparing this with Equation 4-2 we find that ϕ_2 has the same tilt as ϕ_1, and the same curvature value with a negative sign. Consequently, the new projected phase map, ϕ_2, can be determined from the measured phase map ϕ_1 by subtracting the tilt from ϕ_1, multiplying the result by -1, and then adding the tilt back. This allows us to correct for the system biases in real time without the need for measuring the system parameters precisely.

Now, consider the case where the test surface is not flat and has a surface height profile given by *H(x,y).* As discussed in Chapter 2, projecting sinusoidal straight fringes with period p_1 on such a surface will produce a fringe intensity distribution on the camera plane given by

$$I = A + B\cos\left(\frac{2\pi}{p_1}\left[1-\frac{2x_1\tan\theta}{a}\right]\times\left[x_1+\frac{2\sin\theta}{M}H\right]\right). \tag{4-8}$$

Projecting a grating with the phase profile measured in the previous step, ϕ_2, will automatically correct for the systematic biases and will produce a fringe intensity distribution on the camera plane given by

$$I = A + B\cos\left(\frac{2\pi}{p_1}\times\left[x_1+\frac{2\sin\theta}{M}H\right]\right). \tag{4-9}$$

The phase of this equation, ϕ_3, is given by

$$\phi_3 = \frac{2\pi}{p_1} \times \left[x_1 + \frac{2\sin\theta}{M} H \right]$$

$$= \frac{2\pi}{p_1} x_1 + \frac{4\pi \sin\theta}{p_1 M} H . \quad (4\text{-}10)$$

Removing the tilt from Equation 4-10 gives

$$\phi_3 = \frac{4\pi \sin\theta}{p_1 M} H . \quad (4\text{-}11)$$

Finally, the height profile can be measured by multiplying the phase by the equivalent wavelength

$$H = \lambda_{eq} \phi_3 , \quad (4\text{-}12)$$

where

$$\lambda_{eq} = \frac{p_1 M}{4\pi \sin\theta} .$$

The equivalent wavelength is determined by calibrating the system using a standard VLSI step height.

1.11.2 Waviness filtering and surface finish measurement

Consider an object like the one described in Chapter 3. The surface consists of a low frequency large form given by h_1 and a high frequency surface finish given by h_2. The overall height profile of the surface is given by

$$H = h_1 + h_2 . \quad (4\text{-}13)$$

In order to measure h_1 only, we need to project pre-deformed fringes that have the same form of the fringes used in Section 4.3.1 to correct for the systematic biases. The fringe frequency is chosen to be very low, but sufficient to measure the low frequency profile without ambiguities. At this frequency, the measurement is insensitive to the surface finish.

The waviness filtering procedure must now be carried out. As illustrated in Chapter 3, straight non-deformed sinusoidal fringes with a large period (p_1) are first projected, so the system will be sensitive only to the large profile. Projecting such a period will produce a fringe intensity distribution on the camera plane given by

$$I = A + B\cos\left(\frac{2\pi}{p_1}\left[1-\frac{2x_1\tan\theta}{a}\right]\times\left[x_1+\frac{2\sin\theta}{M}h_1\right]\right), \tag{4-14}$$

Where the measured phase is given by

$$\phi_1 = \frac{2\pi}{p_1}\left[1-\frac{2x_1\tan\theta}{a}\right]\times\left[x_1+Kh_1\right]$$

$$= \frac{2\pi}{p_1}\left[x_1-\frac{2x_1^2\tan\theta}{a}+Kh_1-\frac{2x_1Kh_1\tan\theta}{a}\right], \tag{4-15}$$

where

$$K = \frac{2\sin\theta}{M}.$$

The last term of the right hand side of Equation 4-15 is small compared to the other terms of the equation. For instance, using the parameter values shown in Figure 4-4, maximum

magnification and object height in the range of 0.1 mm, which is typical for our application, this term is approximately 700 times less than the term Kh_1. Consequently, it can be ignored without adding significant error. Equation 4-15 becomes

$$\phi_1 = \frac{2\pi}{p_1}\left[x_1 - \frac{2x_1^2 \tan\theta}{a} + Kh_1 \right]. \tag{4-16}$$

Notice that the perspective error is not corrected since we projected straight fringes. The first term of Equation 4-16 represents a tilted plane, the second term represents the curvature due to the perspective effect, and the third term is the low frequency height profile multiplied by a constant *K*.

Fringes with a variable period ($p_3(x_1)$) must now be projected, in order to filter out the low frequency profile h_1. This gives a fringe intensity distribution on the camera equivalent to the distribution corresponding to a flat surface. Therefore,

$$I = A + B\cos\left(\frac{2\pi}{p_3(x_1)}\left[1 - \frac{2x_1 \tan\theta}{a}\right] \times \left[x_1 + Kh_1\right] \right) = A + B\cos\left(\frac{2\pi}{p_1} x_1 \right), \tag{4-17}$$

which leads to

$$\frac{1}{p_3(x_1)} = \frac{x_1}{p_1\left[1 - \frac{2x_1 \tan\theta}{a}\right] \times \left[x_1 + Kh_1\right]}. \tag{4-18}$$

So, in order to filter out the low frequency profile, we should project the fringe intensity distribution given by

$$I_{projected} = 1 + \cos\left(\frac{2\pi}{p_3(x_1)} x_1\right)$$

$$= 1 + \cos\left(\frac{2\pi x_1^{\,2}}{p_1\left[1 - \frac{2x_1 \tan\theta}{a}\right] \times \left[x_1 + Kh_1\right]}\right). \qquad (4\text{-}19)$$

The phase of Equation 4-19 can be written as

$$\phi_3 = \frac{2\pi x_1^{\,2}}{p_1\left[1 - \frac{2x_1 \tan\theta}{a}\right] \times \left[x_1 + Kh_1\right]}$$

$$= \frac{2\pi x_1}{p_1} \times \frac{1}{\left[1 - \frac{2x_1 \tan\theta}{a}\right]} \times \frac{1}{\left[1 + \frac{Kh_1}{x_1}\right]}\ , \qquad (4\text{-}20)$$

and since the term $2x_1 \tan\theta << a$, and the term $Kh_1 << x_1$, (the object height is much smaller than the field of view), the Taylor series expansion of Equation 4-20 can be written as

$$\phi_3 \sim \frac{2\pi x_1}{p_1} \times \left[1 + \frac{2x_1 \tan\theta}{a}\right] \times \left[1 - \frac{Kh_1}{x_1}\right]$$

$$= \frac{2\pi}{p_1} \times \left[1 + \frac{2x_1 \tan\theta}{a}\right] \times \left[x_1 - Kh_1\right]$$

$$= \frac{2\pi}{p_1}\left[x_1 + \frac{2x_1^2 \tan\theta}{a} - Kh_1 - \frac{2x_1 Kh_1 \tan\theta}{a}\right]. \qquad (4\text{-}21)$$

Again, the last term of the right hand side of Equation 4-21 can be ignored giving

$$\phi_3 \sim \frac{2\pi}{p_1}\left[x_1 + \frac{2x_1^2 \tan\theta}{a} - Kh_1 \right] \tag{4-22}$$

Comparing Equation 4-22 to Equation 5-16 we find that the two phase maps have the same tilt represented by the term x_1, and the second and third terms have the same magnitude with an opposite sign. Consequently, the phase ϕ_3 that is needed to filter out the low frequency profile can be extracted from the measured phase ϕ_1 by subtracting the tilt from ϕ_1, multiplying the result by -1, and then add the tilt back. Therefore, projecting a sinusoidal fringe profile with a phase profile given by ϕ_3 on the test object produces a straight sinusoidal fringe profile on the camera that leads to a flat surface once analyzed.

To measure surface finish without the impact of the large profile, we need to project fringes with a phase profile similar to ϕ_3 with much higher frequency. This can be done by multiplying ϕ_3 by a factor representing the ratio between the high and low frequencies. For example, if we need to project fringes with 10 times the frequency of ϕ_3, the new phase should be $10\phi_3$.

1.12 Experimental procedures and results

1.12.1 Determining the bias correction phase profile

A Mitutoyo ceramic gage block, with surface flatness of 1 μ inch, was used as a flat surface reference.

A straight sinusoidal fringe profile was created in Matlab™ using the equation $I = 1 + \cos\frac{2\pi}{p_1}$, where $p_1 \sim 0.5\ mm$ is the fringe period on the LCD panel plane. The fringes were displayed on the screen and consequently projected on the flat surface with the system adjusted to its lowest magnification where the field of view is around 5.3×4.1 mm^2. An image of the fringes impacted by the surface was then captured and saved. This procedure was repeated eight times, shifting the phase of the lines by π/2 each time, to get a total of eight phase-shifted frames, as shown in Figure 4-5. The function '*mat2vision_8*' was then used to convert the frames to Vision™ format, and then analyzed using an 8-step phase shifting algorithm to create the surface OPD map. Figure 4-6 shows the flat surface OPD map before removing the tilt, and Figure 4-7 shows the same map after the tilt was removed. The curvature of the OPD map shown in this figure is a direct result of the perspective bias of the system. The figure also shows a linear, periodic high-frequency artifact added to the OPD map. These grove-like features are caused by the high frequency components of the non sinusoidal shape of the fringes resulted by the camera nonlinear intensity response.

The flat measured so far, and shown in Figure 4-7, represents the system biases in addition to noise (mainly camera noise), and potential flatness variations on the surface. In order to better estimate the system biases, the previous procedure was repeated fifty times. A small phase shift (2π/50) was added to the generated gratings every time in order to average out the non-sinusoidal fringe bleed through, and different randomly-selected

regions of the gage block were measured every time to average out surface flatness errors. Finally, the average of the fifty measurements was taken and the tilt removed by subtracting the best fit plane from the OPD map. The resultant was multiplied by -1 and the tilt was added back by adding the best fit plane. This map was saved as the system biases OPD map. This map, after multiplying by 2π to obtain the phase map, is used to generate all of the pre-deformed gratings needed to overcome the systematic biases (mainly the perspective bias). The system bias non-tilted OPD map is shown in Figure 4-8.

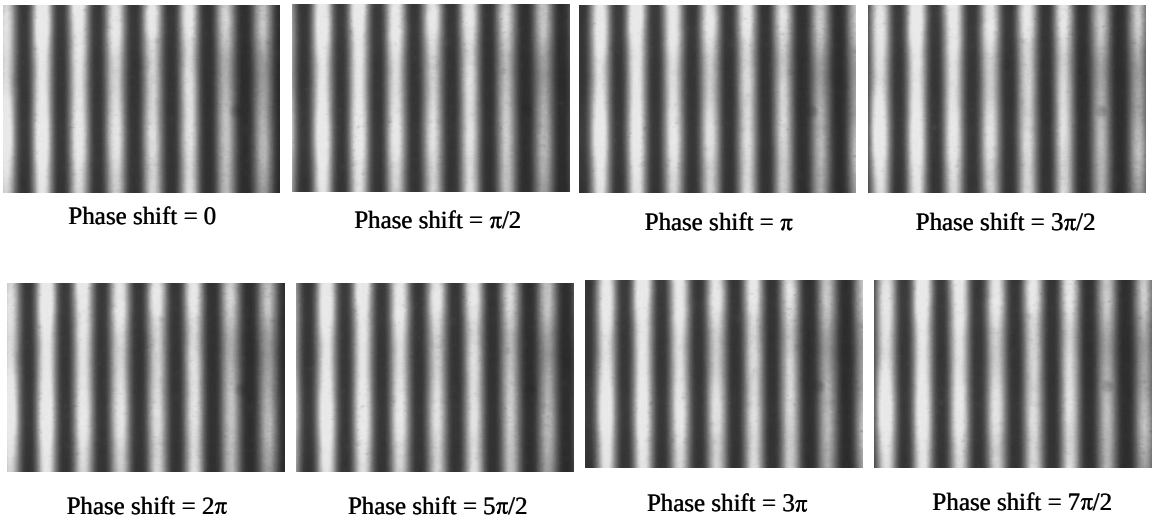

Figure 4-5. Eight phase-shifted frames showing the fringes after being projected on the flat surface.

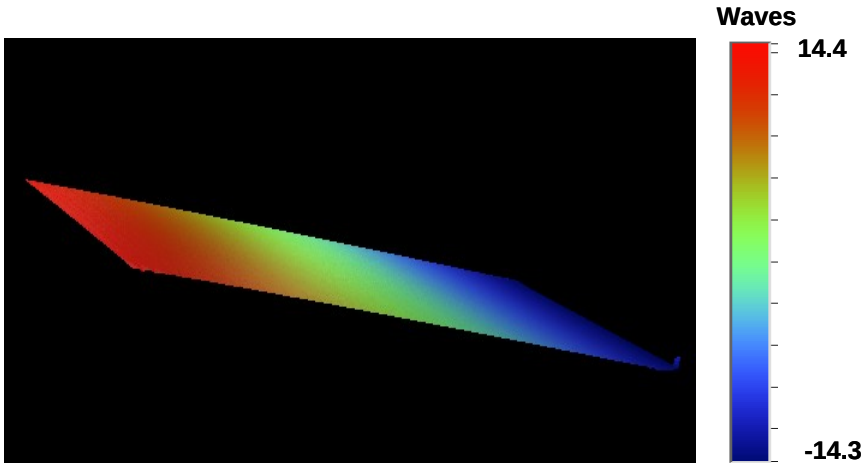

Figure 4-6. The flat surface OPD map before removing the tilt.

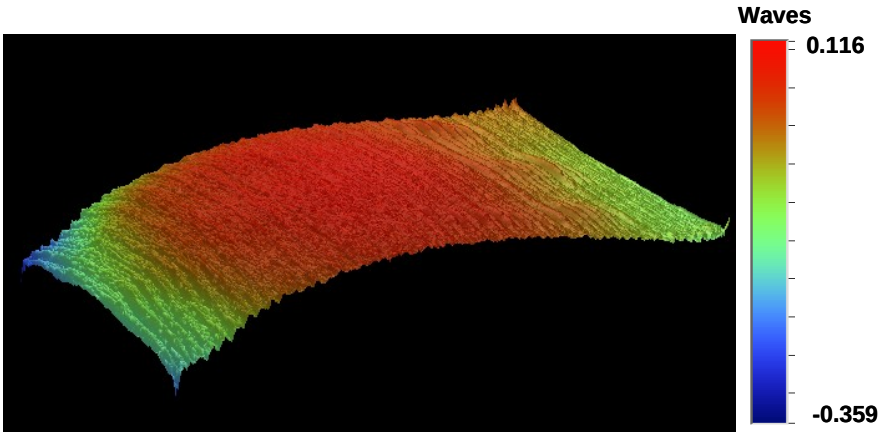

Figure 4-7. The flat surface OPD map after removing the tilt. The grove like high frequency artifact is the fringe bleed through resulted from the high frequency components in the fringe profile.

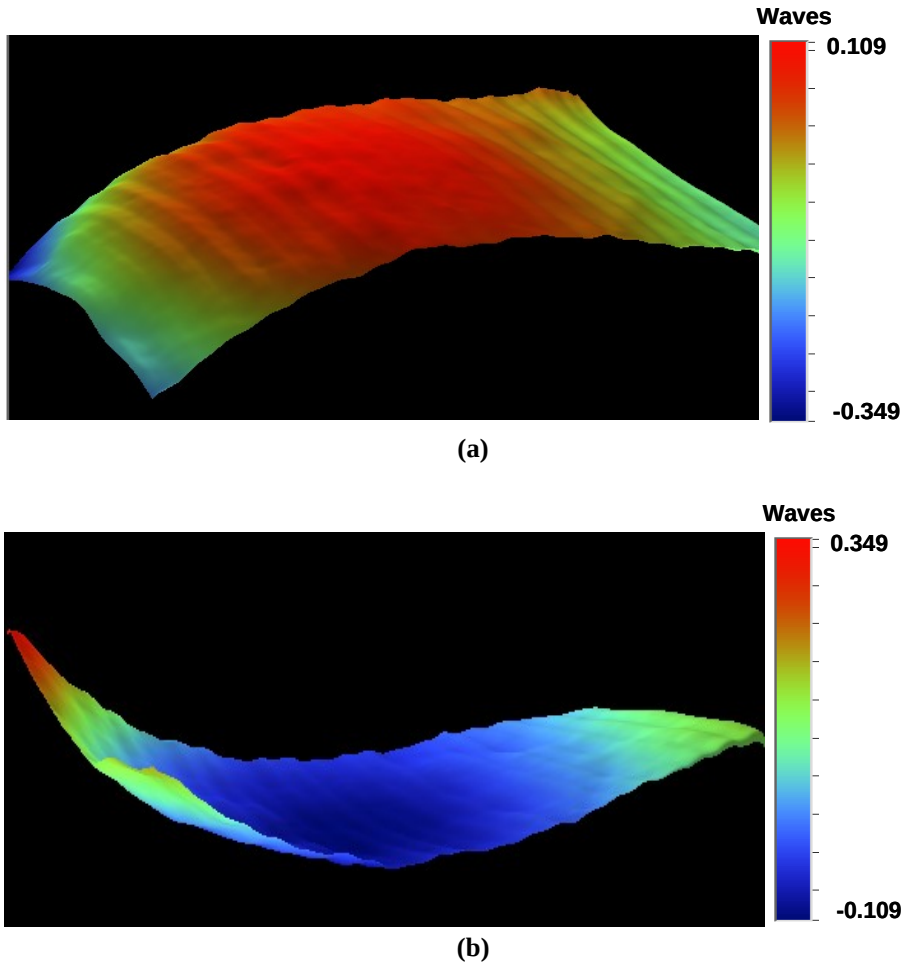

Figure 4-8. The system biases OPD map (a) before inverting and (b) after inverting.

1.12.2 System vertical calibration (measuring λ_{eq})

The next step was to calibrate the system for the height measurements. The goal is to find the effective wavelength to be used to convert all the measured OPD maps (in waves) into real height values. A 23.23 µm VLSI standard step height was used for this purpose. The surface of the step height is highly reflective, so external neutral density filters were added to reduce the intensity.

First, to assess the system bias in our measurements, a straight sinusoidal grating with period ~ 0.5 mm was projected onto the step height surface, and eight phase-shifted frames were captured and sent to Vision for analysis. Figure 4-9 shows the fringes projected on the step height and Figure 4-10 shows the resulting OPD map generated by Vision. The system bias is apparent in this figure as the large bowed background.

In Figure 4-9, the image shows dark areas at the corners of the image, more apparent at the left side. This is due to a process called vignetting that results from a reduced effective aperture stop of the imaging system for the off axis light bundles [108].

Next, the system bias OPD map shown in Figure 4-8 (b) was used, after adding the tilt back, to generate the pre-deformed grating needed to correct for these biases. This grating was then projected onto the VLSI surface and an 8-step phase shifting algorithm used to analyze the interferograms. Figure 4-11 shows the generated OPD map. The figure shows that the system bias is minimized. The bias correction is not complete at the top left corner, and this is due to the vignetting effect mentioned above. The vignetting has the effect of reducing the intensity and hence reducing the fringe contrast. This should not affect the phase as long as the intensity level is well above the noise level, but when the contrast is so poor the noise effect will be significant and this translates to an error in the phase map which is obvious in this case.

In order to correctly measure the step height, a mask was applied to the data to exclude the two sides and keep the middle region only. The multi region analysis function in Vision was used to calculate the average step height value and the standard

deviation. Figure 4-12 shows the results. The column labeled “mean” represents the mean height of the different regions, and the column labeled “Ra” represents the mean roughness for each region. The regions are labeled and shown in the step height view to the left side of the table. In this table, the values are expressed in nanometers instead of waves, but the data were initially normalized so that every nanometer equals one wave. The mean roughness, Ra, is mainly a result of the fringe bleed through, and was taken as the error in estimating the step height value.

From these results, the step height value was calculated to be 0.044 ± 0.0015 waves. Finally, the equivalent wavelength was calculated by dividing the nominal step height value, in micrometers, by the measured value in waves: $\lambda_{eq} = 527.0 \pm 11.8\ \mu$m/wave

.

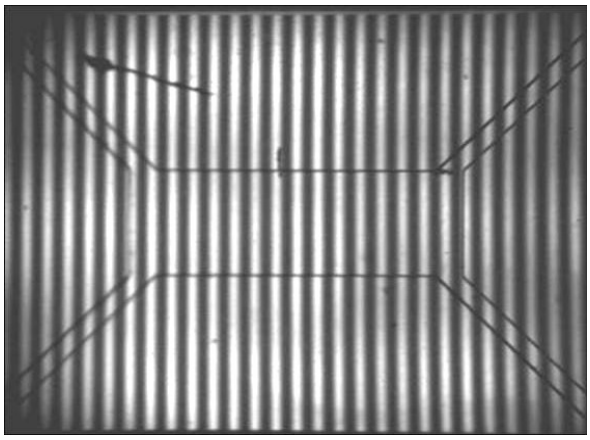

Figure 4-9. Fringes projected on the VLSI step height surface. The vignetting effect is apparent on the upper and lower left corners.

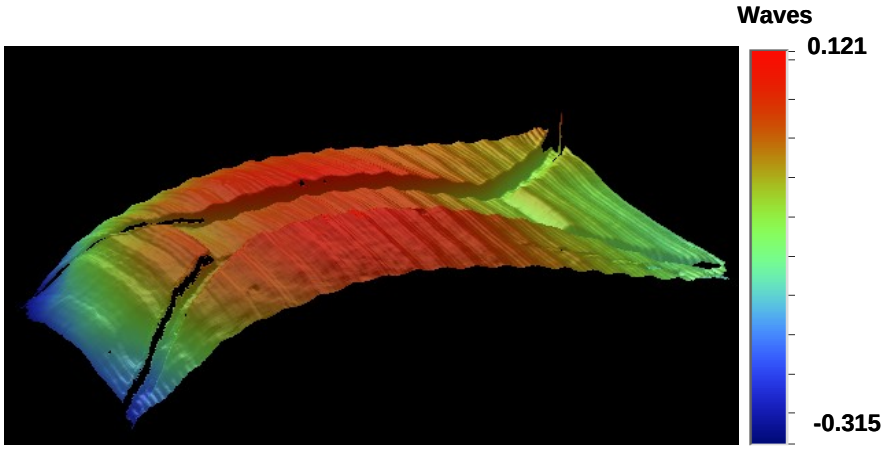

Figure 4-10. The OPD map of the VLSI step height resulted from projecting straight fringes. The effect of the system biases is very clear.

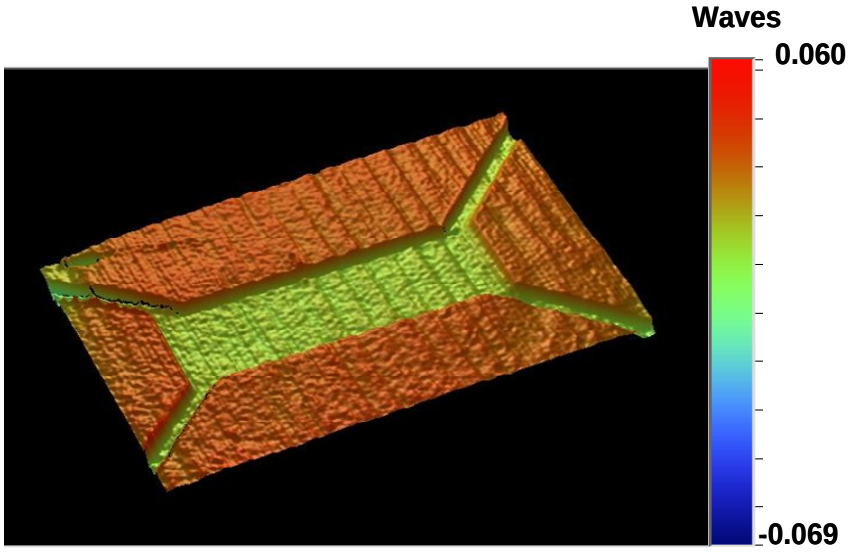

Figure 4-11. The VLSI step height OPD map generated by projecting the pre-deformed grating to correct for the system biases.

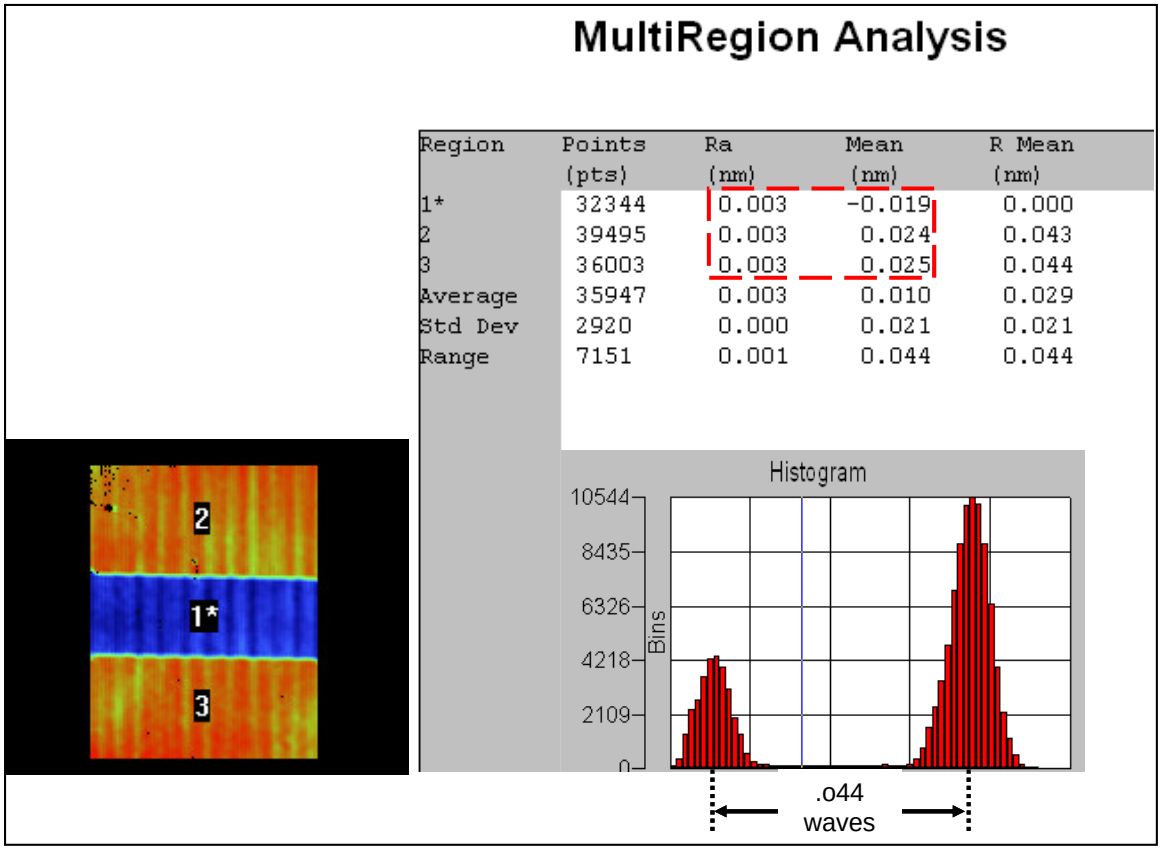

Figure 4-12. Multi-region analysis results for the step height measurement.

1.12.3 Lateral calibration

An Edmund 10mm cross line scale was used for lateral calibration. The scale is numbered every 1 mm, and graduated every 0.1 mm.

First, the scale was placed horizontally to calibrate the x-axis. A set of 8-frames were captured and sent to Vision. The calibration factor in Vision was set to 1, so every micron represents one pixel. The resulting OPD map was high pass filtered to distinguish the lines labeling the scale. The 2-D analysis option in Vision was used to estimate the

distance between the scale lines. The results are shown in Figure 4-13, showing that 5 mm on the scale is represented by 596 ± 2 pixels. The 2 pixel uncertainty includes the uncertainty in placing the cursor over the label on the scale, one pixel from the left and one from the right. Consequently, the x-calibration factor was calculated by dividing the scale nominal value by the number of pixels, which gives a factor of 8.39 ± 0.03 μm/pixel.

The same procedure was followed to calibrate the y-axis, but this time the scale was placed vertically. The results are captured in Figure 4-14, which shows a 3 mm patch on the scale was represented by 326 ± 2 pixels, which makes the calibration factor for the y-axis = 9.21 ± 0.06 μm/pixel.

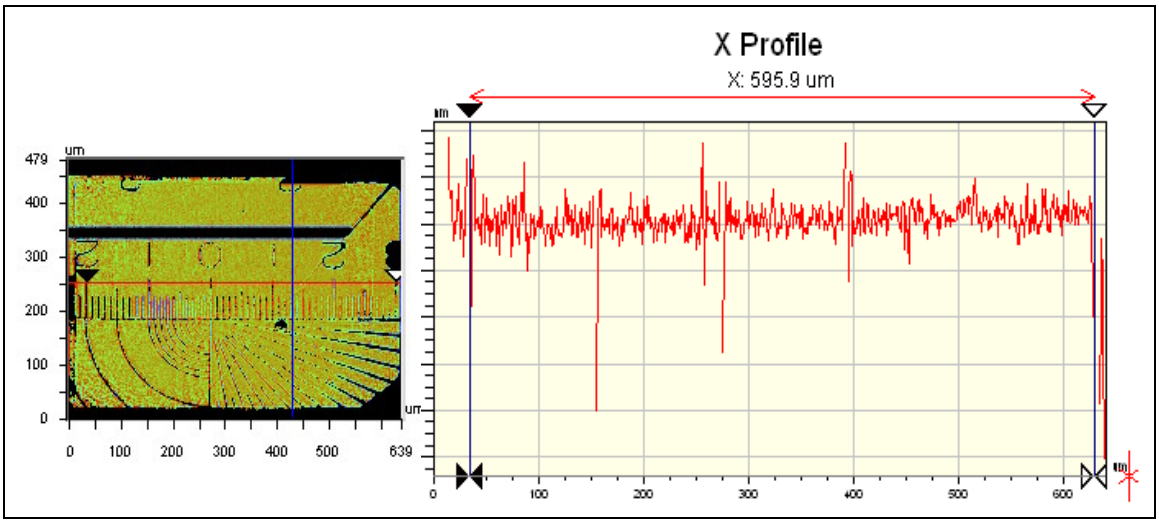

Figure 4-13. X-axis calibration through VisionTM. To the left is the top view of the scale, and to the right is a line trace at the location indicated by the blue line, showing the peaks representing two scale lines. A pixel represents one micron in the plot.

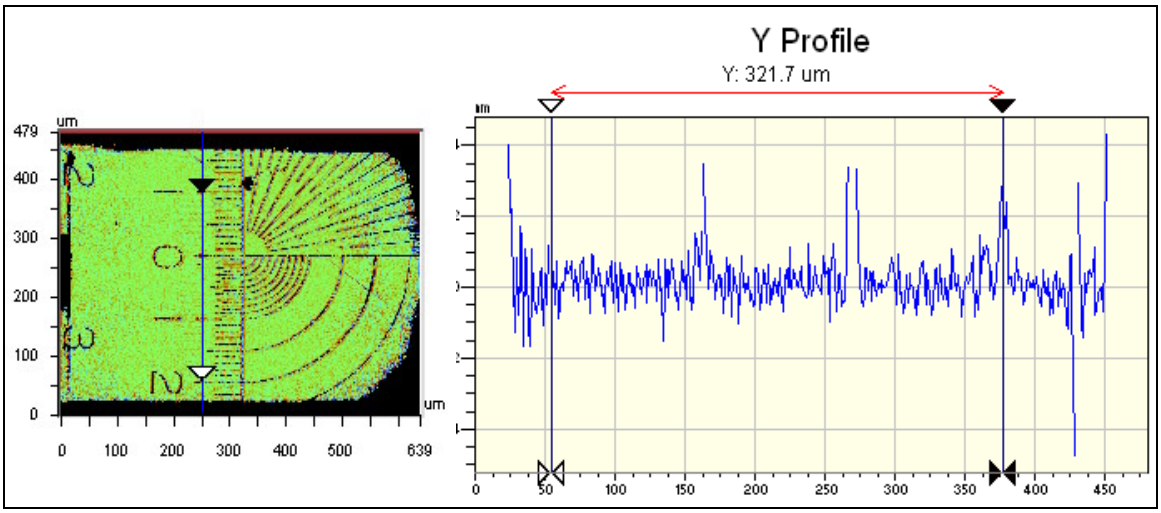

Figure 4-14. Y-axis calibration using Vision™. To the left is the top view of the scale and to the right is a line trace through the image on the left at the vertical blue line. The two markers indicate the location of two scale lines. A pixel corresponds to a micron in the plot.

1.12.4 Filtering the large surface form

To demonstrate the dynamic range measurement method, we fabricated a surface that had surface topography with two distinct spatial frequencies. We used a dental replica to replicate the roughness of a piece of sand paper. The dental replica remains flexible after replication and can then be deformed to generate an additional low frequency shape. Wrapping the replicated sand paper surface around a small post provided the low-frequency form in this case. We spray painted the surface white to maximize fringe contrast. The resulting surface is shown in Figure 4-15.

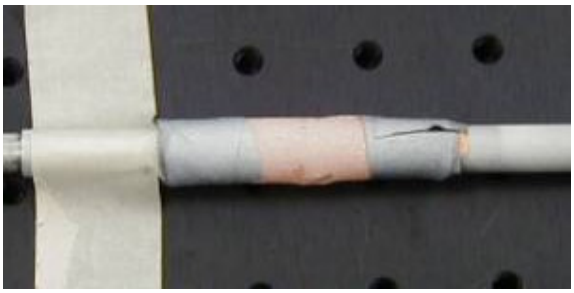

Figure 4-15. Test object. The light-orange area in the middle is the dental replica of the sand paper, wrapped around a post and sprayed with white paint.

The first step to the measurement was to create the bias-correcting, pre-deformed grating with a period p = 5 mm. This grating was the same system-bias tilted OPD map used to create the fringes to measure the step height in Section 5.4.2, but multiplied by a factor of 0.1 to decrease the fringe frequency (increase the effective wavelength) 10 times. This frequency was chosen to minimize the system sensitivity so the large surface form was easily measured which reduced the sensitivity to the small surface finish. At this wavelength though, the system did not have enough sensitivity to measure the 23.23 μm VLSI step height standard. This was the largest calibrated step height available, consequently the system effective wavelength could not be calibrated at this frequency. The equivalent wavelength was taken to be approximately 10 times larger than that determined in the system vertical calibration procedure described in Section 5.4.2. This is a good approximation assuming that the system biases are well corrected. Consequently, the system equivalent wavelength at this frequency was estimated to be 5.27 ± 0.12 μm/wave.

The grating was then displayed on the screen and projected on the surface, 8 phase-shifted frames were captured and analyzed. Figure 4-16-(a) shows the grating, and

Figure 4-16-(b) shows the fringes after being projected on the surface. Figure 4-17-(a) shows the resulting surface OPD map without removing the tilt, and Figure 4-17-(b) shows the height profile after removing the tilt, multiplying by the equivalent wavelength and applying a low pass filter for noise reduction. The figure shows that the system is able to measure the surface profile while filtering out the surface finish. The cut off frequency of the low pass filter used here was chosen so that most of the high spatial frequency features on the surface are filtered out and the only remaining spatial frequency is the surface large profile since this is the profile we intended to measure at this step.

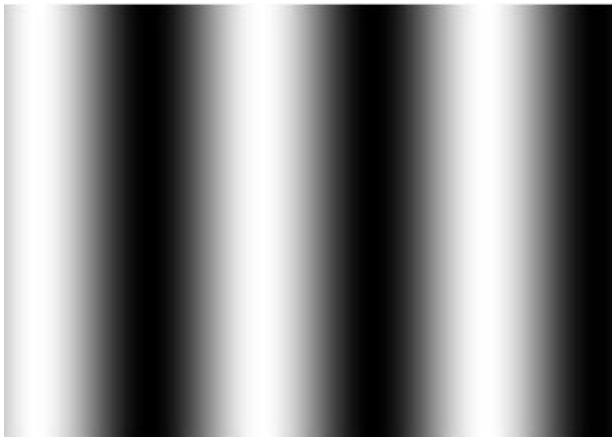

(a)

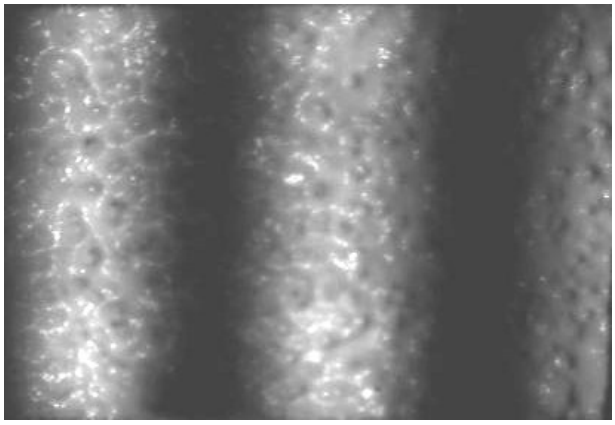

(b)

Figure 4-16. (a) The 5 mm period grating used for measuring the surface form. (b) The fringes after being projected on the surface.

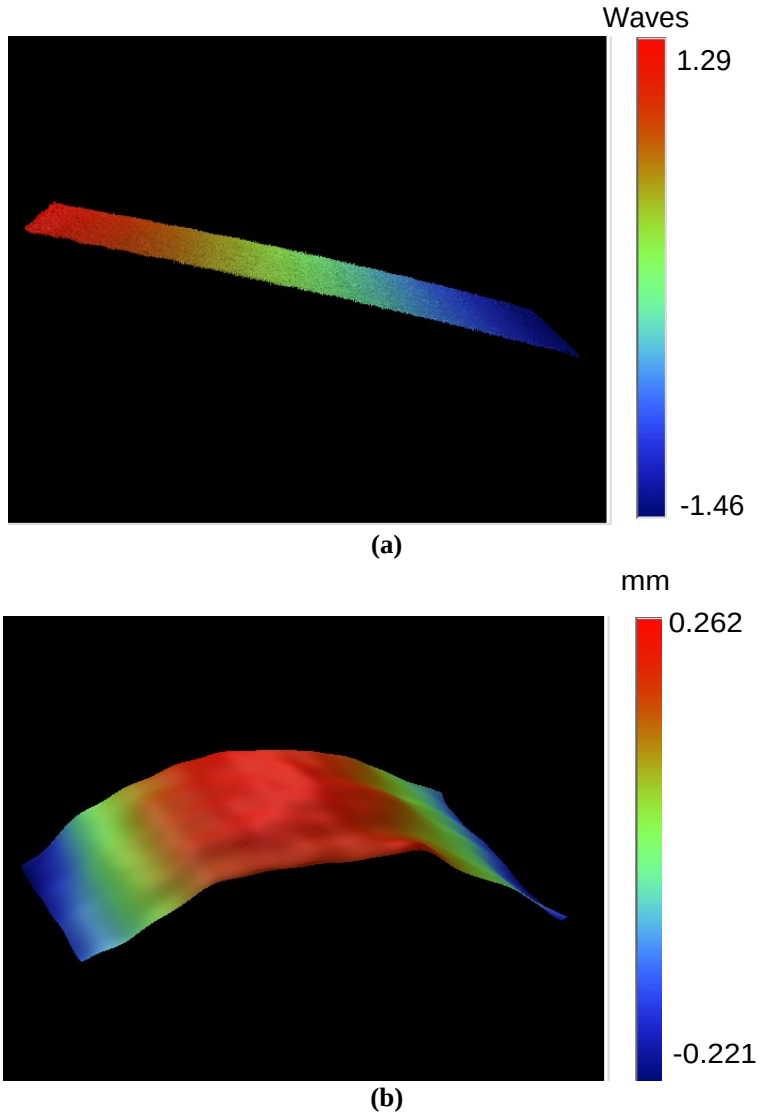

Figure 4-17. (a) The measured surface form OPD map without removing the tilt. (b) The low frequency form of the object found by removing the tilt in (a) and multiplied by the equivalent wavelength.

Figure 4-17-(a) was then used to optically filter out the surface low-frequency form (waviness) to measure the surface finish.

First, the tilt was removed by finding the best fit plane and subtracted it from the OPD map, then the map was multiplied by -1 to invert the profile. This was then added to the bias-correction OPD profile shown in Figure 4-8-(b) to create an OPD profile capable of correcting the system biases and filtering out the waviness simultaneously. Finally, the tilt was added back by adding the best fit plane found earlier.

The OPD map created so far can be used to create a grating with period of 5 mm. Using this grating will correct for the system biases and filter out the surface large form, but the system will not have sufficient sensitivity to measure the small features. To reduce the period of this grating (increase the frequency), this OPD map was multiplied by 10 to increase the fringe frequency 10 times, making the system equivalent wavelength 527 μm again. This wavelength is necessary to make the system sensitive enough to measure the small features on the surface.

The final OPD map was used to create the grating needed to filter out the waviness and measure the surface finish. Figure 4-18 shows the image of the grating projected onto the surface.

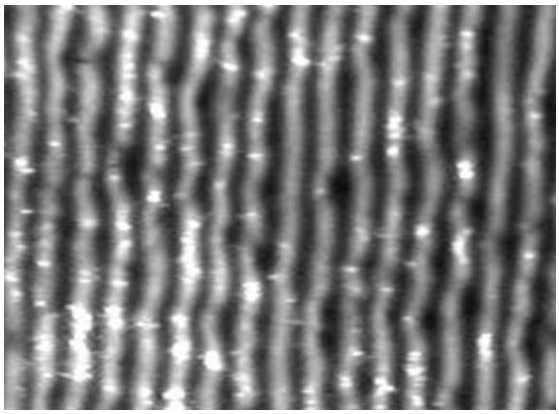

Figure 4-18. The 0.5 mm fringes projected on the surface. The fringes are deformed by the small features on the surface.

As before, 8-phase shifted frames were captured and then analyzed to create the surface finish OPD map. The tilt was removed and the phase map then multiplied by the equivalent wavelength to generate the surface finish height map shown in Figure 4-19-(a) and (b). The figure clearly shows that the surface large form was successfully filtered out and the surface finish was measured without the impact of the form. The lateral calibration factors discussed in Section 5.4.3 were used to define the lateral dimensions shown in Figure 4-19-(b).

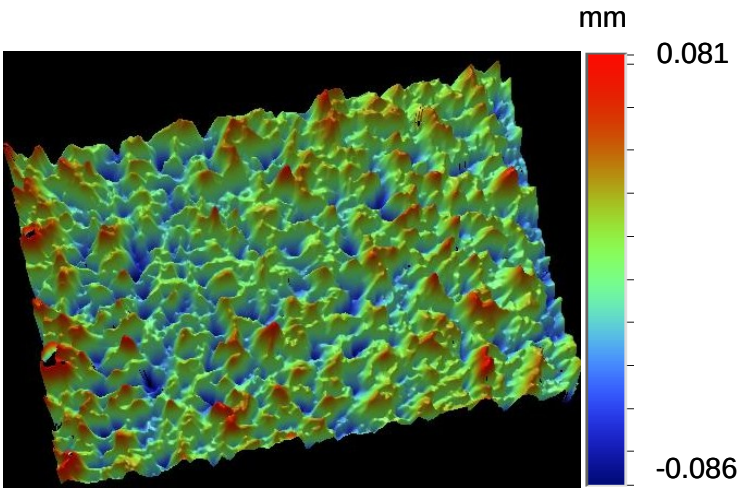

(a)

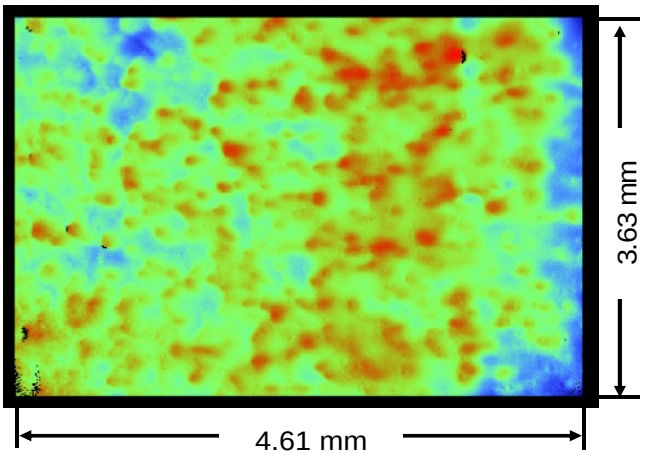

(b)

Figure 4-19. The surface finish measured without the impact of the surface low-frequency form. (a) The 3-D profile. (b) Top view with lateral dimensions.

Looking at Figure 4-19 we can see a small amount of waviness from left to right, this is believed to be a real surface waviness component that could not be detected using the

large equivalent wavelength since it has a very small value. But when using the small equivalent wavelength grating the system had sufficient resolution to detect it.

Finally, the overall object height profile was created by adding the form shown in Figure 4-17-(b) and the surface finish shown in Figure 4-19. The final surface height profile is shown in Figure 4-20.

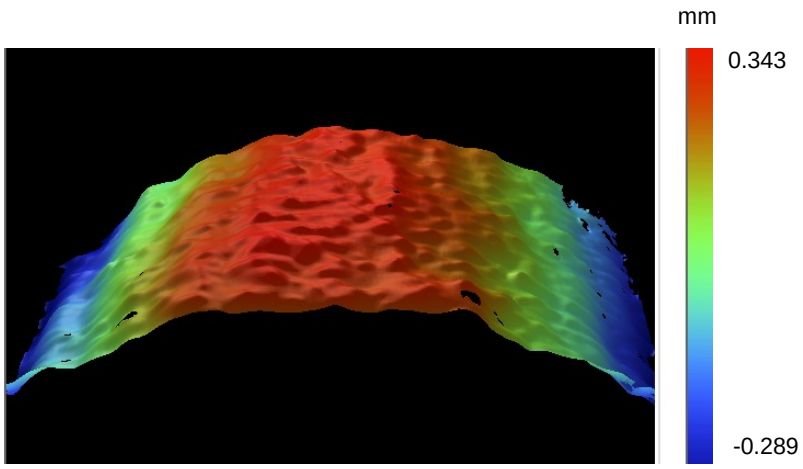

Figure 4-20. The final surface height profile created by adding the surface form shown in Figure 4-17 and the surface finish shown in Figure 4-19.

1.12.5 Other measurements

In the course of developing this system, several objects with different sizes and shapes were measured. The following example is a measurement of the head of the falcon that appears at the back of a quarter. The coin was sprayed white and a 0.5 mm fringe period was used. Figure 4-21 shows the fringes projected on the surface, and Figure 4-22 shows the surface height profile.

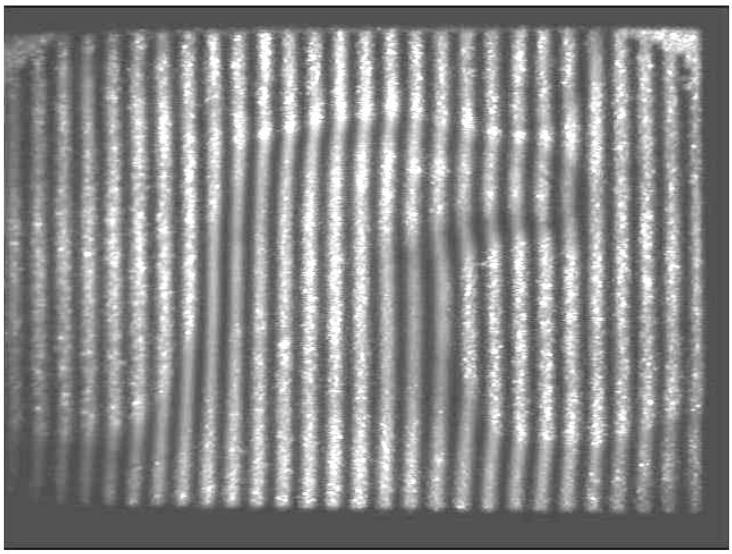

Figure 4-21. The 0.5 mm period fringes projected onto the surface of a quarter.

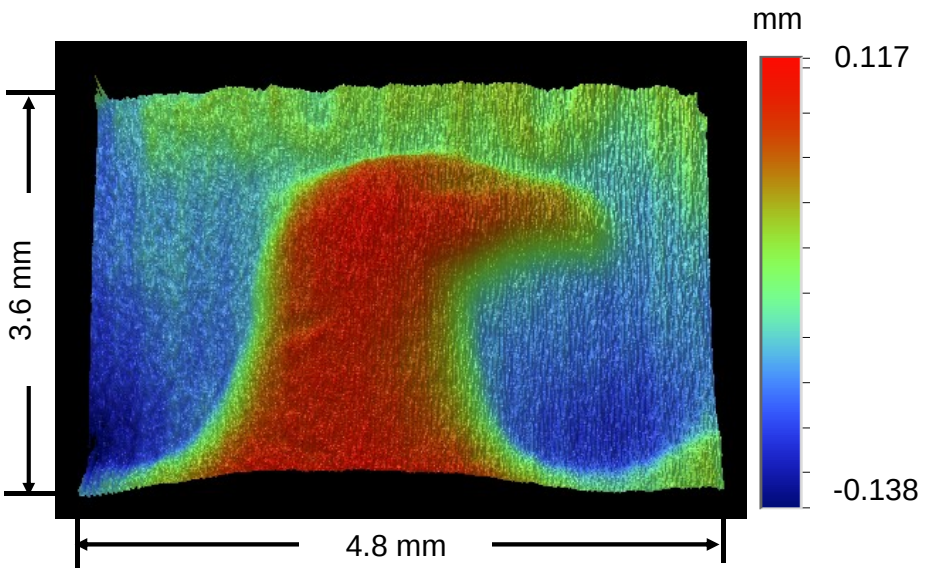

Figure 4-22. The measured height profile.

CHAPTER 5: SOLDER BUMP METROLOGY

1.13 Introduction

Flip chip bonding in advanced integrated circuit packaging requires the deposition of very large arrays of small solder bumps. The bumps are spherical caps with diameters on the order of 80-100 μm and are approximately 25-50 μm high. They are deposited on a substrate covered by a solder resist film to electrically isolate the bumps from each other. Between the solder resist film and the substrate there are additional solder and resist layers to connect the upper part (the bumps) to the pins and then to the board. Thousands of bumps are grouped together into various patterns to serve as high density interconnects between the package and the chip itself (the die). Figure 5-1 shows a substrate package with a solder bump field in the middle. Figure 5-2 is a higher magnification micrograph of a solder bump field and a micrograph of an individual bump taken by a scan electron microscope.

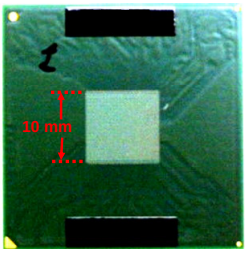

Figure 5-1. Solder bump field on the middle of a substrate package. The bump field is approximately 10 mm^2 and contains ~ 3000 bumps.

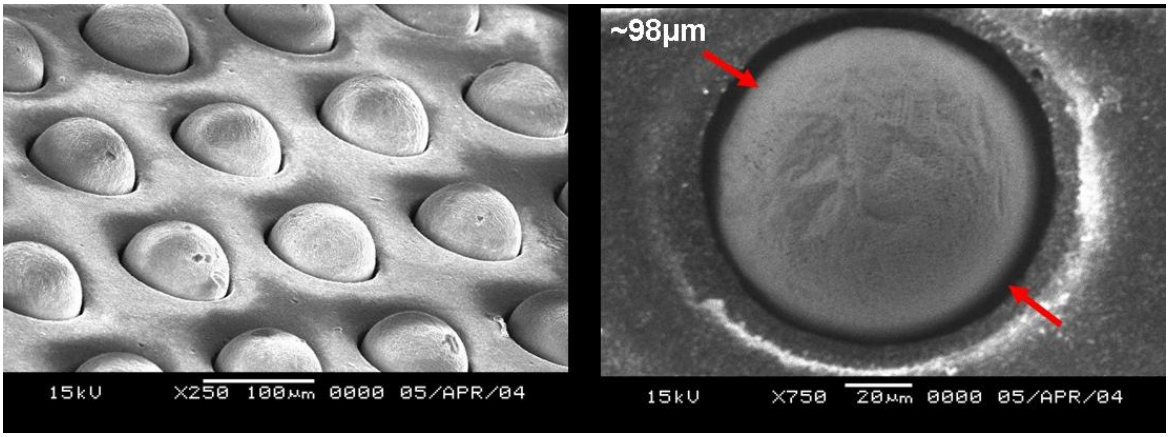

(a) **(b)**

Figure 5-2. SEM images for solder bumps. (a) A bump field magnified 250 times. (b) An individual bump magnified 750 times.

As mentioned in Chapter 1, it is critical to measure the volume of these bumps. It was found that bumps with insufficient solder volume will not be able to connect with the die, causing an open circuit leading to a faulty processor or chipset. On the other hand, bumps with extra solder volume have the tendency to spread during the packaging process short circuiting the neighboring bumps. Therefore, it is critical to measure the volume of these bumps to set a tolerance range for the allowed solder volume used in different chip packaging processes.

To determine the true shape of the solder bumps above the substrate, research was conducted during an internship at Intel's assembly material characterization lab summer 2004. The results showed that the solder portion above the substrate is well approximated by a spherical cap. A cross sectional approach was used to collect an enormous number of cross sections for random bumps, cross sectioned to variable depths, in different types of packages from different manufacturers. The cross sections were imaged using a high magnification, high resolution optical microscope, and then a circle fitting algorithm used to fit circles through the 2-D cross sections. Figure 5-3 shows examples of the cross

sections magnified 500 times. The added circle in the images indicates the quality of a spherical cap approximation for the bump shape.

The figures also show that different packages have different amounts of solder with different shapes below the surface. From a measurement perspective, an estimate of the solder volume should include the volume below the surface. On the other hand, from the perspective of process control for the chip attachment the volume below the surface is irrelevant since it is not available for forming the joint. Also, it is almost impossible to measure the hidden solder volume without destroying the part. Consequently, the metrology discussed here focused on measuring the part of solder above the substrate, (the spherical caps).

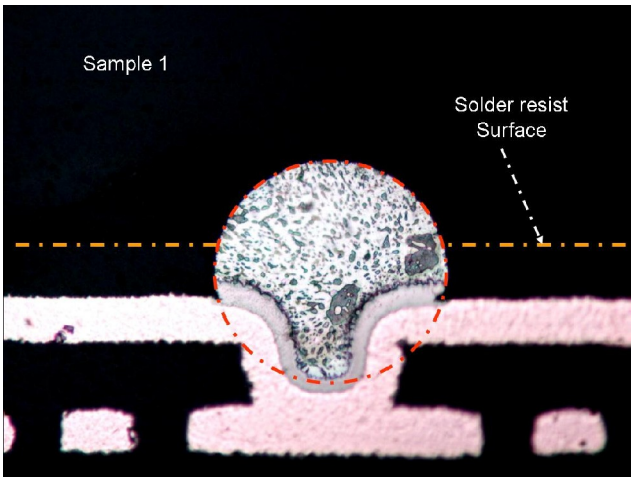

(a)

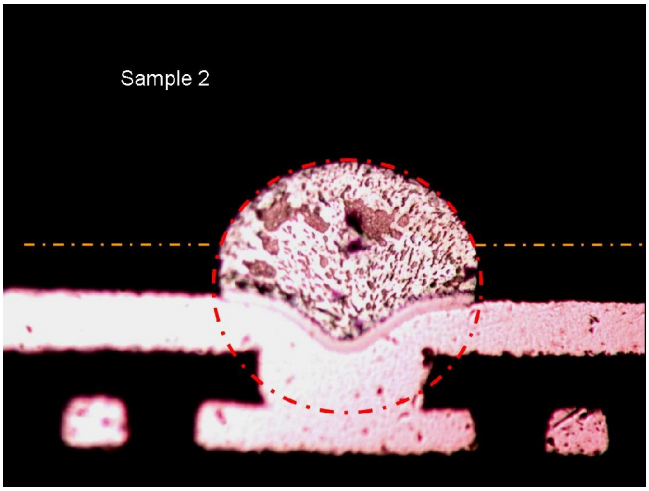

(b)

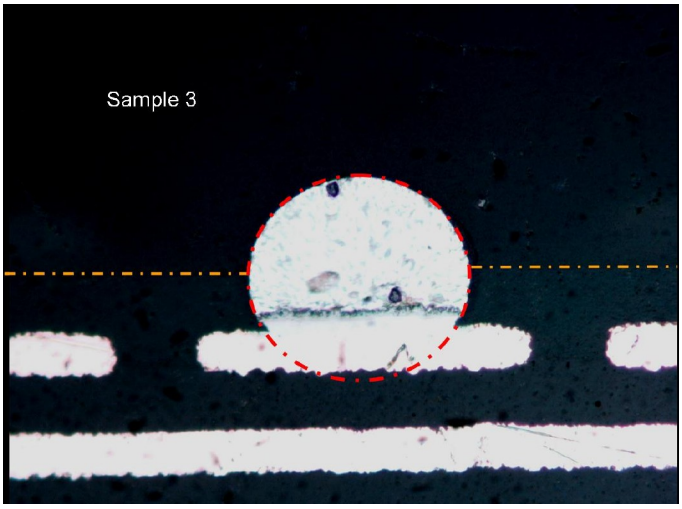

(c)

Figure 5-3. Cross sectional views for different solder bumps. Notice how well the circles fit the bump surfaces.

1.14 Intel's bump metrology tool

As mentioned before, the current measurement tool at Intel used for solder bumps is based on the well-known fringe projection technique to measure bump heights, and it uses a red LED ring placed very close to the part to provide a low angle dark field illumination to measure the bump diameters. (The bumps appear as rings with this illumination). Figure

5-4 shows a schematic of the system. A fringe projector illuminated by a halogen lamp projects a grating (Ronchi ruling) with fixed frequency and projection angle of 60º. A high resolution camera (1300 x 1200 pixels) is placed above the part and perpendicular to the bump field and collects the images. The part is surrounded by a red LED ring for diameter measurements as mentioned above. The system uses a 4 step phase shifting technique for fringe analyses. The phase shifting is achieved by shifting the grating in front of the projector using a step motor. Figure 5-5-(a) shows a bump field with the projected fringes (the type of images used for height measurements), and Figure 5-5-(b) shows a 2-D ring illuminated image (the type of image used to measure diameters).

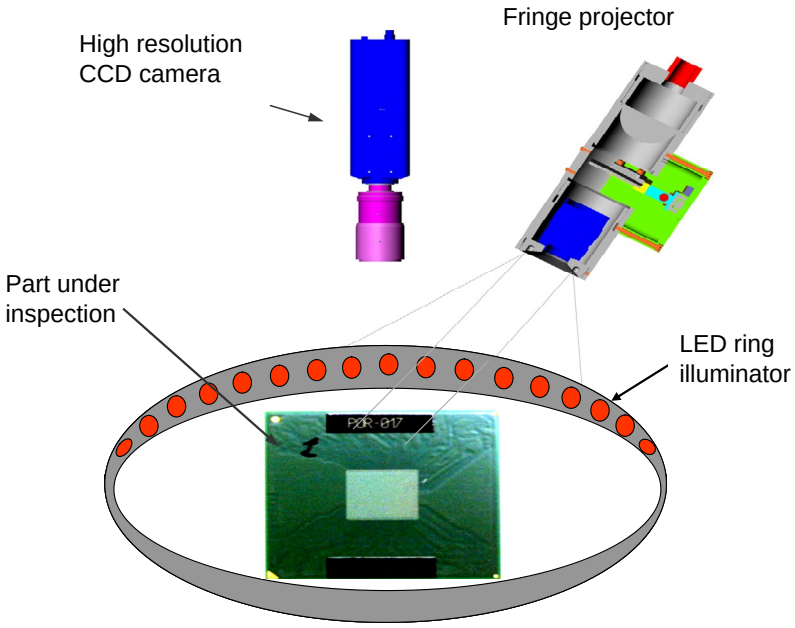

Figure 5-4. Intel's system schematic

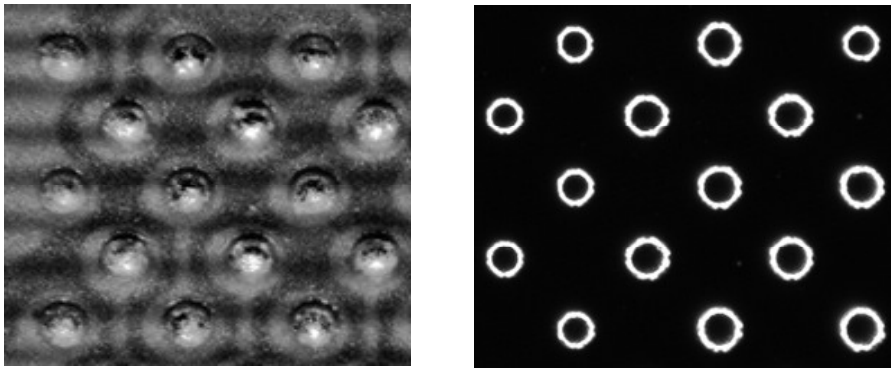

(a) **(b)**

Figure 5-5. (a) A bump field showing the projected fringes used for bump height measurements. (b) A 2-D image of the bump field illuminated using the LED ring light to measure bump diameters.

Two major challenges are faced in measuring solder bumps. The spherical shape of the bumps, with large slopes on the sides, makes light collection from these regions difficult. Because the bumps are relatively smooth, only specular light is reflected from the sides and imaging requires a very large numerical aperture imaging system. Consequently, only a small patch at the top of the bump is captured by the imaging optics. Increasing the NA of the imaging optics will increase the bump area that can be measured, but decreases the field of view and hence the measurement speed.

The other challenge is the high reflectivity of the bump material. Large intensities from the portion of the bump imaged can easily saturate the camera and blur the fringe profile. Decreasing the intensity minimizes this, but decreased intensity decreases the amount of light reflected from the substrate since its reflectivity is much smaller. Both surfaces must be measured to estimate the bump height. Figure 5-6 shows a bump field with the projected fringes as seen by Intel's system. Notice how bright the top of the bumps appear and the low fringe contrast on the substrate. Also notice the small amount of the available data at the top of the bump compared to the total bump size.

Since the system does not provide the constructed phase map of the bump field after analysis, we analyzed the images using a commercial fringe analyses program, IntelliWave™, to obtain the 3-D phase map shown in Figure 5-7. The map shows the constructed bumps having a dip (missing data) at the top caused by the saturated camera pixels at the top. The map also shows large data peaks surrounding the measured portion of the bump that are caused by specular reflections from neighboring bumps. These are the faint ring of spots seen near the bump edge in Figure 5-6. These peaks are usually treated as noise and ignored in the measurement. The system's vendor uses a "classified" algorithm to overcome the above problems.

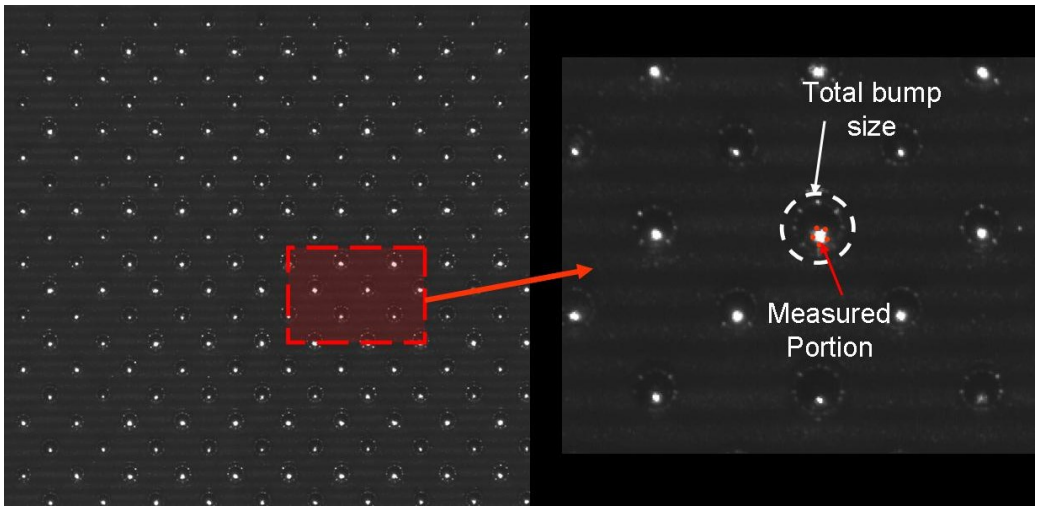

Figure 5-6. A bump field with projected fringes as seen by the Intel's system. Notice the intensity difference between the fringes on the substrate surface and the bump surface. The figure on the right compares the actual size of the bump with the measured portion size. The small light dots surrounding each bump are speckle reflection from surrounding bumps.

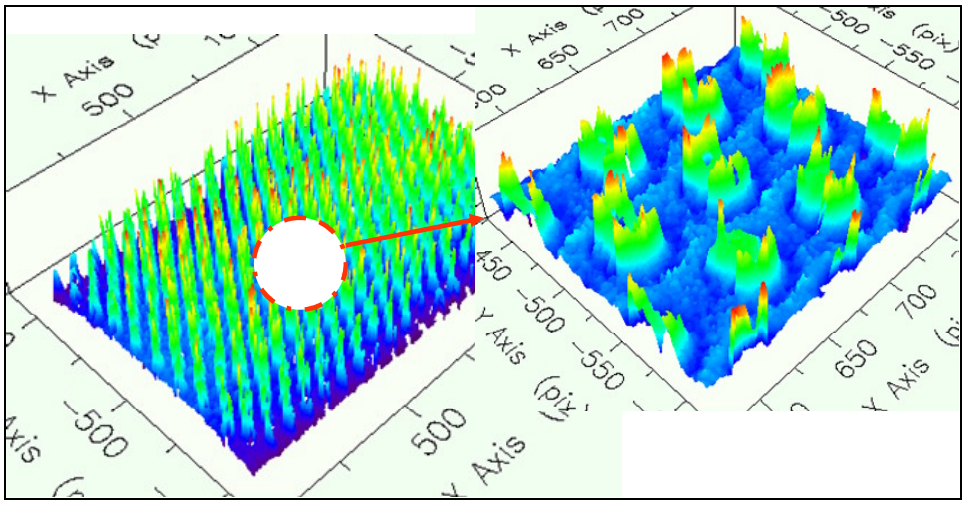

Figure 5-7. The bump field obtained by analyzing the interferograms using commercial fringe analysis program, IntelliWave™. Notice the dips at the middle of each bump due to saturated camera pixels. Also notice the large noise peaks caused by the reflection from the neighboring bumps.

Intel's system provides two bump volume measurement models. In both models it considers the bump volume of the solder portion above the solder resist and adds to it the volume of solder embedded inside the solder resist film (which is assumed to have a thickness of 21 μm). The two models are shown in Figure 5-8. The first model is the geometrical model which treats the solder bump (above and inside the solder resists) as a continuous spherical cap, and calculates the volume using the geometrical equation of the spherical cap volume:

$$V = \frac{1}{6}\pi h\left(\frac{3}{4}d^2 + h^2\right), \tag{5-1}$$

where h and d are the bump height and diameter, respectively.

The second model is called the Volume Pixel Acquisition (VPA) model, which measures the volume of each detected pixel by multiplying the measured height of each pixel by the pixel's area, and then treats the remaining dark portions at the sides of the bumps above the solder resist as a spherical cap and measures its volume using Equation

5-1. Since this model depends on the height value of each pixel for measurements, the presence of the artificial dips at the top of the bumps will introduce errors in estimating the total bump height and volume, most probably underestimating them. This model treats the solder portion below the surface as a cylinder with a diameter equal to the measured bump diameter and a height equal to the solder resist thickness. The total volume is then the sum of the two portions. In order to compare with our measurements, only the geometrical volume is considered, excluding the volume of solder below the surface.

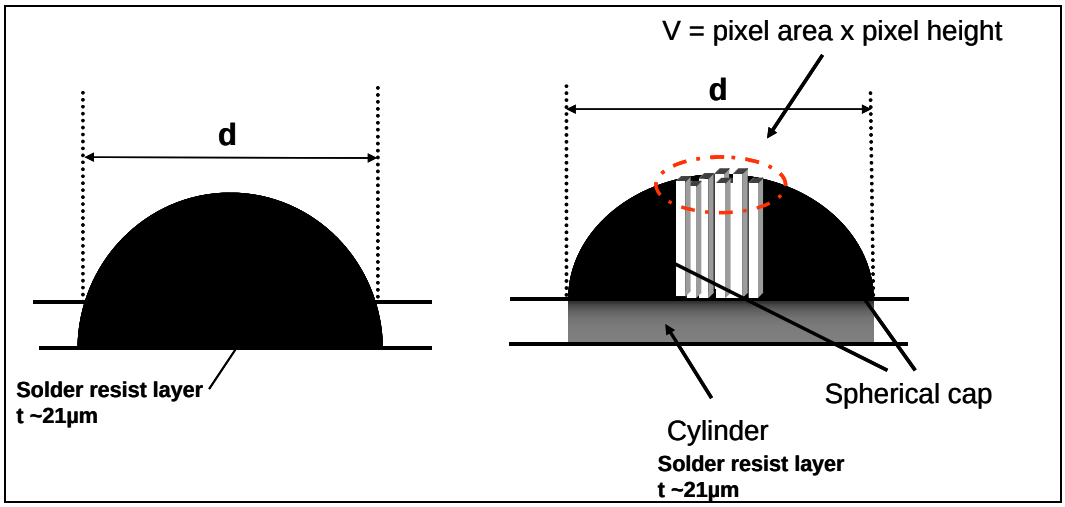

Figure 5-8. Intel's system's volume measurement models. (a) The geometrical model. (b) The volume pixel acquisition model (VPA).

1.15 Individual solder bump measurements using SWLI

The instrument used for measuring individual solder bumps was Zygo NewView™ SWLI. A variety of interferometric objectives with different magnifications is available. A list of these objectives is shown in Table 5-1. For our application, we used the 50× Mirau

objective. From the table, the field of view for this objective is 0.14×0.11 mm^2, which is sufficient to cover slightly more than the area occupied by a single solder bump.

As mentioned before, solder bumps are approximately spherical. As a result, the numerical aperture of the objective is the main limitation, which is around 0.55. Consequently, only a small portion at the top of the bump is measured, and this is the only data available for bump volume estimation. To efficiently utilize the available data, a best fit sphere approach is used to simulate the complete bump and estimate its parameters. The bump height is measured by finding the height difference between the top of the best fit sphere and the substrate best fit plane, the diameter is estimated as the diameter of the circular intersection between the best fit sphere and the substrate plane, and finally, the height and diameter are used to estimate the volume. The detailed procedure is described in Section 3.3.3. The sphere fitting algorithm used to determine the least-squares best fit sphere is described in the next section.

Power	Sys Mag	NA	Working Distance (mm)	Focus Depth (µm)	Inter Depth (µm)	Lateral Res (µm)	Field of View H x V (mm)	Spatial Samp (µm) 320x240	640x480	Max Slope (deg)
1X	20X	0.030	8.5	± 322.5	4.0	11.8	7.0 x 5.3	22.00	11.00	1.41
2.5X	50X	0.075	10.3	± 51.6	4.0	4.72	2.82 x 2.11	8.80	4.40	3.52
5X	100X	0.130	9.3	± 17.2	4.0	2.72	1.41 x 1.06	4.40	2.20	6.08
10X	200X	0.300	7.4	± 3.2	4.0	1.18	0.70 x 0.53	2.20	1.10	13.82
20X	400X	0.400	4.7	± 1.8	3.6	0.88	0.35 x 0.26	1.10	0.55	18.15
50X	1000X	0.550	3.4	± 1.0	2.0	0.64	0.14 x 0.11	0.44	0.22	24.27
100X	2000X	0.800	0.55	± 0.5	1.0	0.45	0.070 x 0.053	0.22	0.11	33.25

Table 5-1. Zygo NewView SWLI objectives characteristics [109].

1.15.1 Sphere fitting algorithm for partial sphere data

The sphere-fitting algorithm is based on finding the least-squares best fit sphere to a set of data that covers a small patch of a sphere (near-planar data) [110]. The algorithm is not suitable for data covering the whole sphere.

To find the least-squares best fit sphere, a set of parameters, $u=[x_o, y_o, z_o, r_o]^T$, are to be determined, where x_o, y_o, z_o are the sphere's center coordinates and r_o is its radius. The following error condition is then defined:

$$e(X;u) = 0, \tag{5-2}$$

which will provide a condition that a point $X = (x, y, z)$ lies on the sphere's surface. The condition defined in 5-2 can be taken as the measure of the error of the fit at a data point $X_i = (x_i, y_i, z_i)$. To find the least-squares fit, we minimize the quantity

$$\sum e^2(X_i;u) \tag{5-3}$$

with respect to the sphere parameters defined by u.

The algorithm uses the following linear sphere equation:

$$S(x,y,z) = A(x^2 + y^2 + z^2) + Rx + Cy + Dz + E = 0. \tag{5-4}$$

Therefore, relations between the coefficients of Equation 5-4 and the sphere parameters are

$$\begin{aligned} x_o &= \frac{-B}{2A}, \\ y_o &= \frac{-C}{2A}, \\ z_o &= \frac{-D}{2A}, \\ r_o &= \frac{-V}{2A}, \text{ where } V = \left(B^2 + C^2 + D^2 - 4AE\right)^{1/2}. \end{aligned} \tag{5-5}$$

The coefficients in Equation 5-4 have to be constrained in order to parameterize the sphere properly, and these constrains should be invariant under translation and rotation.

For the near-planar data, the curvature coefficient, *A*, is expected to be close to zero. The idea is to set one of the parameters *B, C* and *D* to 1. For stability reasons, its preferred to choose the coefficient that have the largest absolute value. The approach used for that is to find the best fit plane to the data, which represent a small spherical cap, to estimate values for *B, C, D* and *E*, and then rotate the data so the normal to the best fit plane points along the positive z axis to constrain the parameter $D = 1$. The rotation will not have an effect on the fitted sphere parameters (its radius and its center) since the data represent a part of a sphere and it's not important which part it is. The rotated data are then fit with the model

$$e_D = A(x^2 + y^2 + z^2) + Bx + Cy + z + E\,. \tag{5-6}$$

By making the data lie close to the plane $z = 0$, the solution values of *A, B, C* and *E* will be small relative to 1. This is the basis of the algorithm described below:

1- Fit a plane to the data set and find estimates for the initial values $\hat{B}, \hat{C}, \hat{D}$ and the centroid $(\hat{x}, \hat{y}, \hat{z})$. The hats on top of these parameters are used to indicate that these are the initial values used before performing the least square fit.

2- Translate the data so that the centroid lies at the origin using

$$(x_i, y_i, z_i) = (x_i, y_i, z_i) - (\hat{x}, \hat{y}, \hat{z})\,.$$

3- Rotate the data using a rotation matrix *U*, which rotates $\hat{B}, \hat{C}, \hat{D}$ to a point on the z-axis:

$$\begin{bmatrix} x_i \\ y_i \\ z_i \end{bmatrix} = U \begin{bmatrix} x_i \\ y_i \\ z_i \end{bmatrix}.$$

4- Solve the linear least-squares system

$$O_D \begin{bmatrix} A \\ B \\ C \\ D \end{bmatrix} = -z$$

where the *i'th* row of O_D is $[(x_i^2 + y_i^2 + z_i^2), x_i, y_i, 1]$, and the *i'th* component of *z* is z_i.

5- Calculate the parameters for the untransformed data according to

$$\begin{bmatrix} \hat{B} \\ \hat{C} \\ \hat{D} \end{bmatrix} = U^T \begin{bmatrix} B \\ C \\ 1 \end{bmatrix},$$

$$\begin{aligned} B &= \hat{B} - 2A\hat{x}, \\ C &= \hat{C} - 2A\hat{y}, \\ D &= \hat{D} - 2A\hat{z}, \\ E &= A(\hat{x}^2 + \hat{y}^2 + \hat{z}^2) - \hat{B}\hat{x} - \hat{C}\hat{y} - \hat{D}\hat{z} + E. \end{aligned}$$

1.15.2 Individual bump measurement procedure

In this experiment, three different solder bump packages from different suppliers were measured. The part and suppliers' names are Intel's classified information. The letters A, B, and C are used to indicate the different parts.

On each part, five randomly selected bumps were measured using the Zygo NewView SWLI located at the Center for Precision Metrology at UNC-Charlotte. The parts were previously measured at Intel's assembly materials characterization lab.

Two dimensional maps of the bump fields showing the bump locations for each part were printed, and five selected bumps on each map were located and properly marked for later comparison with Intel's measurements.

First, the part was placed on the stage and the 10× objective was used to view the complete bump field so the selected bump was easily located. At this magnification, the light intensity adjusts automatically (by pressing the F5 button). The part's z-location was varied until interference fringes were observed. The stage tip/tilt was then adjusted to get a null fringe position, but since the bump field has variable height variations it was difficult to obtain a total null, so the tip/tilt was adjusted until a minimum number of fringes was obtained. Once this was done, the desired bump was located and placed at the center of the field of view. The turret was then rotated to switch to the 50× objective, so the field of view was covered by the test bump. The light was then automatically adjusted to get a clear image of the bump.

To obtain interference fringes, the part's z-location was slowly varied until fringes were observed on the substrate surface. The manual light intensity adjustment was used in order to make sure that the camera was not saturated at any z level. This is done by activating the manual adjustment by pressing the F4 key, which opens a live intensity image of the part with red areas indicating saturated pixels. By starting a z-direction scan the intensity can be reduced until red pixels are no longer present.. This was done over the entire height of the bump to ensure that the camera pixels are efficiently used and utilized to get the maximum possible amount of data.

The bump height values range from 25- 50 μm. To make sure this range was covered, the extended scan option was selected in Metropro^{TM} and the scan range was set to 75 μm.

The part's z-location was then adjusted to focus on the substrate surface, or a little below. Now, the instrument was ready to measure the part. The measurement was then started and the instrument scanned through the bump until the 75 μm scan range was covered. A compete measurement lasts for approximately 70 seconds.

Once the measurement was complete, Metropro^{TM} analyzes the data to obtain the complete 3-D height profile. Figure 5-9 shows a snapshot of the Metropro^{TM} screen showing the measurement results. The measurement was saved as a Metropro^{TM} data file (.dat) which was later converted to a text file to be analyzed by Matlab^{TM}.

In order to estimate the measurement repeatability, each bump was measured 10 times, and all the data files were saved for further analysis. A total of 150 data files were saved (3 parts, 5 bumps/part, and 10 runs/bump).

1.15.3 Estimating the bump parameters and the uncertainties

After Metropro^{TM} data files were saved, they were converted to a format that is readable by Matlab^{TM}. This was done using a Matlab^{TM} patch file called "dat_to_xyz" which accepts a Metropro^{TM} ".dat" file and converts it to text. The text file contains three columns and 307,200 rows which is the total number of data points (640×480 pixels). The first and second columns are the x and y pixel locations, the third column is the pixel's z-height in micrometers. The x and y locations are later converted to micrometers by multiplying by the instrument's lateral scale factor.

In order to estimate the bump parameters from the measurement, the sphere fitting algorithm discussed in Section 3.3.1 was used to find the least square best fit sphere to the bump data. The bump parameters are defined in Figure 5-10. The bump height (h) is the distance from the top of the best fit sphere to the substrate's best fit plane. The bump

diameter (d) is the diameter of the circular intersection between the best fit sphere and the substrate's best fit plane, and the bump radius (r) is the radius of the best fit sphere, and the bump volume (V) is the volume of the best sphere's portion above the substrate.

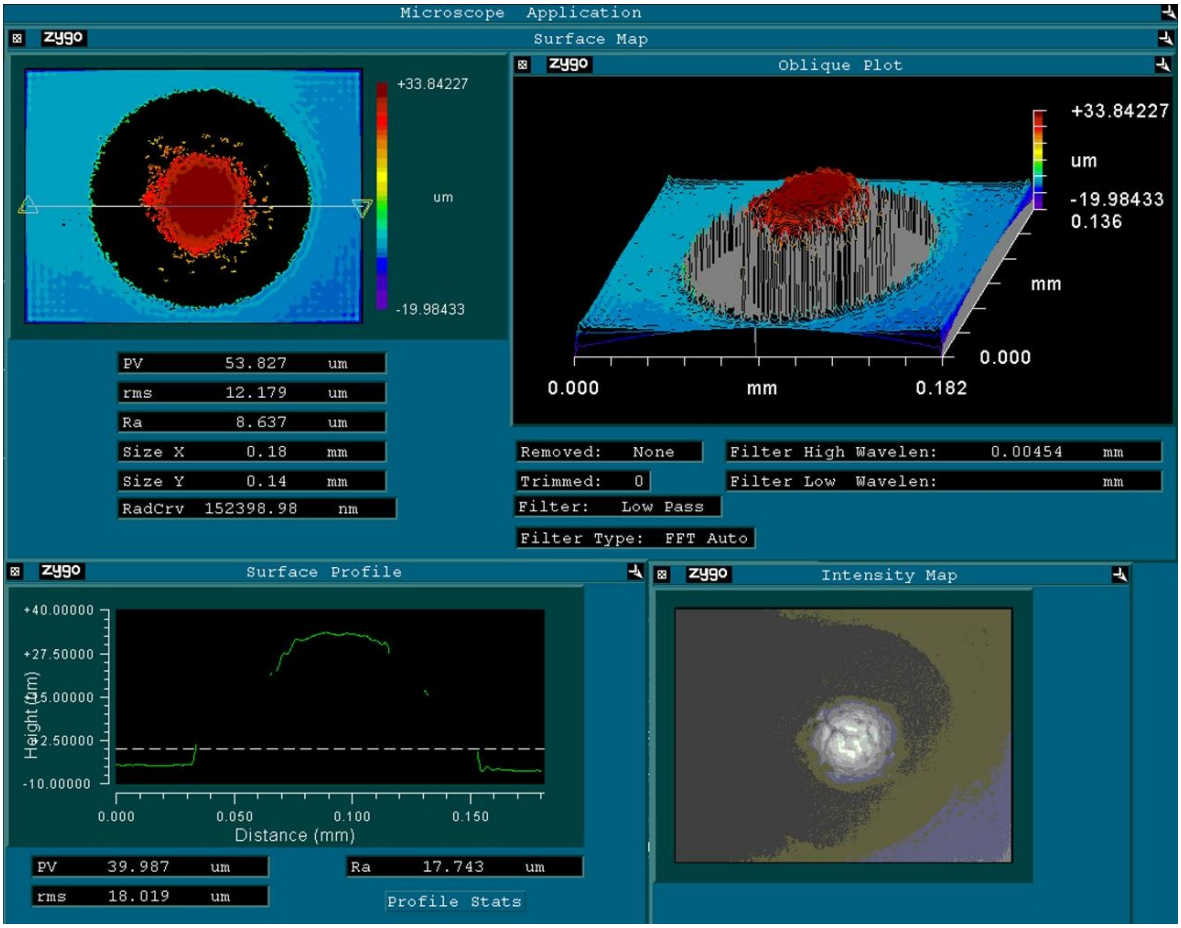

Figure 5-9. A snapshot of the Metropro™ screen showing the measurement results. The top-left image is the 2-D height map where different height values are presented by different colors. Underneath is a 2-D cross sectional profile across the line shown at the middle of the top-left image. The top right image is the 3-D map of the bump, and underneath it is a gray-scale intensity map.

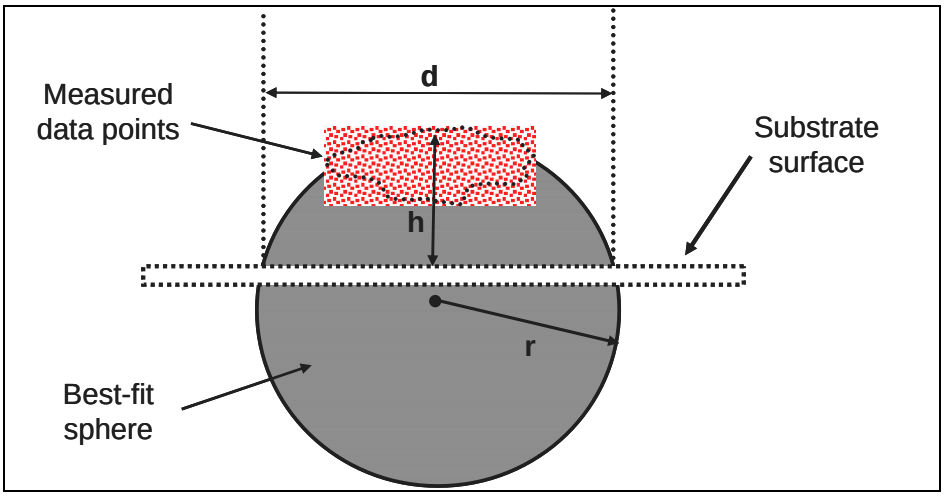

Figure 5-10. Parameters of the best fit sphere of the bump data.

The diameter and volume of the best fit sphere are calculated using the spherical cap formulas [111]

$$d = 2\sqrt{r^2 - (r-h)^2} \tag{5-7}$$

and

$$V = \frac{1}{6}\pi h\left(\frac{3}{4}d^2 + h^2\right). \tag{5-8}$$

The repeatability for each parameter is taken to be the standard deviation from the analysis of the group of ten measurements, but this is not a good estimate of the combined uncertainties. Instrument calibration also contributes. The full combined uncertainty was estimated with a Monte Carlo simulation.

The best way to estimate the uncertainty in the lateral calibration is to calibrate the instrument several times and then calculate the standard deviation. This was not an option since it would have affected the instrument's calibration that has been used in the past. Instead, we used the original calibration uncertainty given by Zygo which was ~ 0.35% for

the 50× objective. And for the height values, the uncertainty for measuring an artifact with a 50 μm height is ~ 0.4%. Therefore, a 0.4% uncertainty was used for all dimensions, x, y and z.

To apply the Monte Carlo approach, a Gaussian random error of 0.4% is added to the lateral calibration factor (0.275 μ/pixel) and then multiplied by the x and y values. A 0.4% random error was also added to the z values. The sphere fitting algorithm was then applied and the bump parameters were calculated. For each one of the 10 repetitions per bump, the Monte Carlo simulation is repeated 10 times, and the standard deviation of the parameter values is used as an estimate of the uncertainty due to the calibration uncertainty ($U_{montecarlo}$). After that, the mean parameter values from the Monte Carlo simulation in all 10 repetitions were calculated and this standard deviation used as an estimate for the uncertainty due to the repeatability ($U_{repeatability}$) is found. The combined uncertainty for each parameter is then calculated using the following expression:

$$U_C = \sqrt{U^2_{montecarlo\_\max} + U^2_{repeatability}} \tag{5-9}$$

where $U_{montecarlo\_\max}$ is the maximum uncertainty from all the Monte Carlo runs.

The detailed procedure for estimating the parameters of one bump goes as follows:

1- Open the text file containing the data for the first repetition, save the x values in an array (X), the y values in (Y), and the z values in (Z). Figure 5-11 shows a 3-D plot of the original bump data. Notice the large amount of missing data at the sides due to the limited objective's NA.

2- Fit a plane through the substrate data points and then subtract the plane from the original data to remove the tilt and offset as shown in Figure 5-12.

3- Add a 0.4% Gaussian random error to the data points in X, Y and Z, and then multiply X and Y by 0.275 to convert from pixels to micrometers.

4- Separate the data points corresponding to the bump from the substrate data points.

5- Apply the complete sphere fitting algorithm described in Section 3.3.1, (steps 1-5), to find the best fit sphere parameters *A*, *B*, *C*, *D* and *E*.

6- Find the sphere parameters x_o, y_o, z_o *and* r_o using Equation 5-4 .

7- Using the plane fit to the substrate data, estimate the bump height by calculating the height difference between the peak point of the best fit sphere and the substrate best fit plane.

8- Calculate the bump diameter and volume using Equations 5-7 and 5-8 respectively, where the sphere radius is the one found in step 8, $r = r_o$.

9- Repeat steps 3-10 for the same repetition data set and then calculate the standard deviation for the bump parameters, (*h*, *d*, *r* and *V*). This is $U_{montecarlo}$ for this repetition.

10- Repeat steps 1-11 for the remaining 9 repetitions.

11- For each bump parameter, take the mean value from each repetition, average them, and then calculate the standard deviation. This is $U_{repeatability}$.

12- To find $U_{montecarlo\_max}$ for each bump parameter, take the maximum $U_{montecarlo}$ found among all repetitions. This is $U_{montecarlo\_max}$.

13- For every parameter, calculate the combined uncertainty using Equation 5-9.

Figure 5-13 shows a 3-D plot of the best fit bump for the data shown in Figure 5-12.

The Matlab™ functions used in this algorithm are found in Appendix B.

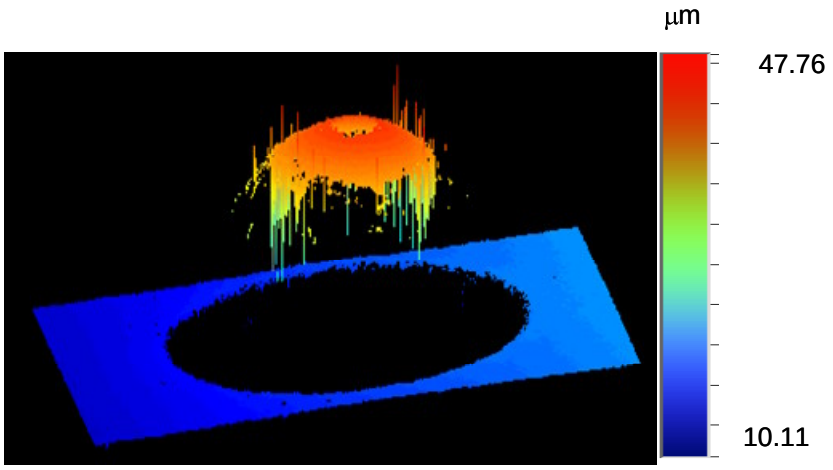

Figure 5-11. Original bump data as measured by Zygo's SWLI.

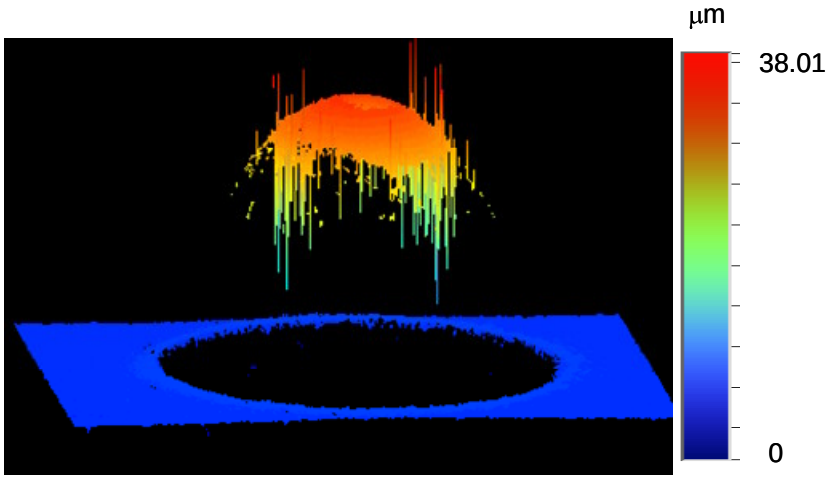

Figure 5-12. The bump data after subtracting the tilt and bias.

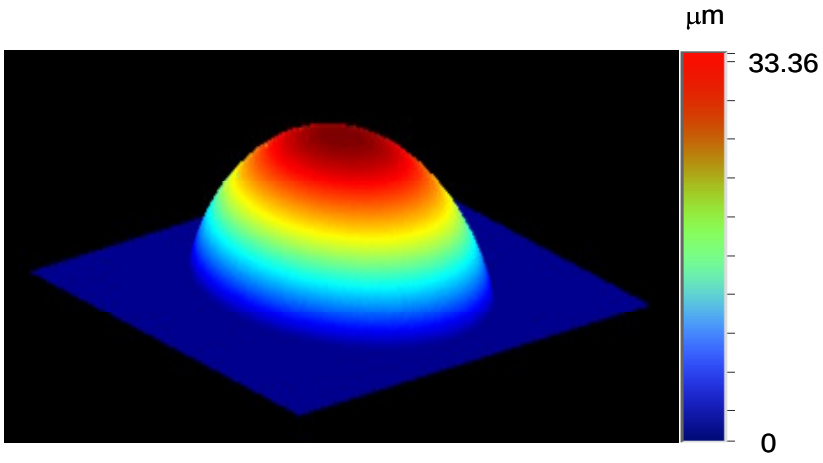

Figure 5-13. The best fit bump to the data in Figure 5-12.

1.15.4 Results and comparison

The procedure described above was used to estimate the parameters for 5 bumps on each of the 3 parts. The same bumps were measured using Intel's tool, with 30 repetitions per bump. The following tables and charts show and compare the results.

Part A

		Height (um)	*Height Unc. (um)*	*error %*	*Diameter (um)*	*Diameter Unc. (um)*	*error %*	*Volume (um^3)*	*Volume Unc. (um^3)*	*error %*
B1	Intel	38.05	0.18	0.46	91.84	0.11	0.12	2.82E+05	1.33E+03	0.47
	SWLI	39.99	0.02	0.06	88.16	0.36	0.40	2.75E+05	2.11E+03	0.77
B2	Intel	35.48	0.13	0.38	103.86	0.13	0.12	3.64E+05	1.35E+03	0.37
	SWLI	32.60	0.04	0.11	100.82	0.19	0.19	3.40E+05	1.58E+03	0.46
B3	Intel	34.96	0.24	0.68	101.64	0.22	0.21	3.50E+05	2.40E+03	0.68
	SWLI	38.25	0.01	0.04	106.23	0.30	0.28	3.96E+05	2.47E+03	0.62
B4	Intel	37.23	0.13	0.34	103.32	0.11	0.10	3.72E+05	1.26E+03	0.34
	SWLI	38.25	0.001	0.003	103.57	0.07	0.07	3.75E+05	5.42E+02	0.14
B5	Intel	33.36	0.24	0.70	89.92	0.09	0.10	2.50E+05	6.76E+02	0.27
	SWLI	36.46	0.08	0.2	89.45	2.04	2.28	2.70E+05	1.31E+04	4.84

Table 5-2. Measurement result for part A.

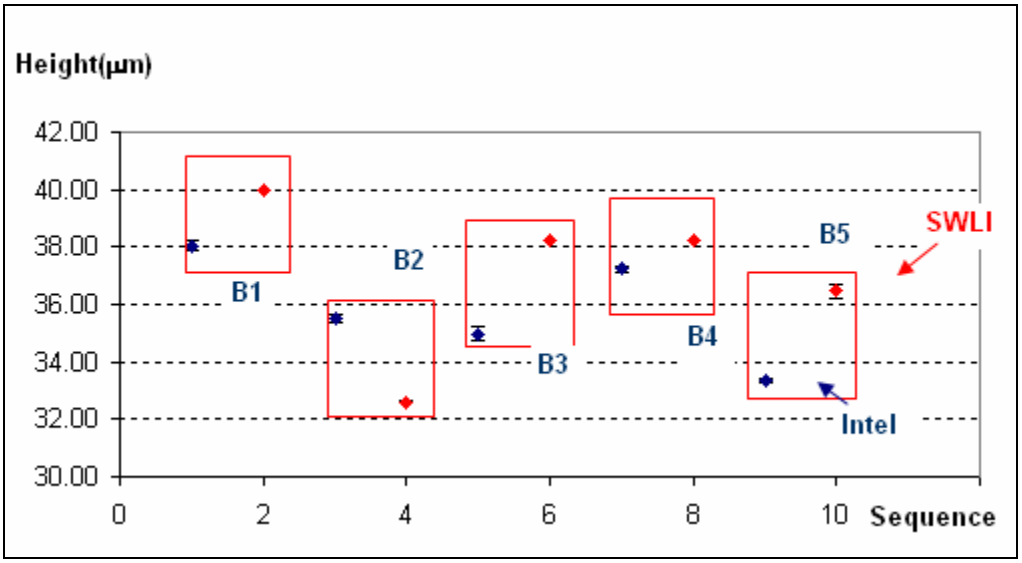

Figure 5-14. Height comparison chart for part A.

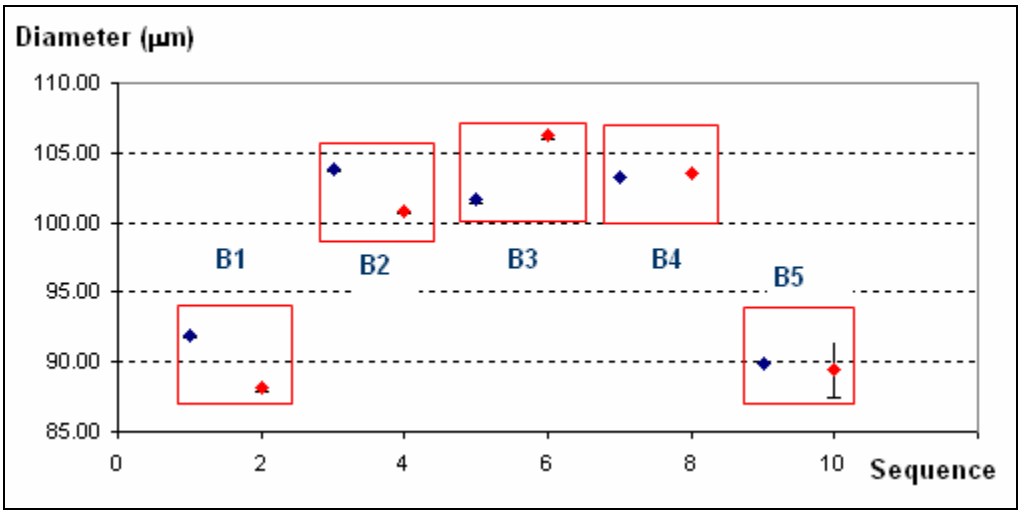

Figure 5-15. Diameter comparison chart for part A.

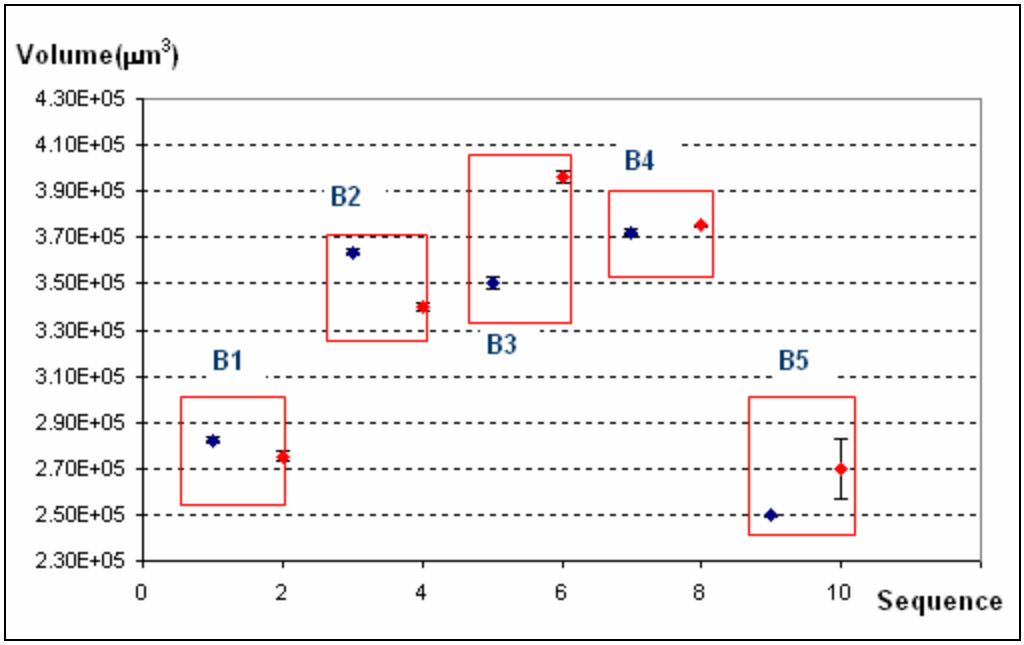

Figure 5-16. Volume comparison chart for part A.

Part B

		Height (um)	*Height Unc. (um)*	*error %*	*Diameter (um)*	*Diameter Unc. (um)*	*error %*	*Volume (um^3)*	*Volume Unc. (um^3)*	*error %*
B1	Intel	25.23	0.20	0.79	100.17	0.29	0.29	2.92E+05	2.01E+03	0.69
	SWLI	31.00	0.01	0.03	107.76	0.07	0.07	4.04E+05	7.20E+02	0.18
B2	Intel	33.03	0.14	0.43	107.91	0.15	0.14	3.67E+05	1.53E+03	0.42
	SWLI	34.76	0.01	0.03	110.04	0.19	0.17	4.22E+05	1.75E+03	0.41
B3	Intel	32.05	0.13	0.40	106.67	0.15	0.14	3.55E+05	1.44E+03	0.41
	SWLI	34.45	0.01	0.02	107.68	0.10	0.10	4.01E+05	9.38E+02	0.23
B4	Intel	34.04	0.16	0.46	108.61	0.16	0.15	3.83E+05	1.75E+03	0.46
	SWLI	33.32	0.01	0.02	105.82	0.11	0.11	3.77E+05	1.01E+03	0.29
B5	Intel	31.11	0.21	0.69	105.52	0.26	0.25	3.45E+05	2.38E+03	0.69
	SWLI	33.03	0.01	0.03	109.29	0.13	0.12	4.15E+05	1.28E+03	0.31

Table 5-3. Measurement results for part B.

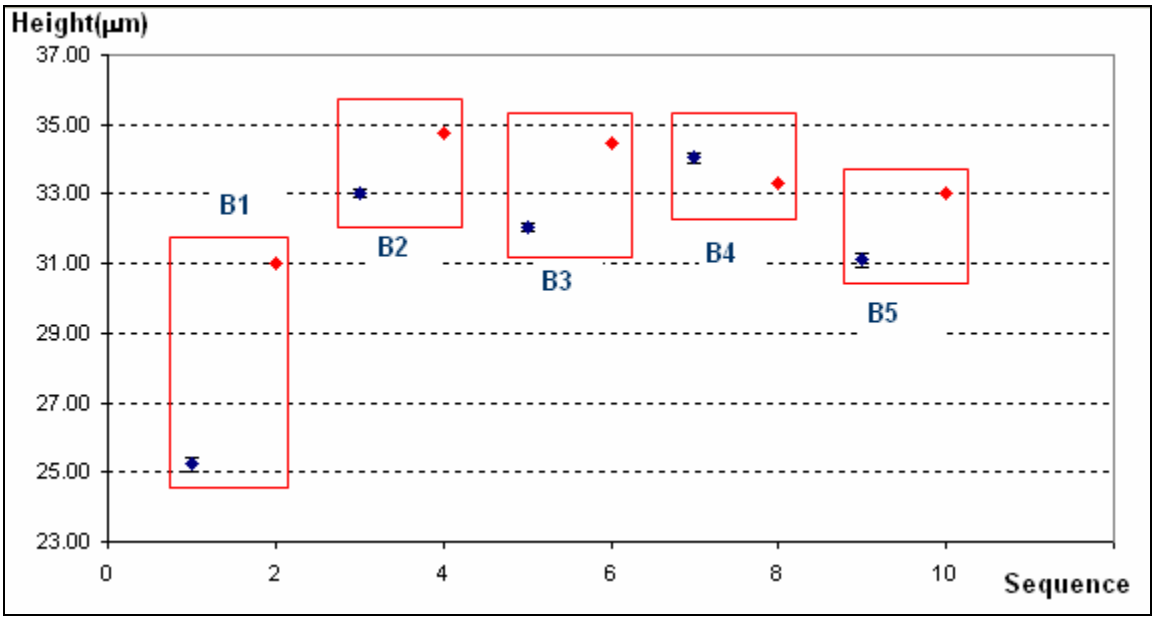

Figure 5-17. Height comparison chart for part B.

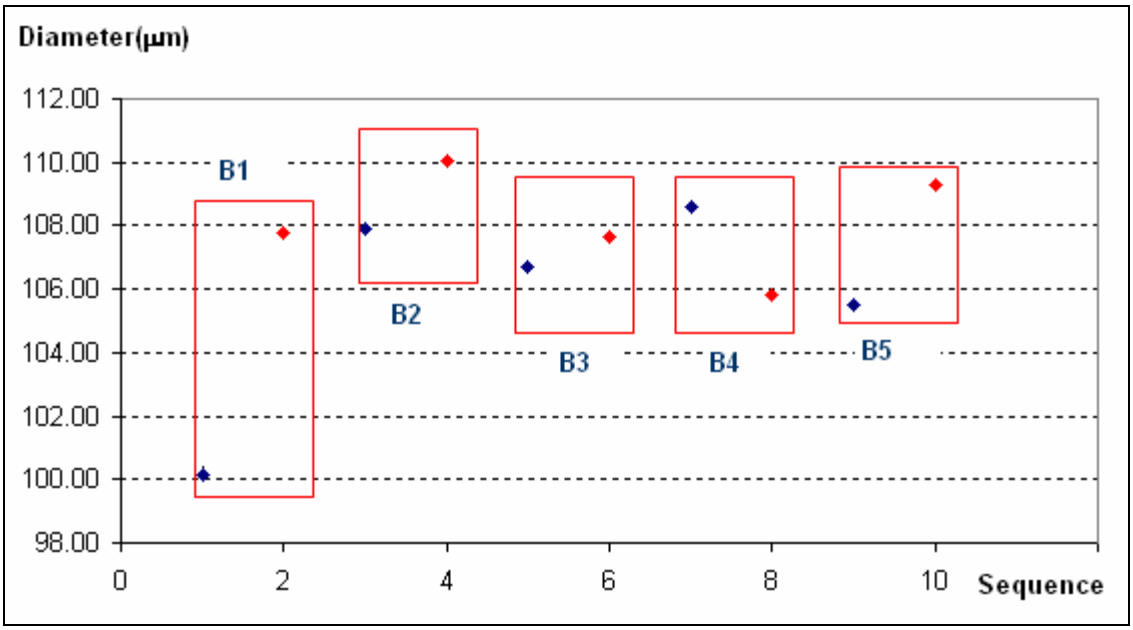

Figure 5-18. Diameter comparison chart for part B.

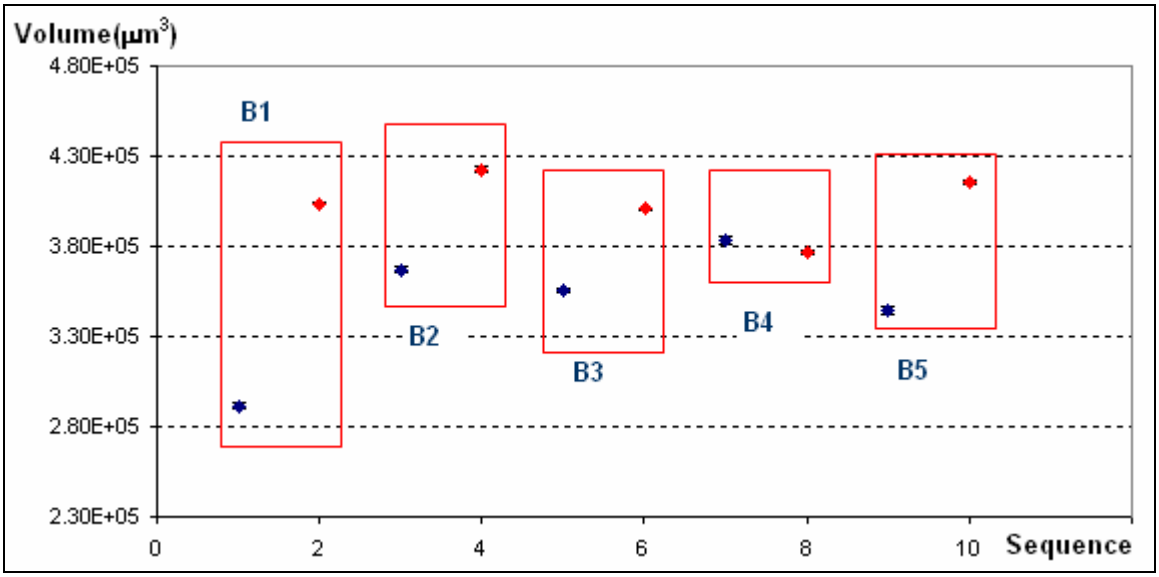

Figure 5-19. Volume comparison chart for part B.

Part C

		Height (um)	Height Unc. (um)	error %	Diameter (um)	Diameter Unc. (um)	error %	Volume (um^3)	Volume Unc. (um^3)	error %
B1	Intel	28.70	0.24	0.83	99.42	0.31	0.32	3.01E+05	2.44E+03	0.81
	SWLI	31.69	0.29	0.91	107.96	0.38	0.35	4.04E+05	3.32E+03	0.82
B2	Intel	29.90	0.52	1.72	100.87	0.54	0.54	3.13E+05	4.93E+03	1.57
	SWLI	33.87	0.08	0.24	104.93	0.07	0.07	3.76E+05	6.45E+02	0.17
B3	Intel	32.03	0.46	1.45	103.30	0.44	0.42	3.35E+05	4.51E+03	1.35
	SWLI	34.05	0.10	0.30	107.84	0.07	0.06	4.02E+05	6.27E+02	0.16
B4	Intel	27.44	0.50	1.82	84.83	0.44	0.52	2.05E+05	3.41E+03	1.66
	SWLI	32.61	0.03	0.08	92.10	0.16	0.17	2.74E+05	1.07E+03	0.39
B5	Intel	31.17	0.31	0.99	87.51	0.25	0.29	2.30E+05	2.29E+03	0.99
	SWLI	33.19	0.02	0.05	104.89	0.24	0.23	3.75E+05	2.13E+03	0.57

Table 5-4. Measurement results for part C.

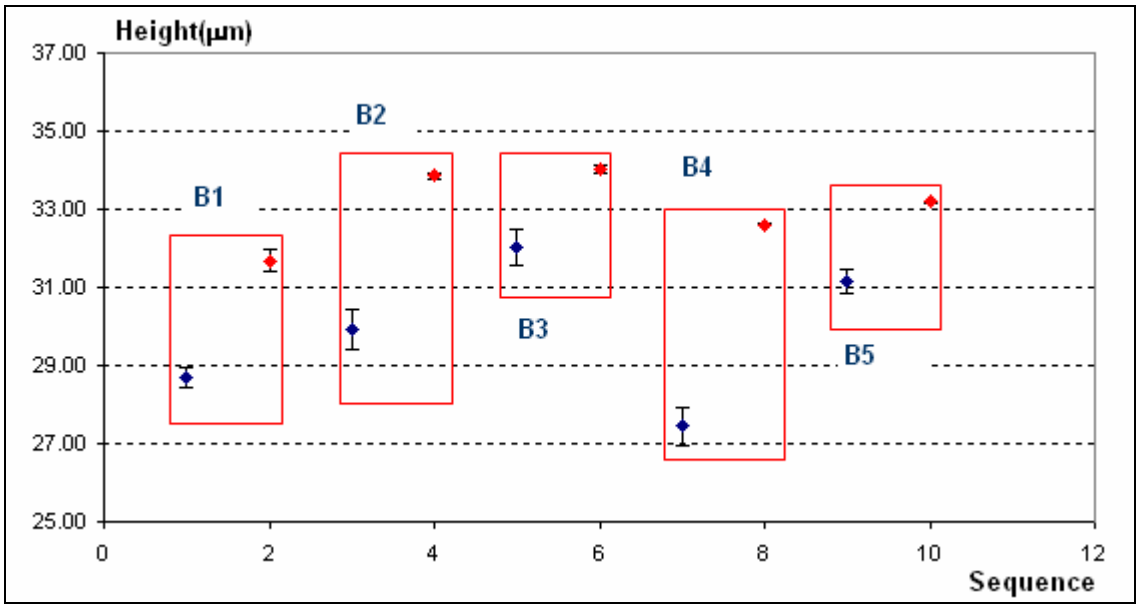

Figure 5-20. Height comparison chart for part C.

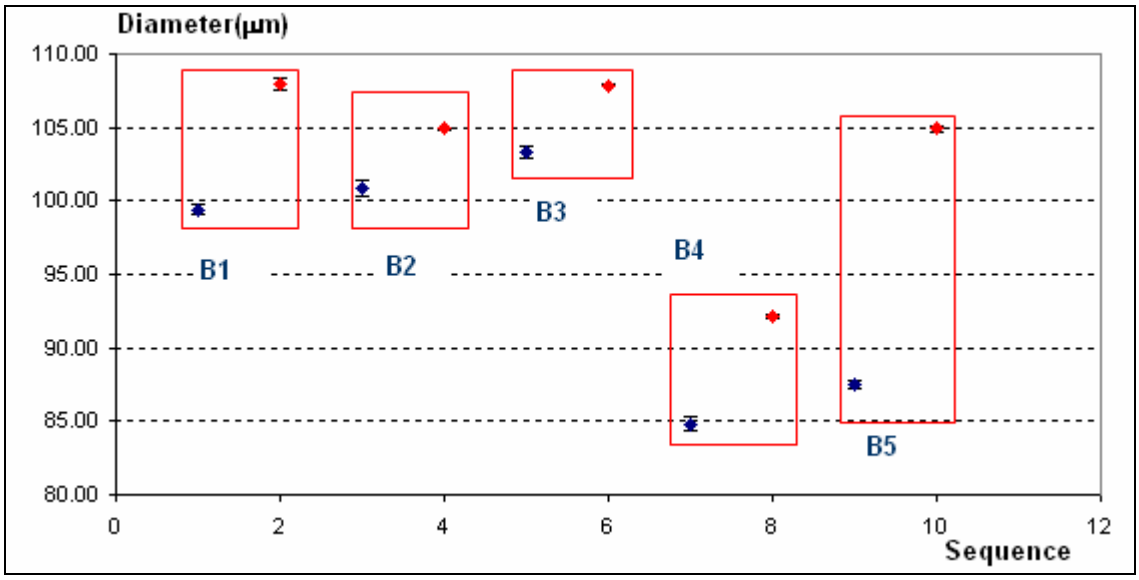

Figure 5-21. Diameter comparison chart for part C.

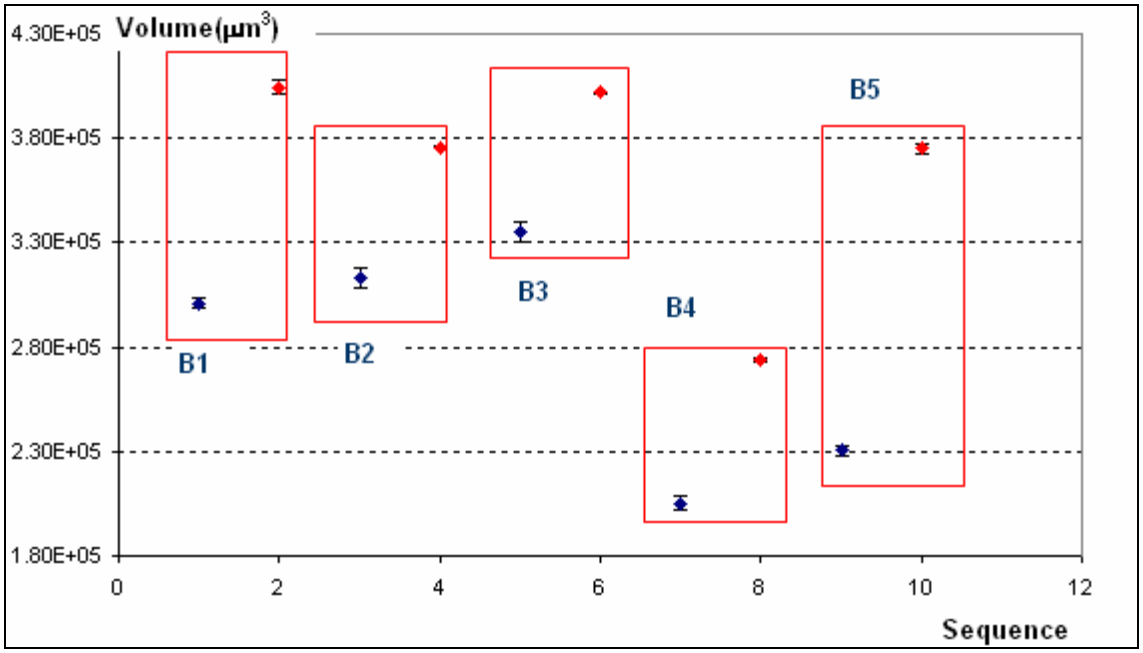

Figure 5-22. Volume comparison chart for part C.

Correlation results for all bumps:

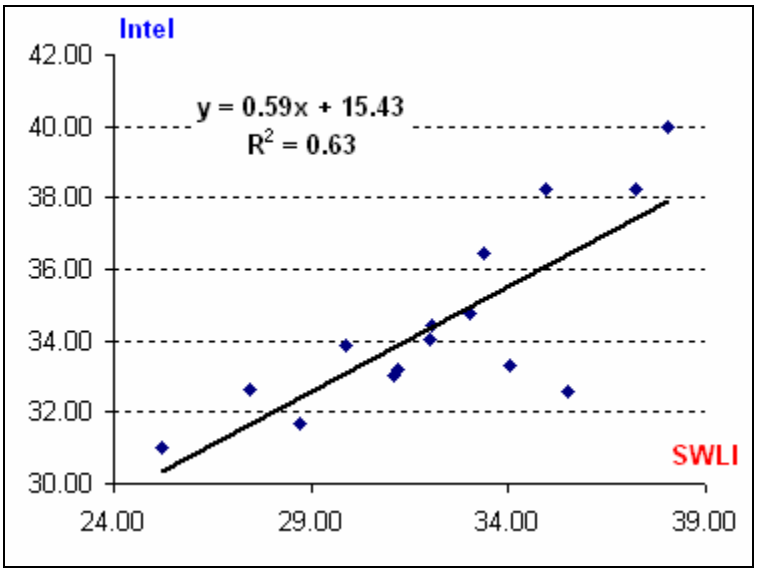

Figure 5-23. Height correlation results.

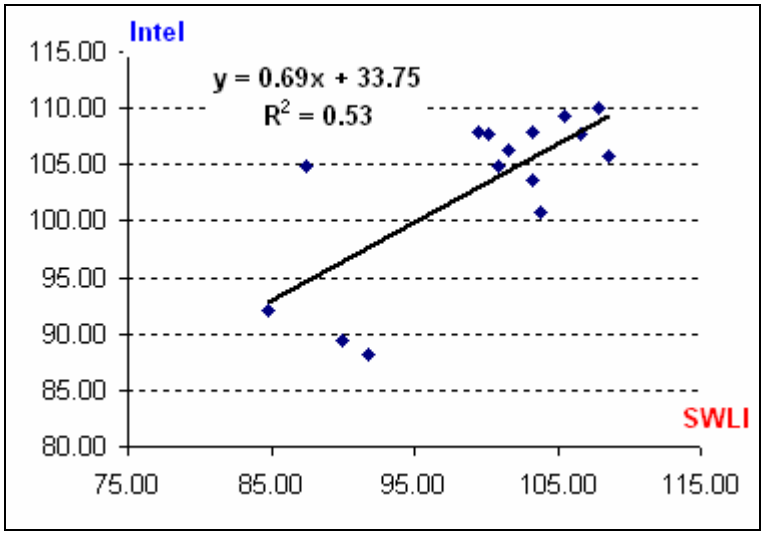

Figure 5-24. Diameter correlation results.

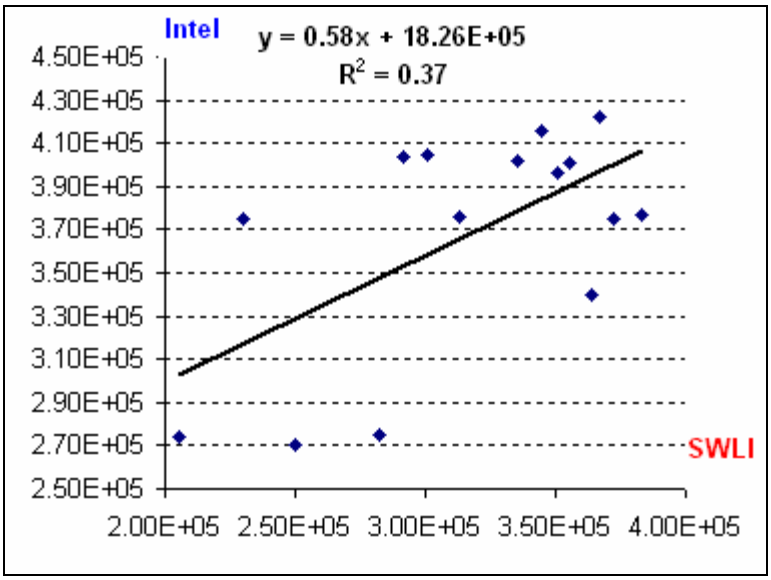

Figure 5-25. Volume correlation results.

The comparison shows a poor correlation with R^2 ~ 64% for height measurements and ~ 53% for diameter measurements, and a poorer correlation with R^2~ 37% for the volume. If bumps 2 and 3 from part A are excluded from the correlation, the R^2 for the height measurements increases to ~ 81% which indicates a fairly good agreement, but the diameter and volume measurements have weak agreements. The approaches to estimating the diameter is likely the major source of discrepancy between methods. As mentioned above, Intel's tool uses a ring of LEDs to illuminate the bump field at a low angle to the substrate (~ 7º). Although the angle is small, the illumination will cause a ring to appear near the base of the bump but not exactly at the substrate level, as shown in Figure 5-26. The tool then uses the measured diameter of this ring and the measured bump height in a 'classified' algorithm to estimate the bump diameter at the base. Our approach uses the measured bump and substrate data and then estimates the bump diameter by finding the intersection between the best fit sphere and the substrate. Since the volume equations in

both methods depend on the square of the diameter, the diameter discrepancies significantly contribute to the volume calculations. One more cause of the height discrepancy may be that Intel adds a bias to the height measurements to correlate with the other bump measurement tools.

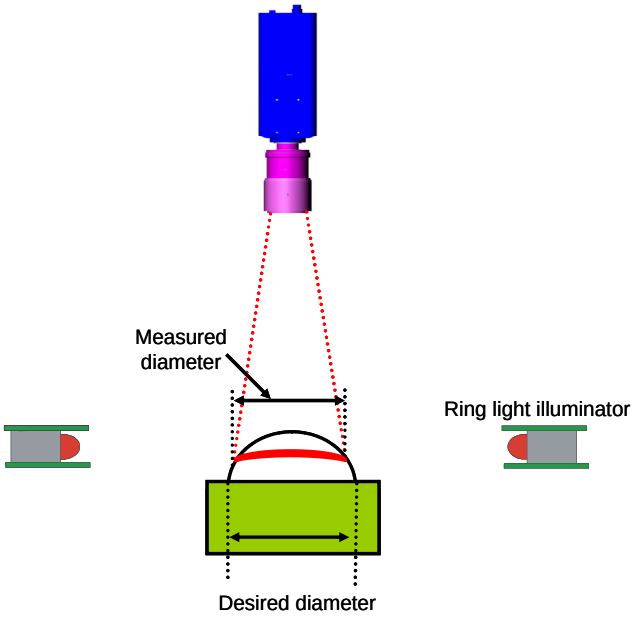

Figure 5-26. Intel's tool 2-D measurement scheme. Notice the difference between the measured diameter and the desired one.

1.16 Measuring solder bump arrays using our fringe projection system

The smallest field of view of our system is ~ 1.2 ×0.9 mm. In a solder bump field, this covers a bump array of approximately 6×5 bumps. At this magnification, the area occupied by one full bump, including the dark area around the edge, is roughly covered by 50×50 pixels. Therefore the area that actually contains valid data points at the top of the bump is covered by less than 20×20 pixels. Choosing a larger field of view (smaller magnification), will allow measuring more bumps but with fewer pixels per bump, leading

to less reliable measurements. For this reason the highest magnification (smallest field of view) was chosen for our measurements.

As discussed in Section 3.2, the high reflectivity of the solder material and the specular surface finish place constraints on the light intensity that can be used to project the gratings. To minimize the speckle effect due to stray reflections from adjacent bumps and to reduce the intensity from the top of the bumps, a polarizer was placed in front of the projection arm, and another polarizer, (called the analyzer), rotated 90º with respect to the first was placed in front of the camera. In general, the polarization of the specularly reflected light does not change, and hence most of the specular light will be blocked by the second polarizer. The diffusely reflected light is randomly polarized and a good portion passes through the analyzer. This minimizes the speckle, but since the bump material reflectivity is much larger than the substrate reflectivity, the intensity of the light from the bumps is still large compared to the substrate, causing the bump surface to blur and most of the time the camera to saturate. Decreasing the light intensity reduces the blur but significantly decreases the light reflected from the substrate, causing low fringe contrast in the substrate areas of the surface.

To minimize this, we took advantage of the reflectivity properties of the bump and substrate materials. The solder material is silver indicating a high reflectivity over the visible spectrum. On the other hand, the substrate appears green, so the reflectivity is largest in the green part of the spectrum. A green filter in front of the projection arm allows only green light to be projected. This blocks approximately two thirds of the light reflected of the bump compared to white light projection, and at the same time

maximizing the light reflected from the substrate. Therefore, a green light filter combined with the polarizer combination maximizes the fringe contrast.

1.16.1 Preparing the system for measurements

The same pre-measurement steps discussed in Section 4.5 were followed. First, the bias correction profile at the system's maximum magnification was obtained by measuring the same Mitutoyo gauge block with a grating period ~1 mm (on the LCD panel plane). The measurement was repeated 50 times at randomly selected locations on the gauge block surface with a (2π/50) phase shift added to the grating each time to reduce the fringe bleed through by averaging. The 50 measurements were then averaged to get the bias correction profile shown in Figure 5-27.

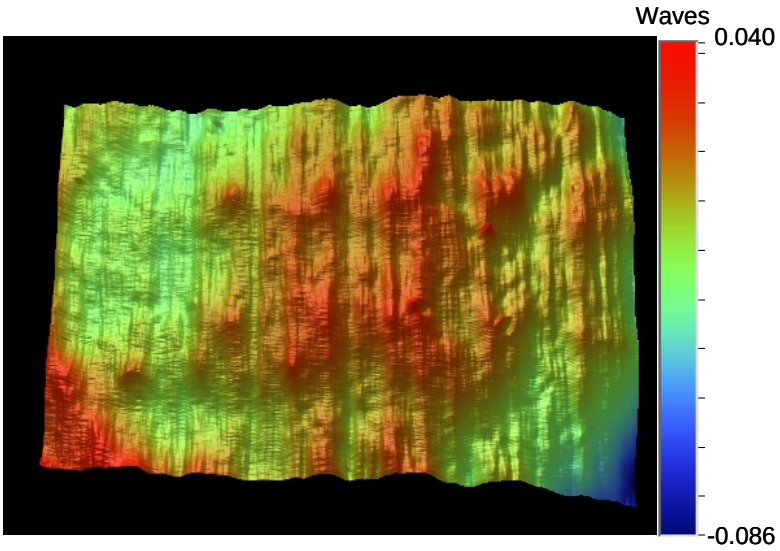

Figure 5-27. System bias correction OPD at the maximum magnification, using a 1 mm grating period.

The bias correction OPD shown in Figure 5-27 was used to generate fringes and measure the 23.23 μm VLSI step height for z-calibration. An average of 20 measurements was taken, and the multi regional analysis algorithm in Vision^{TM} was used to obtain the

equivalent wavelength. Figure 5-28 shows the obtained phase map of the step-height, and Figure 5-29 shows the multi-regional analyses results. The step height was measured to be 0.093 ± 0.006 waves and therefore the equivalent wavelength was calculated to be 251 ± 16 µm/wave.

Edmund's 10mm cross line scale was used for lateral calibration. Figure 5-30 (a) and (b) show the calibration results for the x and y dimensions, respectively. The x calibration factor was estimated to be 1.920 ± 0.007 µm/pixel, and for y calibration the factor was 2.292 ± 0.012 µm/pixel. As described in Section 4.4.3, the uncertainty in the lateral calibration factors was obtained by assuming 2 pixels error in placing the cursor on the exact label position on the scale.

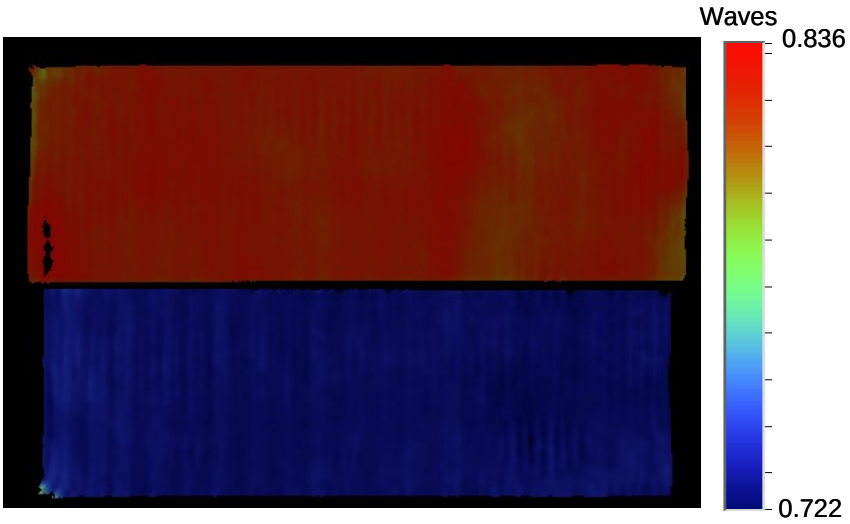

Figure 5-28. Step height OPD map.

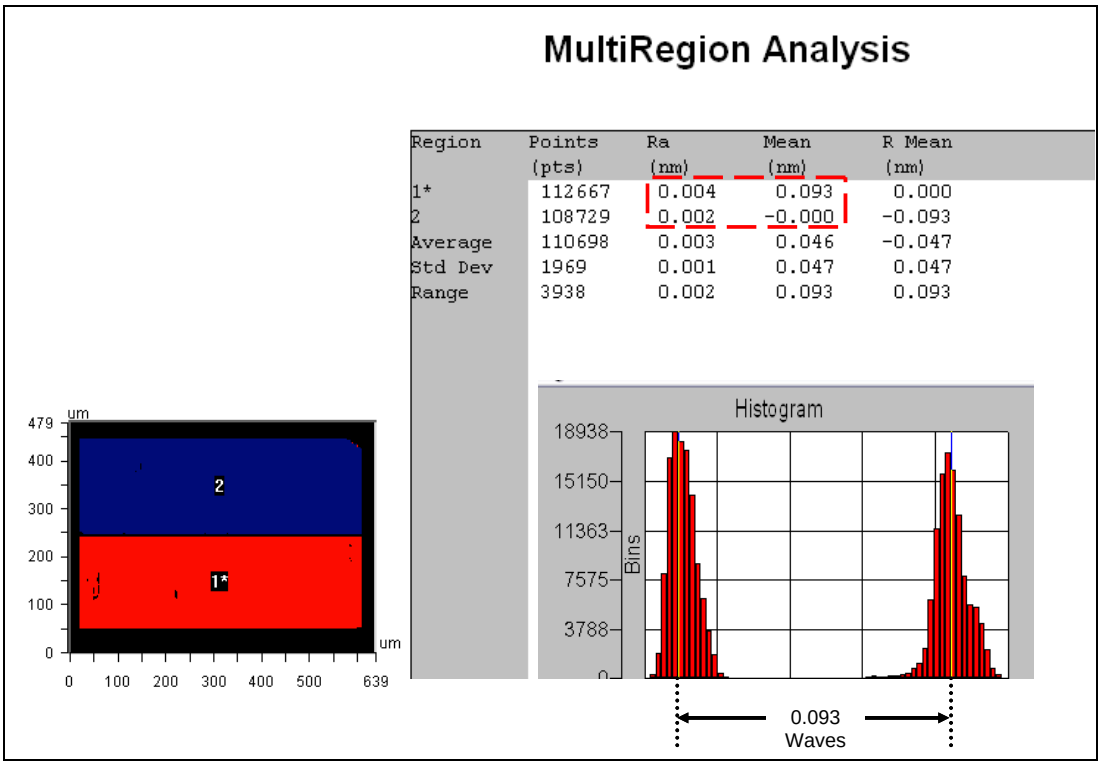

Figure 5-29. The multi regional analysis results for the 23.23 µm VLSI step-height at the maximum system magnification and 1 mm fringe period.

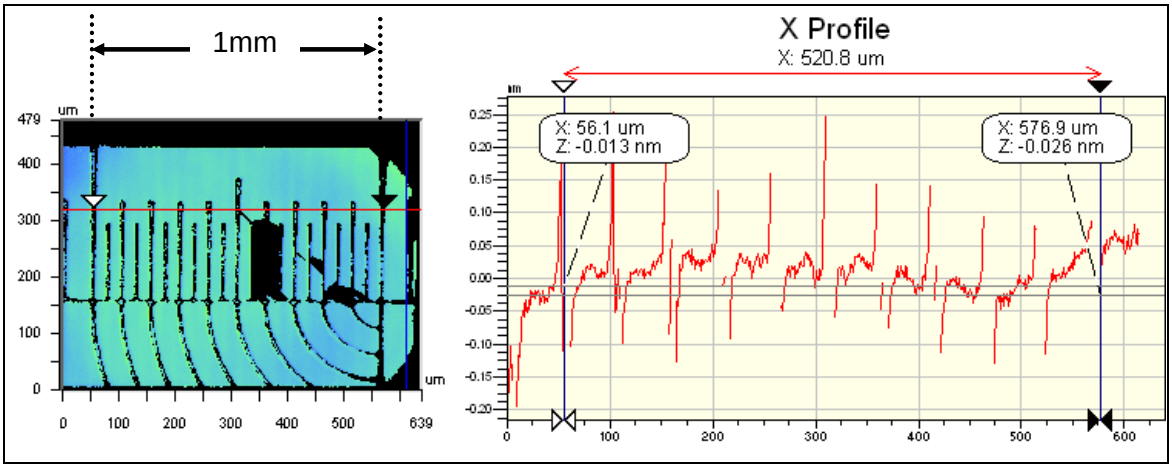

(a)

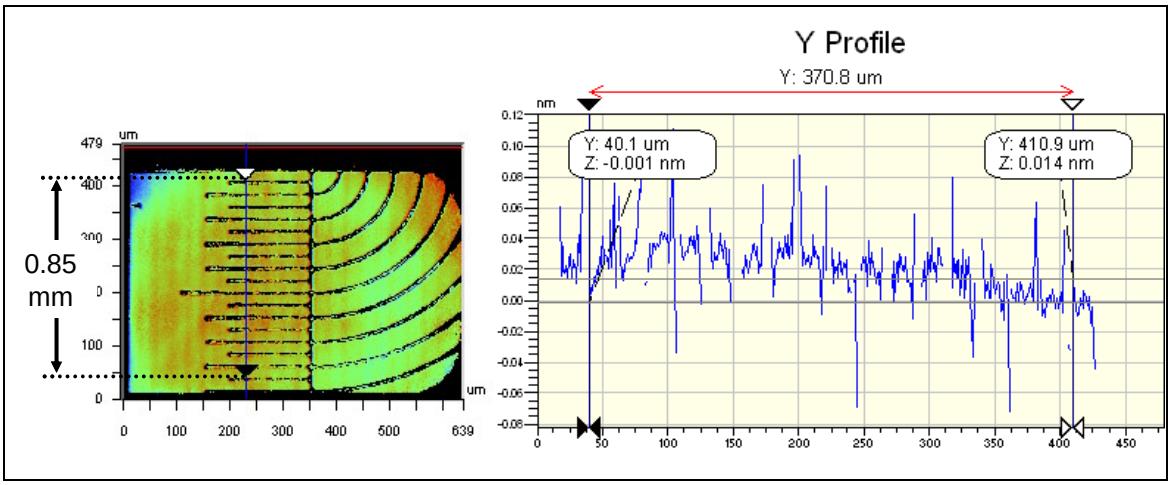

(b)

Figure 5-30. Lateral calibration results. (a) Figures showing x-axis calibration. (b) Figures showing y-axis calibration.

1.16.2 Measurement procedure

The test part was placed under the system for measurement after calibration. The light was adjusted to minimize pixel saturation by adding extra neutral density filters in addition to the green filter and the polarizers. The bias correction OPD obtained in the previous section was used to create and project the fringes, and 8-phase shifted frames were captured. Figure 5-31 shows a window in the first four frames. Notice how the intensity of the light at the top of the bumps is changing with the phase shifting. Notice also the bright dots surrounding each bump due to specular reflection from the neighboring bumps. These are masked out before analyzing the interferograms.

The interferograms were then analyzed using Vision^{TM}. Figure 5-32 shows the obtained OPD map for this measurement. The software had difficulty unwrapping the phase map which leads to the stepped background in the map. After testing different surfaces, including surfaces other than solder bumps, it became clear that the software

fails to unwrap OPD maps with large discontinuities from data drop out. Data drop out is always present in a bump field measurement due to the large slopes at the bump edges.

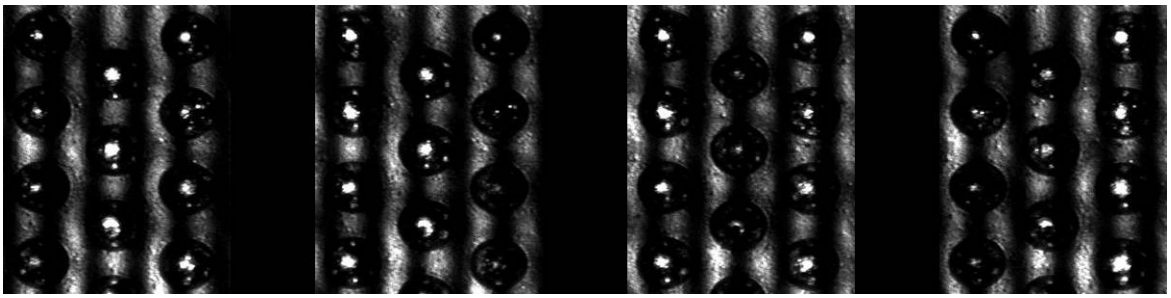

Figure 5-31. The first four phase shifted images of the bump field. Notice the intensity change at the top of the bumps with phase shifting.

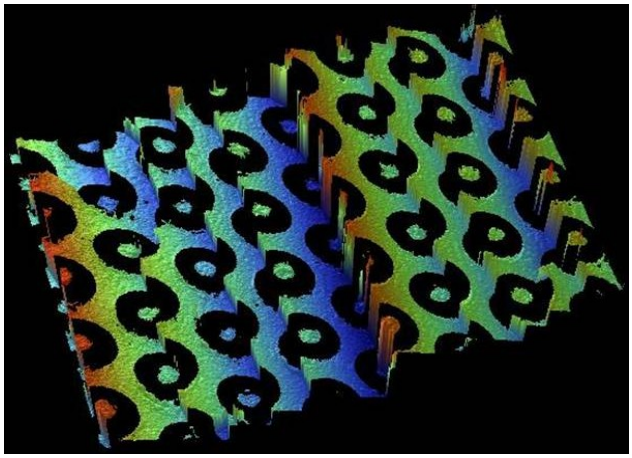

Figure 5-32. The bump field OPD map obtained by analyzing the interferograms shown in Figure 5-31. The software failed to unwrap the OPD map.

To overcome this problem, the software was tricked by replacing the pixels containing no data in the bump field interferograms by data points from the interferograms of a flat surface, as shown in Figure 5-33. Analyzing these interferograms generates an OPD with no unwrapping errors, with flat surfaces covering the areas that had no data in the original interferograms. This OPD is shown in Figure 5-34. A mask was then applied to delete the

artificially added flat surfaces to give the correct bump field OPD map shown in Figure 5-35.

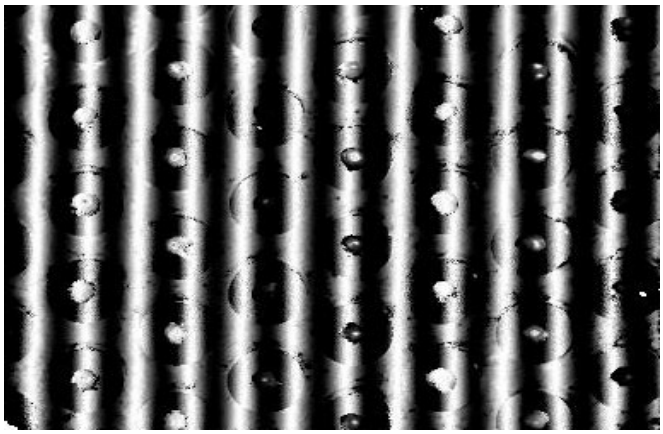

Figure 5-33. The bump field interferogram after replacing the missing data areas with data from a flat surface interferogram.

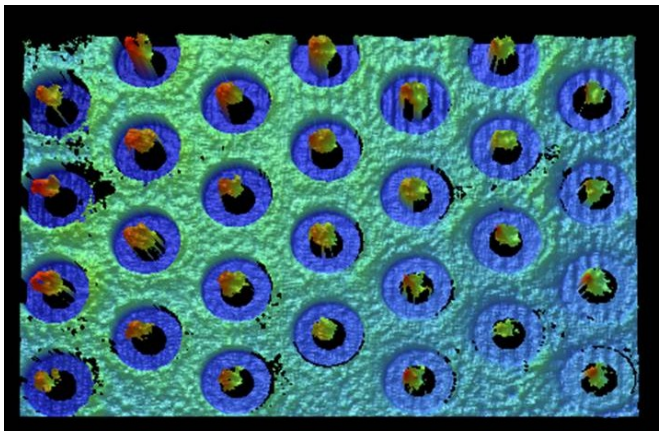

Figure 5-34. The OPD map of the bump field obtained by analyzing the interferograms shown in Figure 5-33. The areas that contain no data in the original bump field interferograms are now filled with a flat surface.

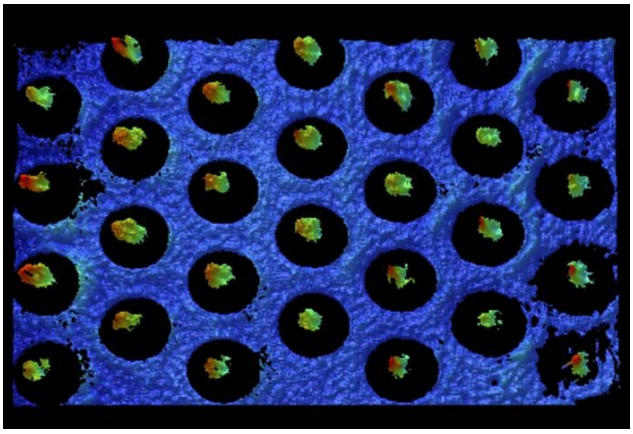

Figure 5-35. The same OPD in Figure 5-34 after masking out the artificially-added flat surfaces.

1.16.3 Estimating the bump parameters

The procedure described in Section 5.4.2 was followed to measure a solder bump field and estimate the parameters for selected bumps. To improve the measurement accuracy and minimize the fringe bleed through, the bump field was measured 50 times with a $(2\pi/50)$ phase shift added to the projected grating each time. Figure 5-36 shows the OPD map for a chosen bump in the field. The figure shows that the measured cap at the top of the bump suffers a rapid jump at the side. This was a common observation for the majority of the measured bumps. Looking at the original interferograms, it is clear that the intensity is the largest at these points.

To investigate this problem, the bump field was measured by projecting the same grating with 20 phase shifting steps from 0 to 2π to collect enough data points to have meaningful intensity plots for each pixel in the field. Figure 5-37-(b) shows a plot of the intensity variation of a non-saturated pixel as it goes through one complete intensity cycle, and Figure 5-37-(a) shows the intensity cycle of a bright pixel. Comparing the two plots, the non-saturated pixel is going through the intensity cycle with the expected sinusoidal dependence. On the other hand, the bright pixel shows clear saturation over much of the

phase shifting sequence. The bright pixels are mostly located at the top of the bumps where the projected light illuminates the bump and directly reflects into the imaging optics. These points saturate the camera at various steps in the phase shifting process, leading to a significant bias in the measurement at these spots. Further lowering the intensity leads to too much data drop out at the substrate level. In spite of the additions to the optical set up (filters, polarizers) that minimize this difference in fringe contrast, saturation of some pixels from the bumps appears to be unavoidable. These pixels were removed from the interferograms by monitoring the intensity variation through the phase shifting cycle and removing pixels with a gray level that exceeds the saturation level of the camera in at least 3 phase shifting steps. Figure 5-38 shows the same bump OPD map shown in Figure 5-36 after deleting bad data points.

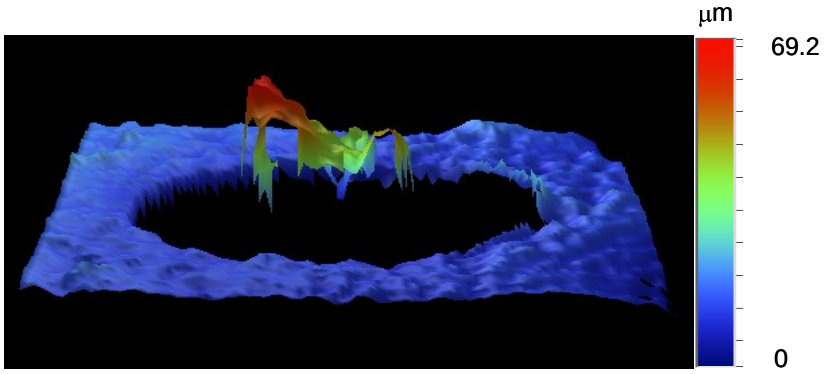

Figure 5-36. OPD map of a selected bump from the field shown in Figure 5-35. Notice the rapid height jump on the left side of the bump.

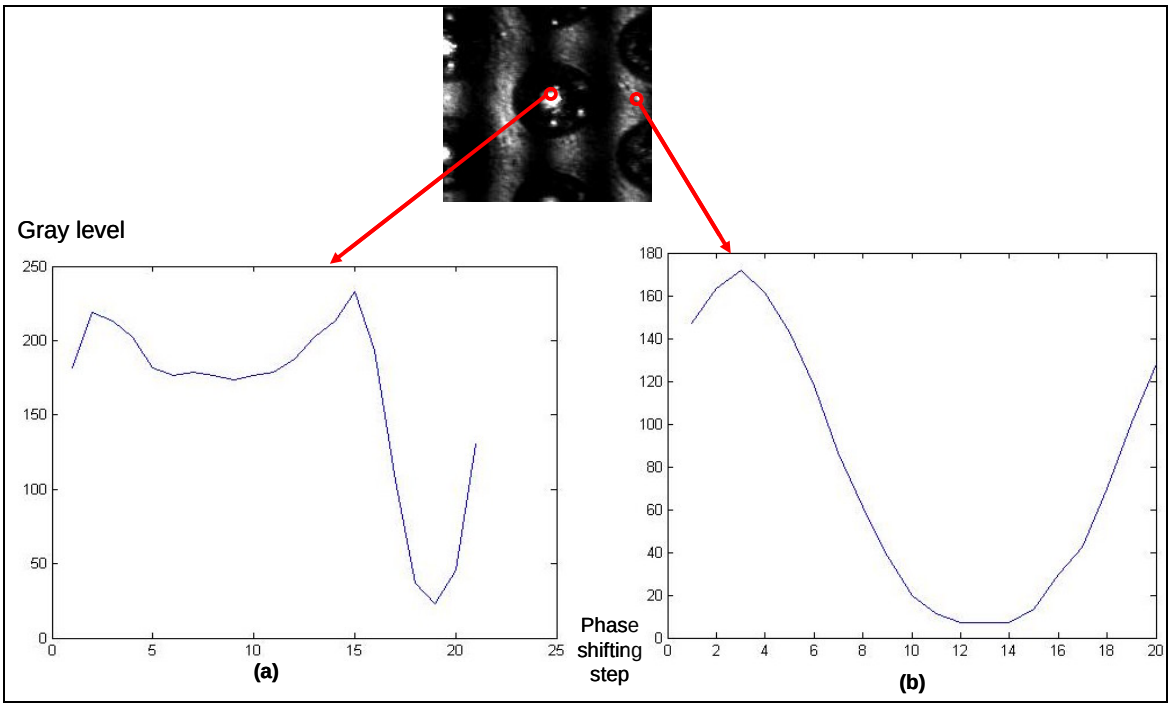

Figure 5-37. (a) The intensity cycle of a bright pixel. Notice that the camera is saturated for most of the phase shifting steps. (b) The intensity cycle of a non-saturated pixel. The profile is almost sinusoidal with no saturation.

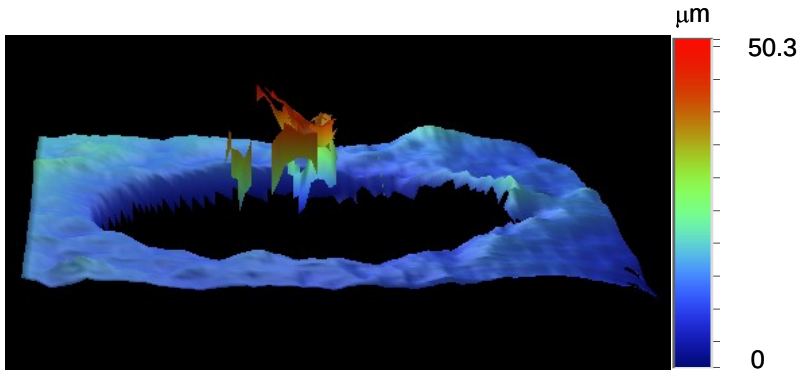

Figure 5-38. The bump OPD map showed in Figure 5-36 after deleting the bad data points from the interferograms.

Looking at Figure 5-38 we see that after removing the bad data points, the remaining data is not reminiscent of a cap, the fringe bleed through due to the camera nonlinearity is believed to be reason, it makes some pixels appear higher or lower than their real values. To estimate the bump height, one option was to fit a sphere through the data following the

same procedure used for the SWLI measurements. This approach failed since the number of pixels representing the bump data was insufficient for the algorithm to work. The other option was to take the difference between the maximum height value of the bump data and the substrate to be the bump height. This approach will give a height value that is so susceptible to errors since it's based on a value of one pixel (the pixel with the maximum height), which might be significantly affected by the fringe bleed through. Finally, we decided to estimate the bump height by finding the difference between the average value of the bump data and the average value of the substrate data, this gives the most reliable estimation since it averages out the effect of the fringe bleed through.

The bump height is estimated (in waves) using the multiple region analysis function in Vision™. In the multiple region analysis prompt, the region finding routine 'by separation' was chosen. This routine separates the data into two regions, the bump data and the substrate data, and gives the average of each. The difference between the mean values is taken to be the bump height. Figure 5-1 shows the multiple region analysis result for the bump shown in Figure 5-38.

For the diameter measurements, the 2-D analysis in Vision was used to measure the x-diameter of the bump in pixels. The diameter measured this way represents the diameter of the opening in the solder resist that contains the bump. From the SEM image shown in Figure 5-2 and the SWLI measurements, we see that the actual bump diameter is a little less than this value. Based on the SWLI and SEM measurements (discussed in Section 5.3.3), the bump diameter is estimated to be 90% of the measured solder resist opening diameter. Figure 5-40 shows the analysis for the diameter estimate for the same bump in Figure 5-38.

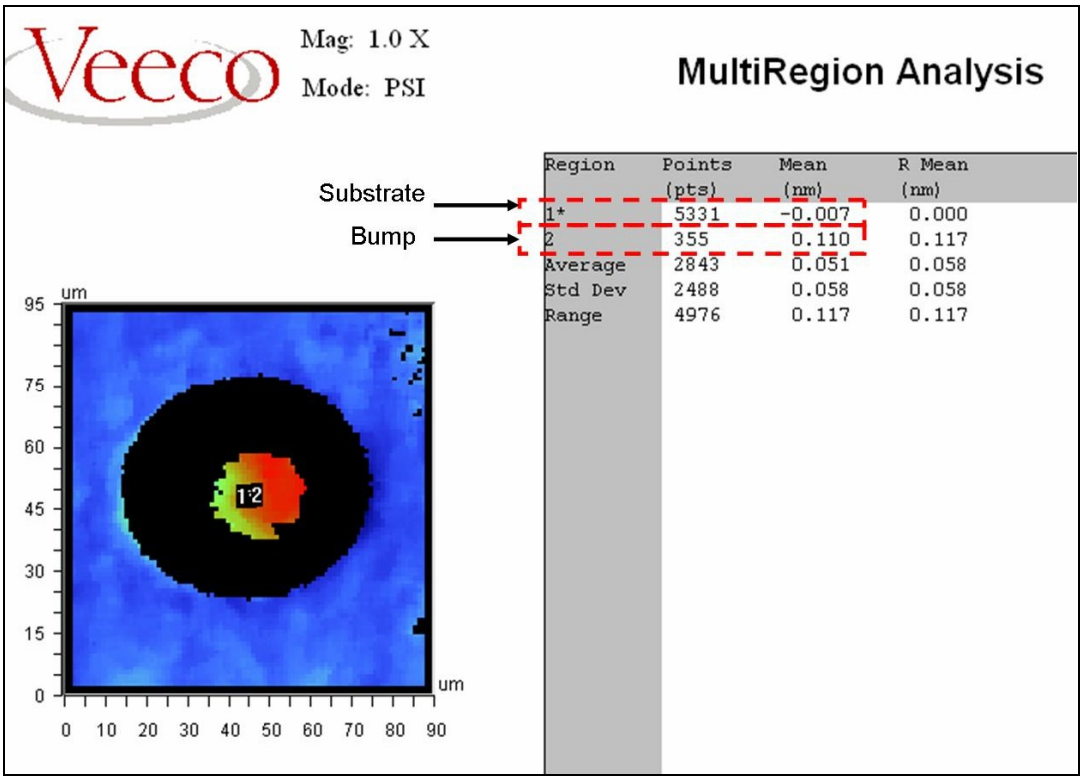

Figure 5-39. The multiple region analysis results for the bump height measurements. Region 1 represents the substrate data, and region 2 represents the bump data. The units here are normalized, so 1 nm = 1 wave.

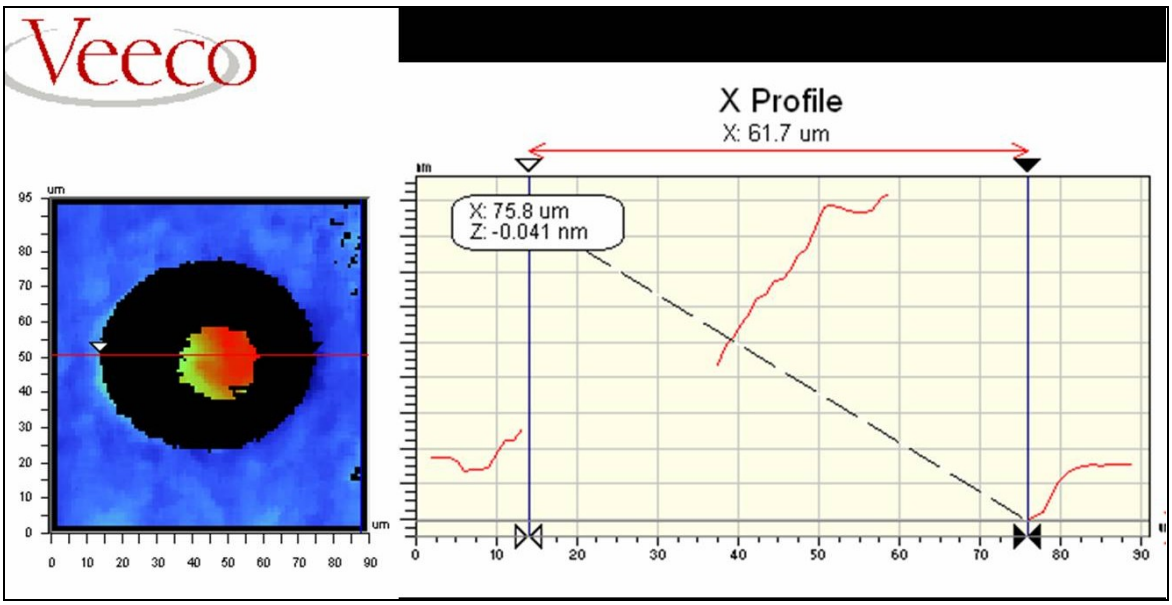

Figure 5-40. The 2D analysis for diameter measurements. The measured diameter is the diameter of the solder resist opening. A good estimate of the bump diameter is approximately 90% of this value. The units here are normalized, so every 1 µm is 1 pixel.

As mentioned at the beginning of this section, the bump field was measured 50 times, shifting the starting phase of the grating by (2π/50) every time. Five bumps were randomly selected to estimate their parameters. The parameters and the uncertainties were measured following the GUM [112]. Let the bump height (in waves) equal $h_{waves} \pm U_{h\_rep}$, and the diameter (in pixels) equal $d_{pixels} \pm U_{d\_rep}$, where h_{waves} is the bump mean height in waves, d_{pixels} is the mean bump diameter in pixels, and U_{h_rep}, and U_{d_rep} are the standard deviations of the repeated measurements of the height and the diameter, respectively. The height is multiplied by the height calibration factor discussed in Section 5.4.1 to find the height in micrometers, $h_{\mu m}$. The combined uncertainty of the height is then found using the following equation:

$$U_{hc} = h_{\mu m}\sqrt{\left(\frac{U_{h\_rep}}{h_{waves}}\right)^2 + \left(\frac{U_{h\_cal}}{h_{cal}}\right)^2}\ , \tag{5-10}$$

were h_{cal} is the height calibration factor in (μm/wave), and U_{h_cal} is the uncertainty in the height calibration factor. The same method is followed to obtain the bump diameter in micrometers and its combined uncertainty, $d_{\mu m} \pm U_{dc}$, where Equation 5-10 becomes

$$U_{dc} = d_{\mu m}\sqrt{\left(\frac{U_{d\_rep}}{d_{pixels}}\right)^2 + \left(\frac{U_{x\_cal}}{x_{cal}}\right)^2}\ . \tag{5-11}$$

Finally, the volume of the bump is calculated using Equation 5-8

$$V = \frac{1}{6}\pi h\left(\frac{3}{4}d^2 + h^2\right) = \frac{\pi}{8}hd^2 + \frac{\pi}{6}h^3\ (\mu m^3).$$

The combined uncertainty of the volume is then calculated using error propagation,

$$U_{Vc} = V\sqrt{2^2.\left(\frac{\pi}{8}\right)^2.\left(\frac{U_{dc}}{d_{\mu m}}\right)^2 + \left(\frac{\pi}{8}\right)^2.\left(\frac{U_{hc}}{h_{\mu m}}\right)^2 + \left(\frac{\pi}{6}\right)^2.3^2.\left(\frac{U_{hc}}{h_{\mu m}}\right)^2}\ . \tag{5-12}$$

As an example, the height and diameter distributions for the 50 measurements of the bump in Figure 5-38 is shown in Figure 5-41 and Figure 5-42, respectively.

The height for this bump, $h_{waves} \pm U_{h\_rep}$, is 0.150 ± 0.002 waves. The bump diameter, $d_{pixels} \pm U_{d\_rep}$, is 58.6 ± 0.5 pixels. The height is multiplied by the equivalent wavelength, 250.8 ± 16.2 μm/wave, to find the height in μm, $h_{\mu m}$ = 0.15 × 250.8 = 37.8 μm. The combined uncertainty for the height is found using Equation 5-10,

$$U_{hc} = 37.8\sqrt{\left(\frac{0.002}{0.151}\right)^2 + \left(\frac{16.2}{250.8}\right)^2} = 2.5\,(\mu\text{m}).$$

The diameter in pixels is multiplied by the x-calibration factor discussed in Section 5.4.1, 1.920 ± 0.007 μm/pixel, to find the diameter in micrometers, and its combined uncertainty is found using Equation 5-11. The final diameter estimate is d = 112.5 ± 1.1 μm.

The bump volume is calculated using Equation 5-8,

$$V = \frac{1}{6}\pi \times 37.8 \times \left(\frac{3}{4}112.5^2 + 37.8^2\right) = 2.17 \times 10^{+5}\ (\mu\text{m}^3).$$

The combined uncertainty of the volume is finally calculated using Equation 5-12,

$$U_{Vc} = 2.17 \times 10^{+5} \times \sqrt{2^2.\left(\frac{\pi}{8}\right)^2.\left(\frac{1.1}{112.5}\right)^2 + \left(\frac{\pi}{8}\right)^2.\left(\frac{2.5}{37.8}\right)^2 + \left(\frac{\pi}{6}\right)^2.3^2.\left(\frac{2.5}{37.8}\right)^2}$$

$$= 2.33 \times 10^{+4}\ (\mu\text{m}^3).$$

Table 5-5 shows the measured parameters for the 5 selected bumps.

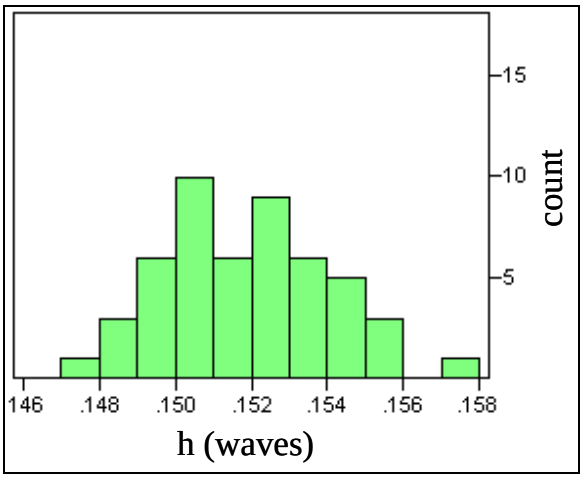

Figure 5-41. Bump height distribution in waves.

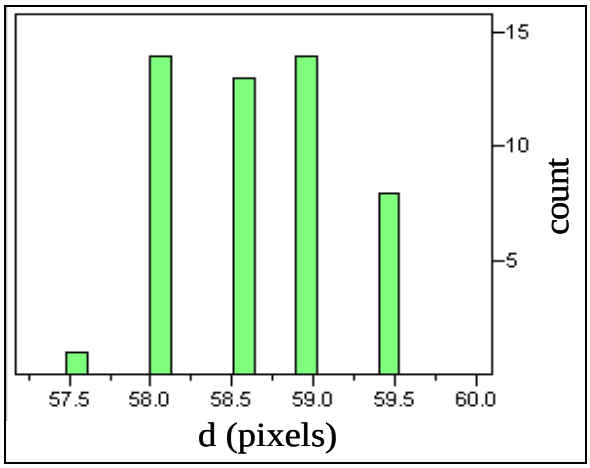

Figure 5-42. Bump diameter distribution in pixels.

	Height (um)	*Height Unc. (um)*	*Diameter (um)*	*Diameter Unc. (um)*	*Volume (um^3)*	*Volume Unc. (um^3)*	*Height % Unc.*	*Diameter % Unc.*	*Volume % Unc.*
B1	37.8	2.5	112.5	1.1	2.16E+5	2.35 E+4	6.6	1.0	10.8
B2	27.2	1.8	111.5	1.1	1.43 E+5	1.53 E+4	6.6	1.0	10.7
B3	28.1	2.1	108.3	1.7	1.41 E+5	1.71 E+4	7.5	1.6	12.2
B4	32.2	2.2	111.0	1.2	1.7 E+5	1.92 E+4	6.8	1.1	11.1
B5	36.3	2.8	112.1	1.3	2.04 E+5	2.55 E+5	7.7	1.2	12.5

Table 5-5. Bump parameters for 5 selected bumps on the field measured by the fringe projection system.

The data in Table 5-5 shows an average uncertainty of 2.2 μm for the height measurements. This number is less than 1% of the system's equivalent wavelength (~ 250 μm), which is a typical repeatability number for phase shifting interferometry [11, 15, 115]. In solder bump height measurement, this number is about 7% of the average bump height. Reducing the equivalent wavelength (by increasing the grating frequency) reduces the uncertainty. A smaller equivalent wavelength could not be used for solder bump measurements because multiple fringes near the top of the bump are not resolvable due to the large intensity and camera nonlinearity, causing data drop out.

In our system, the uncertainty values represent reproducibility numbers that take into consideration systematic biases as well as measurement and data analysis variability. Intel's uncertainty numbers shown in Section 5.3.4 are static repeatability numbers where the part was measured 30 times without moving it. They are not representative of an overall combined uncertainty or even the reproducibility of the system. Also, the data analysis carried out on Intel’s tool involves many approximations and considerable data messaging to obtain the bump height values (see Figure 5-7),. The analysis algorithms of this system are classified, therefore the impact on the measurement output could not be assessed.

The size and nature of solder bumps, and the data analysis involved, make the uncertainty in the measurement large compared to other test objects. For instance, measurements of continuous surfaces with height values in the range of the equivalent wavelength will have less than 1% of uncertainty.

For solder bump measurements, the measurement uncertainty in our system is limited by the camera linearity which causes fringe bleed through and measurement distortion at

the top of the bumps. For samples with a uniform reflectivity, the uncertainty is limited by intensity fluctuations. Both of these uncertainty sources can be reduced to enhance the system, and this is discussed in Chapter 6 as suggested future work.

CHAPTER 6: CONCLUSIONS AND FUTURE WORK

1.17 Conclusions

We propose a solution for one of the main limitations in classical interferometry and fringe projection, which is the dynamic range limitation. The technique is based on real time inverse fringe projection to enhance the dynamic range and increase the vertical resolution. The mathematical models derived in Chapter 4 describe the generation of the inverse fringes and their use to remove systematic biases (such as the perspective bias) and increase the dynamic range of fringe projection systems. The models also show that these fringes can be generated in real time without the need for prior information about the object or the system parameters. The object's surface geometry (optical path difference) map is first measured and then used to generate the inverse fringes to optically filter the low spatial frequency form. The higher spatial frequencies are then measured without the impact of the form. The technique can be applied in several steps to characterize specific feature size ranges and spatial frequencies.

A stereo microscope-based fringe projection system was designed, constructed, and used to illustrate the technique. The results presented in Chapter 4 demonstrate the generation of the inverse fringe pattern in real time and its use to correct for system biases. Another set of fringes is then generated to filter out the low spatial frequency form

of the test surface to enhance the systems vertical resolution for surface finish measurements.

The system was also used to characterize solder bumps, which are solder micro structures grouped in thousands on a package substrate to provide the electrical input/output connections in semiconductor flip chip technology. The results presented in Section 5.4 show that the system is capable of measuring solder bump height, diameter and volume with an uncertainty of approximately 10 %. Two major challenges are faced when measuring solder bumps. The spherical shape of the bumps, with large slopes on the sides, makes light collection from these regions difficult. Because the bumps are relatively smooth, only specular light is reflected from the sides and collecting light and therefore data from these regions requires a very large numerical aperture imaging system. Consequently, only a small patch at the top of the bump is captured by the imaging optics. Increasing the NA will increase the fraction of the bump surface that can be measured, but will decrease the field of view and hence the measurement speed.

The high reflectivity of the bump material is the other challenge. Large intensities from the portion of the bump imaged can easily saturate the camera and blur the fringe profile. Decreasing the intensity minimizes this, but decreased intensity decreases the amount of light reflected from the substrate since its reflectivity is much lower. Both surfaces must be measured to estimate the bump height. To minimize this problem, polarizers and green light filter were used. The green filter maximizes the light reflected of the substrate and reduces the light reflected of the bumps by approximately two thirds compared to white light illumination, and therefore maximizes the fringe contrast.

Individual solder bumps were also characterized using Zygo's NewView^{TM} scanning white light interferometer. The same bumps were previously measured using Intel's metrology tool. The results were compared to assess the uncertainty and bias of Intel's tool. Comparing the results presented in Chapter 5, we see that the SWLI has the lowest uncertainty and maximum repeatability even though only a small patch at the top of the solder bump can be measured. The SWLI is a more accurate tool with vertical resolution in the nanometer range, which makes it a very useful lab tool for high precision measurements. On the other hand, the SWLI is slow compared to Intel's tools, which makes it unsuitable for process control where parts are produced and inspected in high volumes.

Intel's system has repeatability in bump height measurements of approximately 1%. This number is strictly repeatability and does not represent the overall uncertainty or even reproducibility of the system. Intel's system repeatability combined with its measurement speed, which is approximately 10 minutes per 25 parts (total of approximately 100,000 bumps), the system can be a useful process control tool.

In our system, the uncertainty was around 2.2 μm. This number represents reproducibility and takes many sources of uncertainty into account such as data masking variability and image processing. Our uncertainty is less than 1% of the system's equivalent wavelength (~ 250 μm), which is a typical repeatability number for phase shifting interferometry [11, 15, 115]. Thus, reproducibility at the 1% level is quite good. In solder bump height measurement, this number is about 7% of the average bump height. Reducing the equivalent wavelength (by increasing the grating frequency) reduces the uncertainty, but this is not possible on a solder bump sample with the current system.

Although Intel's system is repeatable, it is not necessarily accurate. This is apparent from the bias between Intel's measurements and our SWLI measurements. Nevertheless, repeatability is more important than accuracy in process control. As long as the part is working, verification that produced parts fall within some tolerance range is usually sufficient. All instruments should be calibrated relative to each other, and scaling factors can always be used to make measurements consistent.

1.18 Future work

The size and nature of solder bumps make the application of characterizing such features difficult. The uncertainty in our system is about 1% of the system's equivalent wavelength which is typical for phase shifting interferometry. This number can be reduced by enhancing our system and minimizing the contribution of some of the uncertainty sources.

Since the uncertainty was ~ 1% of the equivalent wavelength, reducing the grating period will reduce the uncertainty (in micro meters). The smallest possible equivalent wavelength in our system is about 50 μm, which is limited by the lateral resolution of the system. Using this equivalent wavelength will reduce the uncertainty to the level of 0.5 μm. A smaller equivalent wavelength cannot be used, however, because multiple fringes near the top of the bump are not resolvable due to the large intensity and camera nonlinearity.

Camera nonlinear intensity response is the main error source when measuring solder bumps. This causes the fringes viewed by the camera to deviate from the sinusoidal profile, causing a periodic ripple in the final surface map. This is called fringe bleed through. The effect of nonlinearity peaks when the intensity of the light viewed by the

camera is close to the saturation level of the camera pixels. Although saturation artifacts are minimized by reducing the intensity reflected from the top of the bumps, and filtering saturated pixels from the measurement, the nonlinearity artifacts are still present, causing the measured part of the bump to deviate from the spherical cap shape as shown in Figure 5-38.

In some cases, the peak to valley amplitude of the bleed through ripple was approximately 5 μm. Using a camera with a better linear intensity response will minimize this problem. The camera's intensity nonlinearity can be verified by capturing images where the intensity is varying and plotting the average pixel value versus the projected image intensity. To minimize the fringe bleed through, the light intensity should be fixed to work within the linear region of this plot. Cooling the camera detector can also enhance the linearity [15]. It is likely that the peak to valley ripple caused by the fringe bleed through can be reduced to less than 1 μm.

The instability of the projector light source is another major source of error. The intensity in commercial digital projectors is stable enough for the human eye, but it is not optimized for metrology applications. The intensity variation in the projector's light during phase shifting will be translated to a height bias in the final surface height map. The light stability can be tested by projecting a constant frame and monitoring the average pixel intensity over time. This test was conducted during my internship at Intel, and the results showed that the average intensity fluctuates randomly by as much as 10 gray levels (around 5 μm using a wavelength of 250 μm). This error can be significantly reduced by introducing a feedback loop to monitor the intensity and correct for these

fluctuations. Also, averaging multiple images for each phase shifting step during a measurement minimizes this error.

Other error sources, such as electronic noise in the camera and frame grabber, and mechanical vibrations contribute to the measurement uncertainty but at a lower level. The mechanical vibration effect can be tested by projecting a fixed grating and monitoring the phase change in the fringes over time.

By improving the system to minimize the above error sources, and placing the system in an environment free of vibrations, a measurement uncertainty at a level of 0.2% of the equivalent wavelength is achievable. This is approximately 0.5 μm using an equivalent wavelength of 250 μm. This is a reasonable uncertainty for Intel's requirements, therefore the system can be optimized to characterize solder bumps with acceptable uncertainty levels.

References

1. Webster's International Dictionary, Merriam Webster, 1998

2. Daniel Malacara, "Optical Shop Testing", 2'nd Edition. Wiley-Interscience, New York, 1992, Chapter 16

3. David W. Robinson and Graeme T. Reid, "Interferogram Analysis: Digital Fringe Pattern Measurement Techniques", Institute of physics publishing, Bristol and Philadelphia, 1993, pp 49-57

4. Daniel Malacara, Manuel Servin and Zacarias Malacara, "Interferogram Analysis for Optical Testing ", Marcel Dekker, Inc, New York, 1998, pp 21-25

5. K. Patorski, "The Handbook of Moiré Fringe Technique", Elsevier, New York, 1993

6. J. D. Briers, "Holographic, Speckle and Moiré techniques in Optical Metrology", Prog. Quant. Electr., Vol. 17, pp. 167-233, 1993

7. Patorski K., "Moiré Methods in Interferometry", Optics and Lasers in Engineering, Vol. 8, pp 147-170, 1988

8. Reid G. T., "Moiré Fringes in Metrology", Optics and Lasers in Engineering, Vol. 5, pp 63-93, 1984

9. Reid G. T., R. C. Rixon and H. I. Messer, " Measurement of Three Dimentional Shape by Phase-Measuring Moiré Topography", Opt. and Laser Tech., Vol. 16, pp 315-319, 1984

10. Robert Czarnek, "High Sensitivity Moiré Interferometry with Compact Achromatic Interferometer", Optics and Lasers in Engineering, Vol. 13, pp 99-115, 1990

11. G. Oster and Y. Nishijima, "Moiré Patterns", Sci. Amer, Vol 208, pp 54-63, 1963

12. H. Phillips Stahl, "White-Light Moiré Phase-Measuring Interferometry", SPIE proceedings, Vol. 1332, pp 720-730, 1990

13. Pramod K. Rastogi and Daniel Inaudi, "Trends in Optical Nondestructive Testing and Inspection", First Edition, Elsevier Science Ltd., 2000, Chapter 23.

14. Daniel Post, Bongtae Han, and Peter Ifju, " High Sensitivity Moiré: Experimental Analysis for Mechanics and Materials", Springer-Verlag New York, Inc. 1994.

15. C. A. Walker, "Handbook of Moiré Measurement", IOP Publishing Ltd. 2004

16. Parmod K. Rastogi, "Photomechanics", Springer-Verlag, Berlin, Germany, 2000, Chapter 5.

17. Kjell J. Gesvik, "Optical Metrology", Third Edition, John Wiley & Sons, Ltd. 2002, Chapter 7.

18. B. P. Hildebrand and K. Haines, "The Generation of 3-D Contour Maps by Wavefront Reconstruction", Physics Letters, Vol. 21, pp 422-423, 1966

19. P. Hariharan, "Optical Holography", Cambridge University Press, Cambridge, 1984

20. Max Born, and Emil Wolf, "Principles of Optics," Seventh edition, Cambridge university press, 2002.

21. Eugene Hecht, "Optics," Fourth edition.

22. B. Han and Y. Guo, "determination of an effective coefficient of thermal expansion of electronic packaging components: a hole field approach", IEEE Transa. Components, Packaging and manufacturing Technology, Vol 19, 1996

23. Y. Guo, C. Lim, W. Chen and C. Woychik, "Soldr Ball Connect Assemblies Under Thermal Loading: Deformation measurement via Moiré Interferometry" IBM J. Res. Development, Vol 37, pp 635-647, 1993

24. B. Han and Y. Guo, "Thermal Deformation Analysis of Various Electronic Packaging Products by Moiré and Microscopic Moiré Interferometry", ASME Jornal of Electronic Packaging, Vol 117, pp 185-191, 1995.

25. C. Sciamarella, "Use of Gratings in Strain Analysis", Phys. Sci. Instr., Vol 5, pp 833-845, 1972.

26. C. Sciamarella, G. DiChirico, and T. Chang, "Moiré Holographic Technique for Three-Dimensional Analysis", Applied Mechanics, Vol 37, pp 180-185, 1970.

27. K. Kato, T. Morota, and T. Jimma, "Improvement of Moiré and Grid Methods of Plastic Strain Analysis and Their Application to Extrusion", Bull Japan Society of Mechanical Engineering, Vol 12, pp 32-42, 1969.

28. R. Millera, I. Mohammed, and P. Ho, "Quantitative strain analysis of flip-chip electronic packages using phase-shifting moiré interferometry", Optics and Lasers in Engineering , Vol 36, pp 127-139, 2001.

29. J. D. Wood, M. Tsai, D. Post, J. Morton, V. J. Parks, and F. P. Gerstle, "Thermal Straind in Bimaterial Joint: an Experimental and Numerical Analysis", Proc. SEM

Spring Conference on Experimental Mechanics, pp 543-551, Society for experimental mechanics, Bethel, Connecticut, 1989.

References

30. Webster's International Dictionary, Merriam Webster, 1998

31. Daniel Malacara, "Optical Shop Testing", 2'nd Edition. Wiley-Interscience, New York, 1992, Chapter 16

32. David W. Robinson and Graeme T. Reid, "Interferogram Analysis: Digital Fringe Pattern Measurement Techniques", Institute of physics publishing, Bristol and Philadelphia, 1993, pp 49-57

33. Daniel Malacara, Manuel Servin and Zacarias Malacara, "Interferogram Analysis for Optical Testing ", Marcel Dekker, Inc, New York, 1998, pp 21-25

34. K. Patorski, "The Handbook of Moiré Fringe Technique", Elsevier, New York, 1993

35. J. D. Briers, "Holographic, Speckle and Moiré techniques in Optical Metrology", Prog. Quant. Electr., Vol. 17, pp. 167-233, 1993

36. Patorski K., "Moiré Methods in Interferometry", Optics and Lasers in Engineering, Vol. 8, pp 147-170, 1988

37. Reid G. T., "Moiré Fringes in Metrology", Optics and Lasers in Engineering, Vol. 5, pp 63-93, 1984

38. Reid G. T., R. C. Rixon and H. I. Messer, " Measurement of Three Dimentional Shape by Phase-Measuring Moiré Topography", Opt. and Laser Tech., Vol. 16, pp 315-319, 1984

39. Robert Czarnek, "High Sensitivity Moiré Interferometry with Compact Achromatic Interferometer", Optics and Lasers in Engineering, Vol. 13, pp 99-115, 1990

40. G. Oster and Y. Nishijima, "Moiré Patterns", Sci. Amer, Vol 208, pp 54-63, 1963

41. H. Phillips Stahl, "White-Light Moiré Phase-Measuring Interferometry", SPIE proceedings, Vol. 1332, pp 720-730, 1990

42. Pramod K. Rastogi and Daniel Inaudi, "Trends in Optical Nondestructive Testing and Inspection", First Edition, Elsevier Science Ltd., 2000, Chapter 23.

43. Daniel Post, Bongtae Han, and Peter Ifju, " High Sensitivity Moiré: Experimental Analysis for Mechanics and Materials", Springer-Verlag New York, Inc. 1994.

44. C. A. Walker, “Handbook of Moiré Measurement”, IOP Publishing Ltd. 2004

45. Parmod K. Rastogi, “Photomechanics”, Springer-Verlag, Berlin, Germany, 2000, Chapter 5.

46. Kjell J. Gesvik, “Optical Metrology”, Third Edition, John Wiley & Sons, Ltd. 2002, Chapter 7.

47. B. P. Hildebrand and K. Haines, “The Generation of 3-D Contour Maps by Wavefront Reconstruction”, Physics Letters, Vol. 21, pp 422-423, 1966

48. P. Hariharan, “Optical Holography”, Cambridge University Press, Cambridge, 1984

49. Max Born, and Emil Wolf, “Principles of Optics,” Seventh edition, Cambridge university press, 2002.

50. Eugene Hecht, “Optics,” Fourth edition.

51. B. Han and Y. Guo, “determination of an effective coefficient of thermal expansion of electronic packaging components: a hole field approach”, IEEE Transa. Components, Packaging and manufacturing Technology, Vol 19, 1996

52. Y. Guo, C. Lim, W. Chen and C. Woychik, “Soldr Ball Connect Assemblies Under Thermal Loading: Deformation measurement via Moiré Interferometry” IBM J. Res. Development, Vol 37, pp 635-647, 1993

53. B. Han and Y. Guo, “Thermal Deformation Analysis of Various Electronic Packaging Products by Moiré and Microscopic Moiré Interferometry”, ASME Jornal of Electronic Packaging, Vol 117, pp 185-191, 1995.

54. C. Sciamarella, “Use of Gratings in Strain Analysis”, Phys. Sci. Instr., Vol 5, pp 833-845, 1972.

55. C. Sciamarella, G. DiChirico, and T. Chang, “Moiré Holographic Technique for Three-Dimensional Analysis”, Applied Mechanics, Vol 37, pp 180-185, 1970.

56. K. Kato, T. Morota, and T. Jimma, “Improvement of Moiré and Grid Methods of Plastic Strain Analysis and Their Application to Extrusion”, Bull Japan Society of Mechanical Engineering, Vol 12, pp 32-42, 1969.

57. R. Millera, I. Mohammed, and P. Ho, “Quantitative strain analysis of flip-chip electronic packages using phase-shifting moiré interferometry”, Optics and Lasers in Engineering , Vol 36, pp 127-139, 2001.

58. J. D. Wood, M. Tsai, D. Post, J. Morton, V. J. Parks, and F. P. Gerstle, "Thermal Straind in Bimaterial Joint: an Experimental and Numerical Analysis", Proc. SEM Spring Conference on Experimental Mechanics, pp 543-551, Society for experimental mechanics, Bethel, Connecticut, 1989.

59. Y. Guo, D. Post and R. Czarnek, "The Magic of Crrier Patterns in Moiré Interferometry", Experimental Mechanics, Vol 29, pp 169-173, 1989

60. F. K. Ligtenberg, "The Moiré Method, a New Experimental Method for Determination of Moments in Small Slab Model", Proc. Soc. Exp. Stress Analysis. Vol. 12, pp 83-98, 1954

61. G. Reider and R. Ritter, "Krummungsmessung an belasteten Platten nach den Ligtenbergschen Moiré Verfahren", Forsch. Ing. –Wes. Vol 31, pp 33-44, 1965.

62. C. A. Sciammarella and O. Combel, "Interferometric Reflection Moiré", SPIE proceedings, Interferometry VII Applications, pp 72-85, 1995.

63. J. P. Duncan, "The Optical Survey of Curved Surfaces", University of British Colombia, Vancouver, 1966.

64. C. Osgerby, "Application of the Moiré Method for use With Culindrical Surfaces", Experimental Mechanics, Vol. 7, pp 313-320, 1967.

65. M. Pedretti, "Nouvelle Méthode de Moiré Pur l'analyse des Plaques Fléchies", Ph.D. Thesis, Ecole Polytechnique Fédérale de Lausanne, 1974.

66. J. Kapkowski, "A New Variety of Reflection-moiré Method", Lectures of 9'th Congress on Material Testing, Budapest, 1986.

67. D. M. Meadows, W. O. Johnson, and J. B. Allen, "Generation of Surface Contours by Moire Patterns", Applied Optics, Vol. 9, pp 942-947, 1970.

68. H. Takasaki, "Moire Topography", Applied Optics, Vol. 12, pp. 845-850, 1973.

69. F. P. Chiang, "Moire Methods for Contouring, Displacement, Deflection, Slope and Curvature", SPIE Proceedings, Vol. 153, pp 113-119, 1978.

70. B. C. Dykes, "Analysis of Displacements in Large plates by the Grid-Shadow Moire Techniques", Proceedings of the fourth int. conference in Sress Analysis, Cambridge, Experimental Stress Analysis and its Influence on Design, pp. 125-134, 1971.

71. L. Pirodda, "Shadow and Projection Moire Techniques for Absolute or Relative Mapping of Surface Shapes", Optical Engineering, Vol. 21, pp 640-649, 1982.

72. H. Takasaki, "Moire Topography from its Birth to Practical Application", Optics and Lasers in Engineering, Vol. 3, pp 3-14, 1982.

73. J. J. Dirckx, W. F. Decraemer, and J. L. Janssens, "Real-time Shadow Moiré Vibration Measurement: Method Featuring Simple Setup, High Sensitivity, and Exact Calibration", Applied Optics, Vol. 25, pp 3785-3787, 1986.

74. T. Ikeda, and H. Terada, "Development of Moire Method With Special Reference to its Application to Biostereometrics", Optics and Lasers Technology, Vol. 13, pp 302-306. 1981

75. P. G. Ifju, X. Niu, and M. Papila, "Shadow Moire Interferometry Applied to Composite Column Buckling", Handbook of Moire Measurement, IOP Publishing Ltd. 2004, Chapter 11.1

76. B. Han, "Shadow Moire Interferometry eith Enhanced Sinsitivity by Optical / Digital Fringe Moultiplication", Handbook of Moire Measurement, IOP Publishing Ltd. 2004, Chapter 11.1

77. Y. Wang, "Shadow Moire Interferometry with a Phase Stepping Technique applied to Thermal Warpage Measurement of Modern Electronic Packages", Handbook of Moire Measurement, IOP Publishing Ltd. 2004, Chapter 11.1

78. G. S. Spagnolo, G. Guattari, C. Sapia, D. Ambrosini, D. Paoletti and G. Accardo, "Contouring of Artwork Surface by Fringe Projection and FFT Analysis", Optics and Lasers in Engineering, Vol. 33, pp 141-156, 2000

79. P. Benoit, E. Matheieu, J. Hormiere and A. Thomas, "Characterization and Control of Three Dimentional Objects Using Fringe Projection Techniques", Nouv. Rev. Optiue, Vol. 6, pp 67-86, 1975

80. A. Fagg, B. Hales and H. Stahl, "Systematic Errors of a Projection Moire Contouring System", SPIE Proceedings, Vol. 1776, pp 120- 128, 1992

81. G. Spagnolo, G. Guattari, C. Sapia, D. Ambrosini, D. Paoletti, and G. Accardo, "Contouring of Art Work Surface By Fringe Projection and FFT Analysis", Optics and Lasers in Engineering, Vol. 33, pp 141-156, 2000

82. M. Idesawa, T. Yatagai, and T. Soma, "Scanning Moire Method and Automatic Measurement of 3-D Shapes", Applied Optics, Vol. 16, pp 2152-2162, 1977

83. C. Quan, C. J. Tay, X. Y. He, X. Kang, H. M. Shang, "Microscopic Surface Contouring by Fringe Projection Method", Optics and Laser Technology, Vol. 34, pp 547-552, 2002

84. K. Korner, R. Windecker, M. Fleischer, and H. J. Tiziani, "One-Grating Projection for Absolute Three-Dimentional Profiling", Optical Engineering, Vol. 4, Issue 8, pp 1653-1659, 2001

85. R. Windecker, M. Flischer, K. Korner and H. J. Tiziani, "Testing Micro Devices With Fringe Projection and White Light Interferometry", Optics and Lasers in Engineering, Vol. 36, pp 141-154, 2001

86. http://vsd.pennnet.com/Articles/Article_Display.cfm?Section=Articles&Subsection=Display&ARTICLE_ID=219446

87. http://www.computeroptics.com/telecentric.html

88. http://www.edmundoptics.com/TechSupport/DisplayArticle.cfm?articleid=239

89. B. Dessus, and M. LeBlanc, "The Fringe Method and its Application to the Measurement of Deformations, Vibrations, Contour Lines and Defferences of Objects", Optics Electronics, Vol. 5, pp 369-390, 1973

90. P. Benoit, and E. Mathieu, "Real Time Contour Line Visualization of an Object", Optics Communications, Vol. 12, pp 175-180, 1974

91. O. Leder, and H. Kurz, "The Miles-Speight Moire Method Applications and Perspectives in Medicine", Acta Stereol. Vol. 6, pp 763-768, 1987

92. James C. Wyant, "White light Interferometry," Proceedings of SPIE, Vol. 4737, pp.98-107, July 2002.

93. Guan-Chang Jin, and Nai Keng Bao, "Surface detection and 3D profilometry for mucrostructure using optical metrology," Optics and Lasers in Engineering, Vol. 36, pp. 1-9, 2001.

94. Werner Nadeborn, Peter Andra, and Wolfgang Osten, "A robust procedure for absolute phase measurement", Optics and Lasers in Engineering (24), pp. 245-260, 1995.

95. E.U. Wagemann, T Haist, M. Schonlerber, and H. J. Tiziani, "Fast shape and position control by moiré-filtering and object-adapted fringe projection", Optics Communications (165), pp. 7-10, 1999.

96. Wansong Li, Thorsten Bothe, Wolfgang Osten, and Michael Kalms, "Object adapted pattern projection-Part I: generation of inverse patterns", Optics and Lasers in Engineering (41), pp. 31-50, 2004.

97. Toyohiko Yatagai, and Masanori Idesawa, “Use of synthetic deformed gratings in moiré topography”, Optics Communications (20), pp. 243-245, 1977.

98. Knight, P. Douglas, “Liquid crystal phase modulation technique to reduce the spatial frequency of interferometric fringes,” MSC Thesis, Department of Physics, UNC-Charlotte, 1996.

99. K. Leonhardt, U. Droste, and H. J. Tiziani, Microshape and rough-surface analysis by fringe projection, Applied Optics. Vol. 33**,** pp. 7477 7488, 1994.

100. R. Windecker, M. Fleischer, and H. J. Tiziani, Three dimensional topometry with stereo microscopes, Optical Engineering, Vol. 36**,** pp. 3372 3377, _1997.

101. Chenggen Quan, Cho Jui Tay, Xin Kang, Xiao Yuan He, and Huai Min Shang, Shape measurement by use of liquid crystal display fringe projection with two step phase shifting, Applied Optics, Vol. 42, pp. 2329-2335, 2003.

102. http://www.tyrexsales.com/dlp/

103. R. Windecker, S. Franz, and H. J. Tiziani, Optical roughness measurements with fringe projection, Applied Optics, Vol 38**,** pp. 2837 2842, 1999.

104. R. Windecker, M. Fleischer, S. Franz, and H. J. Tiziani, Testing micro devices with fringe projection and white-light interferometry, Optics and Lasers in Engineering, Vol. 36, pp. 141 154, 2001.

105. K.-P. Proll, J.-M. Nivet, C. Voland, and H. J. Tiziani, “Application of a liquid-crystal spatial light modulator for brightness adaptation in microscopic topometry,” Applied Optics, Vol. 39, pp. 6430–6435, 2000.

106. http://lfw.pennnet.com/Articles/Article_Display.cfm?Section=ARCHI&ARTICLE_ID=197515&VERSION_NUM=1&p=12

107. http://www.projectorcentral.com/lcos.htm

108. Eugene Hecht, “Optics,” Fourth Edition, Addison Wesley, 2002

109. www.zygo.com

110. Aliaster B. Forbs, ”Robust circle and sphere fitting by least squares,” National Physics Laboratory, 1999.

111. http://mathworld.wolfram.com/SphericalCap.html

112. http://physics.nist.gov/cuu/Uncertainty/combination.html

113. http://homepages.inf.ed.ac.uk/cgi/rbf/CVONLINE/entries.pl?TAG248

114. http://www.icaen.uiowa.edu/~dip/LECTURE/3DVisionP1_2.html#knownscene

115. Katherine Creath, “Practical interferometry and fringe analysis,” Optics and Photonics conference, San Diego, 2005.